NASA CR - 168340

NASA

ADVANCED ION THRUSTER RESEARCH

(NASA-CR-168340) ADVANCED ION THRUSTER RESEARCH Annual Report, 1 Oct. 1982 - 1 Nov. 1983 (Colorado State Univ.) 139 p HC A07/MF A01 CSCL 21C G3/20

N84-19467

Unclas 11912

PREPARED FOR

LEWIS RESEARCH CENTER

NATIONAL AERONAUTICS AND SPACE ADMINISTRATION

Grant NGR-06-002-112

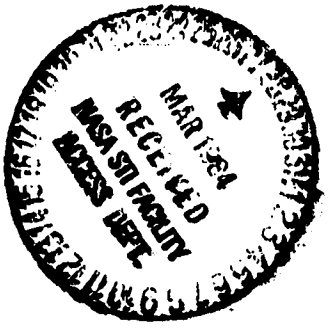

Annual Report

Jan. 1984

Paul J. Wilbur
Department of Mechanical Engineering
Colorado State University
Fort Collins, Colorado

1. Report No.	2. Government Accession No.	3. Recipient's Catalog No.
NASA CR 168340		

4. Title and Subtitle	5. Report Date
ADVANCED ION THRUSTER RESEARCH	Jan. 1984
	6. Performing Organization Code
7. Author(s)	8. Performing Organization Report No.
Paul J. Wilbur	
9. Performing Organization Name and Address	10. Work Unit No.
Department of Mechanical Engineering Colorado State University Fort Collins, Colorado 80523	11. Contract or Grant No.
12. Sponsoring Agency Name and Address	13. Type of Report and Period Covered
National Aeronautics and Space Administration Washington, D.C. 20546	Annual, Oct. 1, 1982 - Nov. 1, 1983
	14. Sponsoring Agency Code

15. Supplementary Notes

Grant Monitor - William Kerslake, NASA Lewis Research Center, Cleveland, Ohio 44135.

16. Abstract

A simple model describing the discharge chamber performance of high strength, cusped magnetic field ion thrusters is developed. The model is formulated in terms of the energy cost of producing ions in the discharge chamber and the fraction of ions produced in the discharge chamber that are extracted to form the ion beam. The accuracy of the model is verified experimentally in a series of tests wherein the discharge voltage, propellant, grid transparency to neutral atoms, beam diameter and discharge chamber wall temperature are varied. The model is exercised to demonstrate what variations in performance might be expected by varying discharge chamber parameters. The results of a study of xenon and argon orificed hollow cathodes are reported. These results suggest that a hollow cathode model developed from research conducted on mercury cathodes can also be applied to xenon and argon. Primary electron mean free paths observed in argon and xenon cathodes that are larger than those found in mercury cathodes are identified as a cause of performance differences between mercury and inert gas cathodes. Data required as inputs to the inert gas cathode model are presented so it can be used as an aid in cathode design.

17. Key Words (Suggested by Author(s))	18. Distribution Statement
Electrostatic Thruster Hollow Cathode	Unclassified - Unlimited

19. Security Classif. (of this report)	20. Security Classif. (of this page)	21. No. of Pages	22. Price*
Unclassified	Unclassified	135	

* For sale by the National Technical Information Service, Springfield, Virginia 22161

TABLE OF CONTENTS

LIST OF FIGURES

LIST OF TABLES

ION EXTRACTION CAPABILITIES OF TWO-GRID ACCELERATOR SYSTEMS

D. C. Rovang

An experimental investigation of the ion extraction capabilities of two-grid accelerator systems was conducted during this grant period. This work is described in Ref. 1 so it will not be reproduced here. The body of experimental data presented in Ref. 1 facilitates the selection of the accelerator system geometries and operating parameters necessary to maximize extracted ion current. Reductions in screen hole diameter to 0.5 mm are shown to induce no dramatic changes in impingement-limited perveance. Results obtained at small grid separation ratios suggest a new grid operating condition where high beam current per hole levels are achieved at a specified net accelerating voltage. This operating condition is realized at a relatively high, optimum ratio of net-to-total accelerating voltage ratio. Electron backstreaming and electrical breakdown characteristics of two-grid systems are also given.

ELECTROTHERMAL RAMJET RESEARCH

B. D. Shaw

Extensive theoretical analysis of the electrothermal ramjet[2] concept was completed during this grant period. This work describes the effects of ionization and dissociation of the propellant on the performance of the ramjet. The effects of ionization are shown to be small so they can be neglected. Dissociation phenomena are modelled using equilibrium, frozen flow and finite reaction rate approaches and the equilibrium approach is shown to

model the processes adequately. The performance degradation introduced by consideration of these real gas effects are shown to be sufficiently small so that the electrothermal ramjet concept still shows considerable promise. A separate report describing this work in detail is planned in the near future.

SIMPLE PERFORMANCE MODEL FOR RING AND LINE CUSP ION THRUSTERS

John R. Brophy

Introduction

In order to improve thruster performance it is desirable to have a theoretical model which describes the effects of thruster design variables and operating parameters on performance. Theoretical models have been developed in the past to predict the performance of both low magnetic field strength (Kaufman type) thrusters[3] and high field strength cusped thrusters.[4] However, these models typically consist of a complex set of equations which must be solved iteratively by a computer. This complexity makes it difficult to identify the dominate mechanisms controlling thruster performance. Earlier work (on Kaufman type thrusters) by Masek[5] and Knauer[6] described thruster performance physically in terms of the average energy expended to produce ions in the discharge chamber plasma. This work resulted in an increased understanding of some of the phenomena affecting thruster performance, but stopped short of providing the capability to predict the performance.

In this paper, a model is developed for high field strength cusped thrusters, which results directly in a single equation for the energy cost of a beam ion (eV/beam ion) as a function of the propellant utilization. This is made possible by formulating the model in terms of the average discharge plasma ion energy cost and the fraction of ions produced which are extracted into the beam. A key feature of the model is that it makes it possible for one to calculate readily the average energy required to produce an ion in the discharge chamber plasma as a function of the propellant mass flow rate and propellant utilization. Comparison of calculated

and measured values of the average plasma ion energy cost are made for variations in propellant flow rate, propellant type, discharge voltage, propellant utilization, accelerator grid open area fraction and beam diameter. The effect of the variation in each of these parameters on the ratio of beam current to ion current produced (extracted ion fraction) is also investigated.

Finally, the model is exercised to indicate the effects on thruster performance due to variations in such parameters as; propellant flow rate, propellant type, discharge voltage, extracted ion fraction, accelerator grid transparency to neutrals and the containment of primary electrons. The potential for improvements in thruster design suggested by the model are discussed.

Theoretical Development

Beam Ion Energy Cost

The specific discharge power, or energy cost per beam ion is defined as,

$$\varepsilon_B = (J_D - J_B)\, V_D/J_B, \text{ [eV/beam ion]} \qquad (1)$$

where the symbols are defined in Appendix A. The beam current (J_B) in Eq. 1 is subtracted from the discharge current (J_D) so that the energy that goes into accelerating the beam ions through the discharge voltage is not charged to the energy cost per beam ion.

In a similar manner the average energy expended in creating ions in the discharge chamber plasma may be defined as,

$$\varepsilon_p = [J_D - (J_C + J_B)]\, V_D/J_p \text{ , [eV/plasma ion].} \qquad (2)$$

By analogy to Eq. 1, the "$J_C + J_B$" term is subtracted from the discharge current so that the energy that goes into accelerating these ions out of the discharge chamber plasma into the chamber walls or the beam is not included in the ion production cost. Rearranging Eq. 2 yields,

$$\varepsilon_p = \frac{(J_D - J_B)}{J_B} V_D \left(\frac{J_B}{J_p}\right) - \frac{J_C}{J_p} V_D \quad . \tag{3}$$

Defining the fractions of ion current produced that go into the beam and to cathode potential surfaces as,

$$f_B = J_B/J_p \text{ and } f_C = J_C/J_p \quad , \tag{4}$$

respectively, and using Eq. 1 in Eq. 3 yields,

$$\varepsilon_p = \varepsilon_B f_B - f_C V_D \quad . \tag{5}$$

Solving this equation for ε_B gives the result,

$$\varepsilon_B = \varepsilon_p / f_B + f_C V_D / f_B \quad . \tag{6}$$

This equation describes the beam ion energy cost as a function of the plasma ion energy cost (ε_p), the extracted ion fraction (f_B), the fraction of ion current to cathode potential surfaces (f_C) and the discharge voltage (V_D).

The first term on the right-hand side of Eq. 6 represents the energy loss associated with producing ions in the discharge chamber and extracting only a fraction of them into the beam. Ions which are not extracted into the beam go to the walls of the discharge chamber where they recombine. The resulting atoms must then be re-ionized before they can contribute to the beam current. Thus the factor $1/f_B$ may be interpreted as the average number of times that a beam ion undergoes ionization before being extracted into the beam.

The second term on the right-hand side of Eq. 6 represents the energy wasted in accelerating plasma ions into interior cathode potential surfaces. This process results in both a discharge energy loss and in the sputter erosion of these surfaces.

To generate performance curves using Eq. 6 one must be able to specify the behavior of each of the terms on the right-hand side of Eq. 6 as a function of the propellant utilization.

Plasma Ion Energy Cost

The plasma ion energy cost parameter, ε_p, appearing in Eq. 6 and defined by Eq. 2 reflects all mechanisms of energy loss from the discharge chamber except for the acceleration of ions out of the plasma through the discharge voltage. Specifically ε_p includes energy losses due to the following mechanisms; direct primary electron loss to the anode, Maxwellian electron collection by the anode, excitation of neutral atoms, excitation of ionic states (which will be neglected) and hollow cathode operation. To derive an expression for the plasma ion energy cost as a function of the propellant utilization an energy balance is made on the discharge chamber plasma represented in Fig. 1. The primary electrons are assumed to be accelerated from a cathode plasma potential that is V_C volts above cathode potential to the potential of the bulk plasma which is assumed to be near that of the anode (i.e. at the discharge voltage (V_D) above cathode potential). Under this assumption as well as the assumption that only the discharge power supply is used to sustain the discharge, energy is supplied to the plasma by the primary electrons at the rate, $J_E(V_D-V_C)$. The "missing" energy $J_E V_C$ is used to operate the hollow cathode. Energy is lost from the plasma primarily by the flux of four types of energy carriers across the plasma boundaries; ions, photons (emitted by de-excitation of excited propellant atoms), Maxwellian electrons, and primary electrons. The ions and

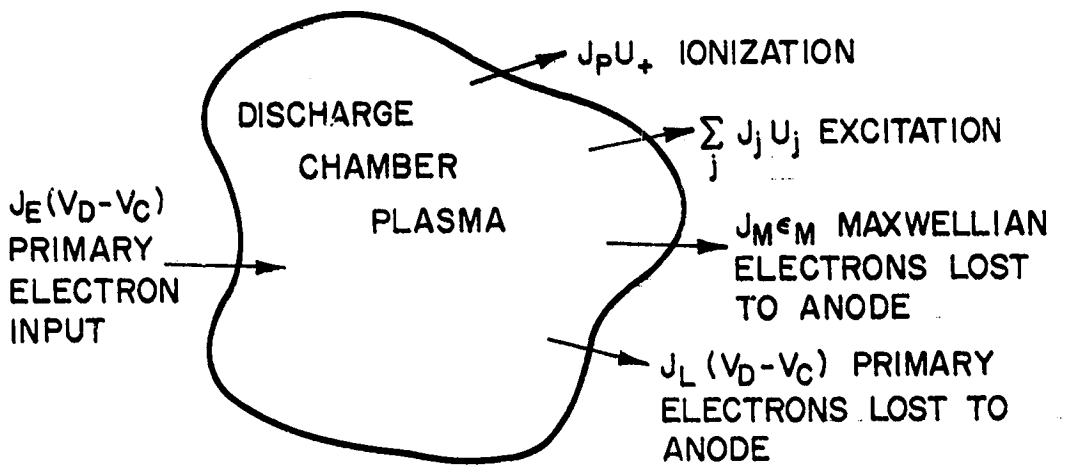

Fig. 1. Discharge Energy Balance Schematic

photons are lost to all interior thruster surfaces whereas the Maxwellian and primary electrons are assumed to be lost to the anode surfaces only. In steady state the rate of energy supplied to the plasma must be equal to the rate at which it is lost, thus,

$$J_E(V_D - V_C) = J_p U_+ + \sum_j J_j U_j + J_M \varepsilon_M + J_L(V_D - V_C) \quad . \tag{7}$$

Dividing Eq. 7 by the ion production current (J_p) and recognizing that the emission current (J_E) is related to the discharge current by,

$$J_E = J_D - (J_C + J_B) \quad , \tag{8}$$

allows Eq. 7 to be written as,

$$\varepsilon_p = U_+ + \frac{\sum_j J_j U_j}{J_p} + \frac{J_M \varepsilon_M}{J_p} + \frac{J_L V_D}{J_p} + \frac{J_E V_C}{J_p} - \frac{J_L V_C}{J_p} \quad , \tag{9}$$

where Eq. 2 has been used. The rate at which the j^{th} excited state is produced is given by

$$J_j = e n_o n_e \langle \sigma_j v_e \rangle \Psi_p \quad , \tag{10}$$

where $\langle \sigma_j v_e \rangle$ represents the product of j^{th} excitation collision cross section and the electron velocity averaged over the electron speed distribution. Similarly, the ion production current is given by,

$$J_p = e n_o n_e \langle \sigma_+ v_e \rangle \Psi_p \quad . \tag{11}$$

Substituting Eqs. 10 and 11 into 9 yields,

$$\varepsilon_p = \varepsilon_o + \frac{J_M \varepsilon_M}{J_p} + \frac{J_L V_D}{J_p} + \frac{J_E V_C}{J_p} - \frac{J_L V_C}{J_p} \quad , \tag{12}$$

where,

$$\varepsilon_o = U_+ + \sum_j \frac{\langle \sigma_j v_e \rangle U_j}{\langle \sigma_+ v_e \rangle} \quad . \tag{13}$$

The third term on the right hand side of Eq. 12 may be written,

$$\frac{J_L V_D}{J_p} = \frac{J_L}{J_E}\left(\frac{J_E V_D}{J_p}\right) = \frac{J_L}{J_E}\varepsilon_p \quad . \tag{14}$$

where the last step was made using Eqs. 2 and 8. The ratio J_L/J_E is simply the fraction of primary electrons emitted by the cathode which are collected by the anode before having any inelastic collisions. This fraction may be given by the survival equation[7] as,

$$\frac{J_L}{J_E} = e^{-\sigma_o n_o \ell_e} \tag{15}$$

where ℓ_e is the average distance a primary electron would travel in the discharge chamber before being collected by the anode - assuming it had no inelastic collisions and σ_o is the total inelastic collision cross section. Combining Eqs. 12, 14 and 15 yields,

$$\varepsilon_p = \varepsilon_o + \frac{J_M \varepsilon_M}{J_p} + \varepsilon_p e^{-\sigma_o n_o \ell_e} + \varepsilon_p \frac{V_C}{V_D} - \varepsilon_p \frac{V_C}{V_D} e^{-\sigma_o n_o \ell_e} \quad . \tag{16}$$

The current of Maxwellian electrons to the anode may be given as the sum of the secondary electrons liberated in the ionization process and the thermalized primary electrons, thus,

$$J_M = J_p + (J_E - J_L) = J_p + J_E(1 - J_L/J_E) \quad . \tag{17}$$

Using Eqs. 15 and 17 in 16 yields

$$\varepsilon_p = \varepsilon_o + \left(J_p + J_E(1 - e^{-\sigma_o n_o \ell_e})\right)\frac{\varepsilon_M}{J_p} + \varepsilon_p\left(e^{-\sigma_o n_o \ell_e} + (1 - e^{-\sigma_o n_o \ell_e})\frac{V_C}{V_D}\right) \tag{18}$$

Finally, using Eqs. 2 and 8 and solving Eq. 18 for ε_p results in,

$$\varepsilon_p = \left\{ \frac{\varepsilon_o + \varepsilon_M}{1 - \frac{V_C + \varepsilon_M}{V_D}} \right\} \left\{ 1 - e^{-\sigma_o n_o \ell_e} \right\}^{-1} \quad . \tag{19}$$

The neutral density, n_o, may be expressed in terms of the propellant flow rate and propellant utilization by equating the rate at which propellant enters and leaves the discharge chamber, i.e.,

$$\dot{m} = J_3 + \dot{n}_o \tag{20}$$

where $\dot{m}$ and $\dot{n}_o$ are in units of equivalent amperes. The neutral flow rate from the thruster may be given as

$$\dot{n}_o = \frac{1}{4} n_o e v_o A_g \phi_o \quad . \tag{21}$$

Combining Eqs. 20 and 21 yields,

$$n_o = \frac{4 \dot{m} (1-\eta_u)}{e v_o A_g \phi_o} \tag{22}$$

where $\eta_u = J_B/\dot{m}$ was used. Thus Eq. 19 may be written,

$$\varepsilon_p = \varepsilon_p^* \left\{ 1 - e^{-C_o \dot{m}(1-\eta_u)} \right\}^{-1} \quad , \tag{23}$$

where,

$$C_o = \frac{4\sigma_o \ell_e}{e v_o A_g \phi_o} \quad , \tag{24}$$

and,

$$\varepsilon_p^* = \frac{\varepsilon_o + \varepsilon_M}{1 - \frac{V_C + \varepsilon_M}{V_D}} \quad . \tag{25}$$

Equation 23 provides a very simple method for calculating the plasma ion energy cost as a function of the propellant utilization. Experimental results, which will be presented in the next section, indicate that under many conditions the parameters C_o and ε_p^* may be taken to be independent of the propellant utilization. Substitution of Eq. 23 into Eq. 6 yields a single equation describing the performance of a given thruster design. For design purposes the parameters f_B and f_C in addition to C_o and ε_p^* may be taken to be independent of the utilization and flow rate. These parameters do, however, depend strongly on the thruster design. Indeed, these four parameters determine the performance of a given thruster design.

The parameter C_o depends on the quality of the primary electron containment (through ℓ_e), the quality of the containment of neutrals (through A_g, ϕ_o and v_o), and the propellant type (through σ_o and v_o). Recall that the primary electron containment length ℓ_e may be interperted as the average distance a primary electron would travel in the discharge chamber before being lost to the anode - assuming it had no inelastic collisions. Magnetic fields in all discharge chamber designs serve the function of increasing this length. Although an effective means of determining ℓ_e remains to be developed it is believed that this parameter is a function primarily of the thruster geometry, magnetic field configuration and cathode location.

Through the parameter C_o, Eq. 23 suggests that the plasma ion energy cost should depend on: the propellant; since different propellants will have different values of the total inelastic collision cross section (σ_o) and different atomic masses, which implies different neutral velocities; the wall temperature, giving rise to different neutral velocities (v_o); the transparency of the grids to neutral atoms (ϕ_o); the area through which the beam is extracted (A_g) and finally, the discharge voltage which determines

the primary electron energy and thus affects the value of the cross section σ_o.

The parameter ε_p^* depends on a number of energy loss mechanisms including the relative amount of energy expended in excitations compared to ionizations of neutral atoms through ε_o, the average energy of the Maxwellian electrons which leave the plasma, ε_m, and the efficiency with which the hollow cathode operates. The cathode efficiency is reflected in the value of V_C which represents plasma potential from which the electrons are supplied. Inefficient cathode operation results in high values of V_C and corresponding poor overall thruster performance. For thermionic cathodes $V_C = 0.$, however, additional heater power must be supplied to effect their operation. The parameter ε_o, defined by Eq. 13, in general depends on the electron energy distribution and may be calculated in the manner discussed by Dugan and Sovie.[8] In spite of the complexity associated with the computation of the parameter ε_p^* it will be shown later that for design purposes it may be taken to be constant for a given discharge chamber design, propellant type and discharge voltage. Thus the model does not necessarily require a detailed knowledge of the electron energy distribution as a function of the propellant utilization to evaluate different thruster designs.

Although the model cannot yet be used to predict the performance of completely new thruster designs it provides a clear physical picture of the phenomena affecting the performance. In order to test several key features of the model the experimental investigation described in subsequent sections was undertaken.

Experimental Apparatus

For this investigation the ion source shown schematically in Fig. 2 was designed and built. This source normally produces a 12 cm dia. ion beam and provides the capability for measuring the distribution of ion currents to the beam, screen grid and internal thruster surfaces (with the exception of the anode).

The magnetic field for this experimental ion source is established through the use of an electromagnet located on the upstream centerline of the discharge chamber and a number of 1.1 cm x 1.3 cm x 0.5 cm samarium cobalt permanent magnets. These permanent magnets are arranged end-to-end to form ring magnets of alternate polarity in the manner suggested by Fig. 2. The flux density at the surface of the magnets is 0.27T and the magnets are attached to the steel discharge chamber housing by their own magnetic attraction. This arrangement allows the ion source magnetic field configuration to be altered quickly and easily by simply adding, removing or changing the position of the magnets. Although many different configurations were tested the results obtained were all similar, thus only those obtained using the configurations shown in Figs. 2 and 3 will be presented. For the configuration shown in Fig. 2 the upstream magnet ring is covered with a strip of 0.13 mm thick steel insulated from the magnets themselves by a strip of 0.25 mm thick mica. This is done so that the surface of this strip can be maintained at anode potential while the rest of the thruster body is at or negative of cathode potential. The downstream magnet ring is uncovered. The magnetic flux density at the surface of the electromagnet can be adjusted from zero to approximately 0.2 T by adjusting the magnet current from zero to 124 A.

The main discharge chamber cathode consists of seven 0.25 cm dia. tungsten wires connected in parallel and supported by two support posts that

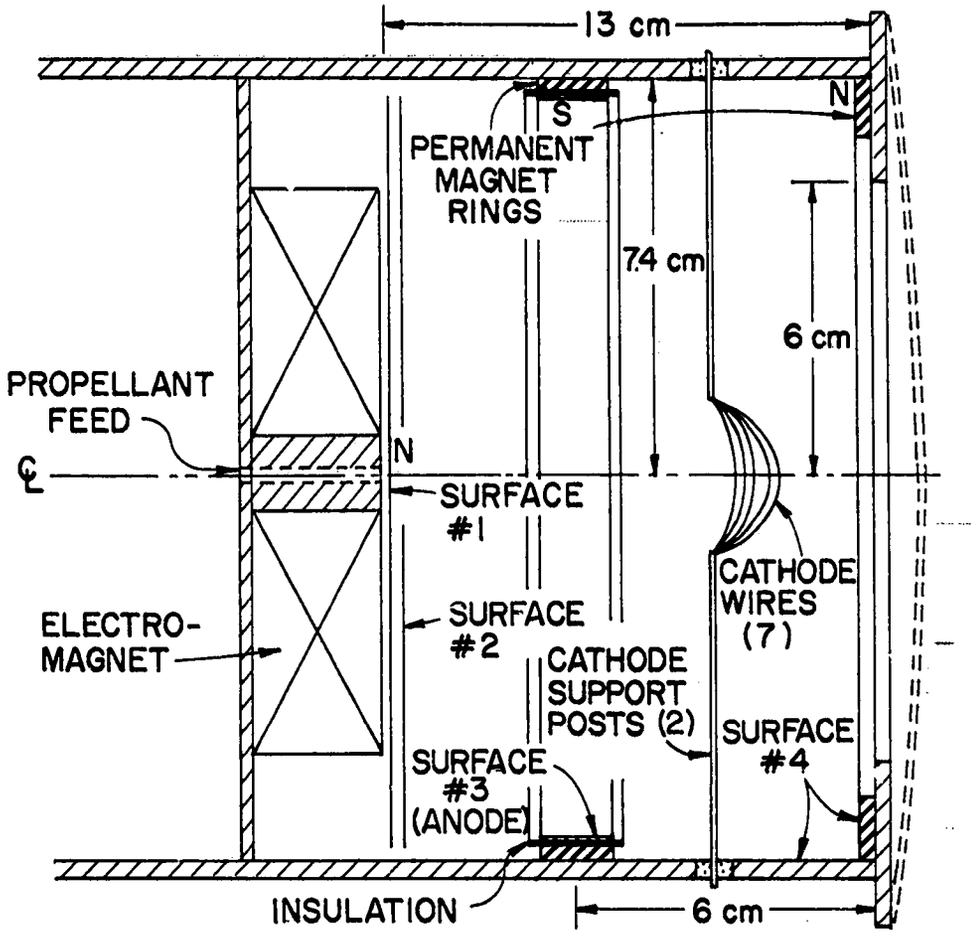

Fig. 2. Ring Cusp Ion Source Schematic

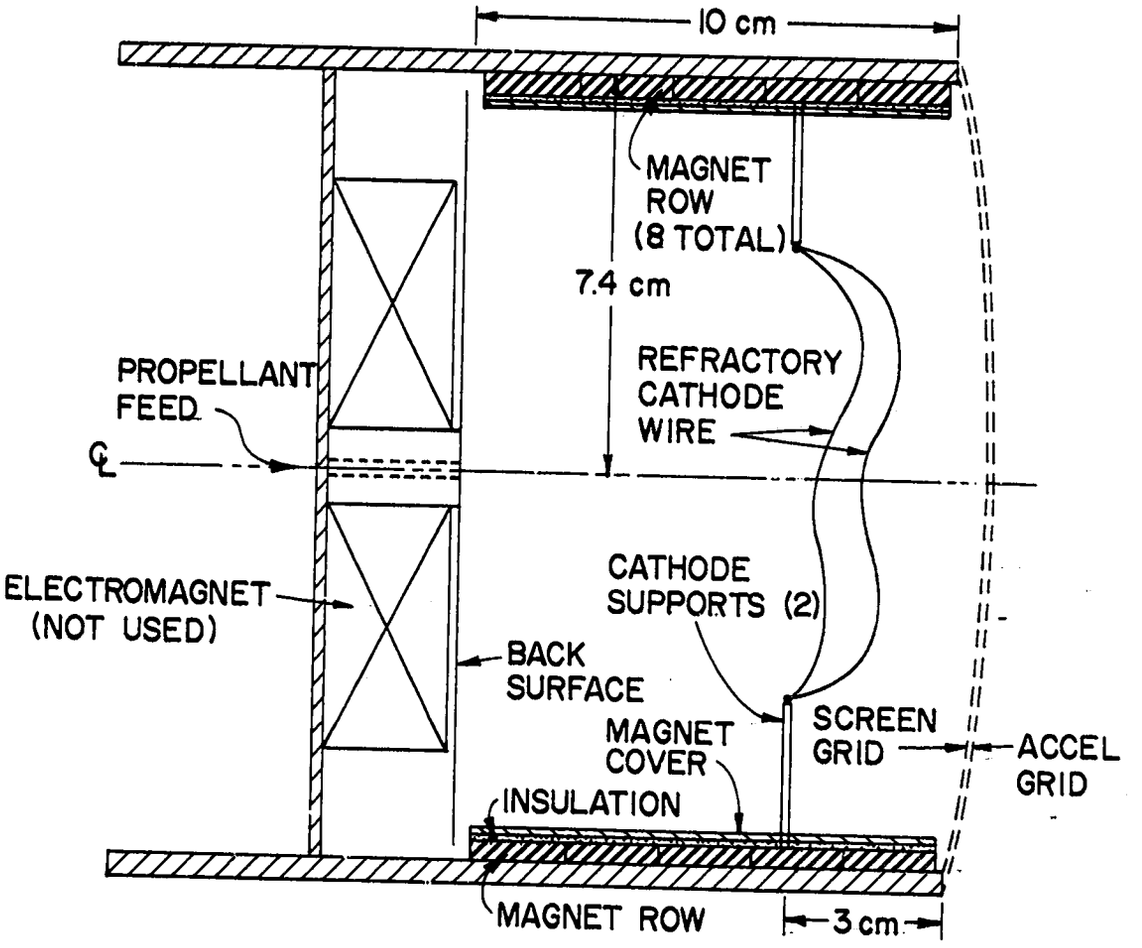

Fig. 3. Line Cusp Ion Source Schematic

are electrically isolated from the thruster body. Each cathode wire is approximately 2.8 cm long so the total cathode length exposed to the plasma is about 19.6 cm. These seven short wires in parallel are used to minimize the voltage drop across the cathode. A voltage drop less than 3 v at the maximum heater current was achieved with this system. It is noted that a small voltage drop across the cathode results in a primary electron energy distribution that more closely resembles the monoenergetic distribution produced by a hollow cathode. The cathode wires were heated using direct currents in the range 6 to 8 A per wire. Tests were conducted using both argon and krypton propellants. Discharge voltages were varied from 30 to 50 v for argon and 20 to 40 v for krypton. The discharge current was adjusted through the range of 0.5 to 5 A for both propellants by controlling the heater current through the refractory cathode wires.

Two ion accelerator systems were used in this study. The first accelerator system consisted of a set of dished small hole accelerator grids (SHAG) with a cold grid separation of 0.75 mm and screen and accelerator grid physical open area fractions of 0.68 and 0.30, respectively. The second system consisted of a set of dished large hole accelerator grids (LHAG) with a cold grid separation of 0.75 mm, and screen and accelerator grid physical open area fractions of 0.68 and 0.57, respectively. Both accelerator systems were normally masked to produce a 12 cm diameter beam. One series of tests was conducted, however, with the SHAG set masked to produce a 6 cm diameter beam. For the 12 cm dia. beam tests flow rates for both argon and krypton were varied from 500 to 1500 mAeq. For the 6 cm dia. beam test the flow rates were varied from 125 to 500 mAeq. All tests were conducted in a 1.2 m dia. x 4.6 m long vacuum test facility. Tank pressures ranged from $\sim 2 \times 10^{-6}$ Torr with no flow to $\sim 3 \times 10^{-5}$ Torr at a flow rate of 1500 mAeq of krypton.

A second series of tests were performed on the line cusp thruster configuration shown schematically in Fig. 3. The magnetic field for the configuration is established using eight rows of samarium cobalt permanent magnets of alternating polarity positioned along the cylindrical discharge chamber side wall. Six of the magnetic rows were maintained at anode potential while the other two (diametrically opposite) rows were biased negative of cathode potential along with the back surface, side wall and screen grid. Tests were conducted over a range of argon propellant flow rates of 600 to 1600 mAeq, discharge voltages of 40 to 50 v and discharge currents of 0.5 to 4.0 A.

Procedure

The following set of experiments was designed to test the ability of the model just developed to predict the functional dependence of the parameter ε_p. The model predicts that the plasma ion energy cost should behave according to Eq. 23 with C_o and ε_p^* given by Eqs. 24 and 25, respectively. The value of ε_p may be determined experimentally through the use of Eq. 2 provided the total ion production current (J_p) and the ion currents to the beam (J_B) and to cathode potential surfaces (J_C) are measured. The total ion production current may be given as the sum of the ion currents leaving the plasma, i.e.,

$$J_p = J_B + J_C + J_A \quad . \tag{26}$$

For these tests the thruster configuration of Fig. 2 was operated with only the upstream magnetic ring at anode potential. All other interior discharge chamber surfaces (with the exception of the cathode support posts) were biased 30 v negative of cathode potential to repel the

discharge chamber electrons and facilitate the measurement of the ion current to those surfaces. Since the only anode surface occurs at a magnetic field cusp the effective area for ion loss to this surface is expected to be less than the physical area.[9-12] Rough calculations indicate that the ion current to the anode with this configuration should be less than a few percent of the total production current. Thus J_p may be approximated as the sum of the ion currents to the beam (including the impingement current) and to the negatively biased discharge chamber surfaces (including the screen grid).

Data consisting of the beam current, propellant flow rate, propellant utilization and total ion production current were collected over the range of operating conditions discussed earlier with the electromagnetic current held constant at 57 A for all cases. Thus the plasma ion energy cost was determined from Eq. 2 for a wide range of operating conditions. In addition, the extracted ion fraction, f_B, given by Eq. 4, was also measured over this same range of conditions.

Results and Discussion

Plasma Ion Energy Cost

Measurement of the plasma ion energy cost for operation of the ring cusp thruster with argon propellant at a 50 v discharge voltage over the range of neutral flow rates from 500 to 1500 mAeq yielded the results shown in Fig. 4. Here the measured values of ε_p are plotted as a function of the quantity $\dot{m}(1 - \eta_u)$ as suggested by Eq. 23. Since this quantity is related to the neutral density in the discharge chamber [Eq. 22] it will be referred to as the neutral density parameter. The solid line in Fig. 4 is the curve given by Eq. 23, where the parameters C_o and ε_p^* have been selected to give the best

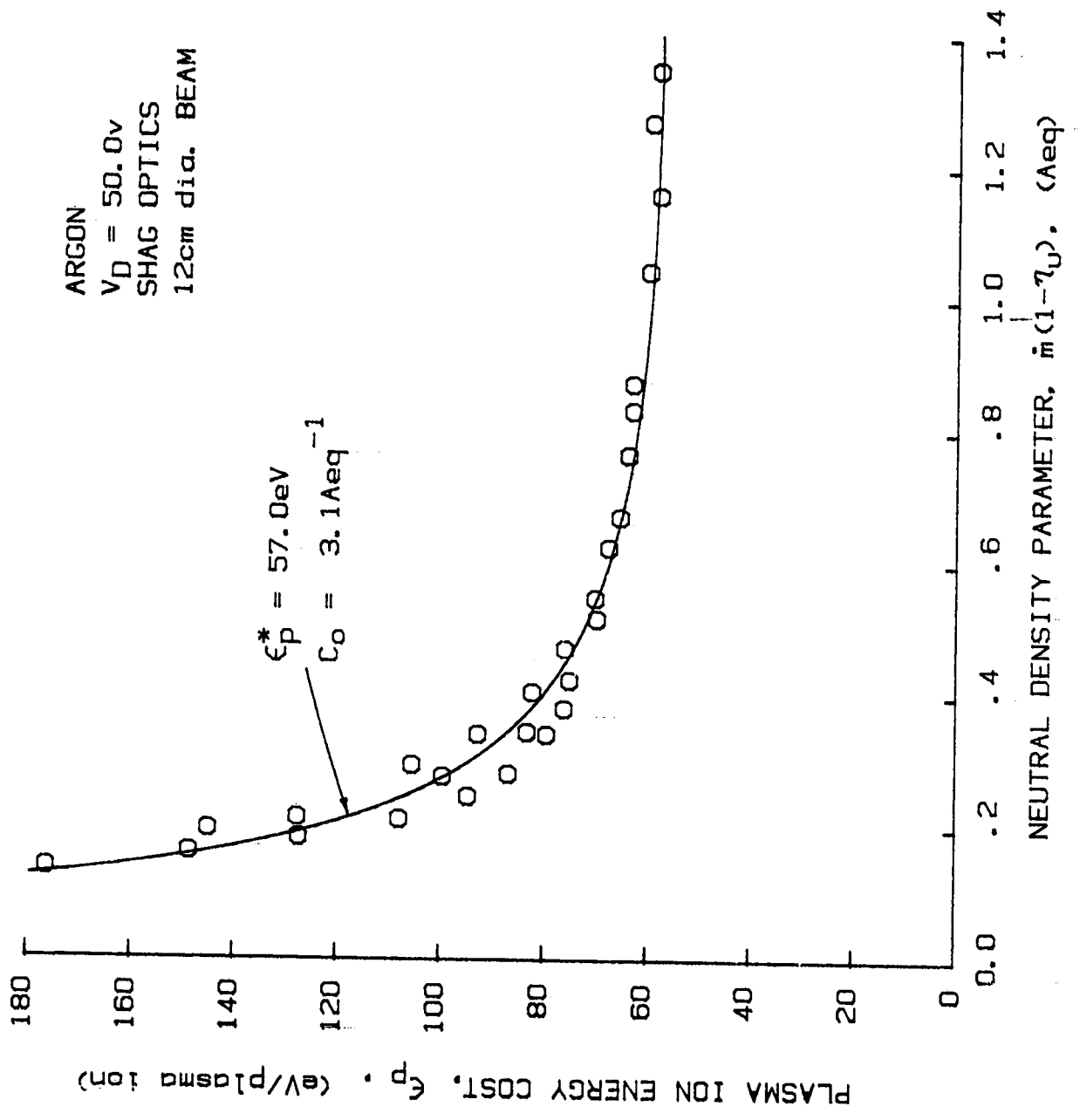

Fig. 4. Baseline Plasma Ion Energy Cost Curve

fit to the data. The parameter ε_p^* was taken to be the value of ε_p measured at large values of the neutral density parameter. The reason for this can be understood by considering Eq. 23, which shows that when $C_o \dot{m}(1 - \eta_u)$ is large then the exponential term is small compared to unity and one obtains $\varepsilon_p = \varepsilon_p^*$. Having established the value of ε_p^* the value of C_o is varied until the best fit is obtained. The agreement between the functional form of Eq. 23 and the experimental data is seen to be quite good. This indicates that the parameters C_o and ε_p^* may indeed be taken to be independent of the neutral density parameter.

We have now established a value of $C_o = 3.1\ \text{Aeq}^{-1}$, which is applicable to the ion source of Fig. 2 operating at the conditions defined in the legend for Fig. 4. New values of C_o applicable to other operating conditions may now be calculated from this value using Eq. 24. For example, changing grid sets from SHAG to LHAG should change the value of C_o through the parameter ϕ_o which is the transparency of the grids to neutral atoms. This effective transparency parameter may be calculated for each grid set according to the equation,

$$\phi_o = \frac{\phi_s \phi_a}{\phi_s + \phi_a} \tag{27}$$

where ϕ_s and ϕ_a are the modified transparencies for the screen and accelerator grid, respectively. These modified transparencies may be calculated as the physical open area fraction of a grid times the appropriate clausing factor.[13] For the two grid sets used in this study we have,

$$\phi_{o_{SHAG}} = 0.16, \text{ and } \phi_{o_{LHAG}} = 0.27 \tag{28}$$

Thus the new value of C_o applicable to the LHAG optics with all other conditions held constant is given by,

$$(C_o)_{LHAG} = \frac{(\phi_o)_{SHAG}}{(\phi_o)_{LHAG}} \; (C_o)_{SHAG}, \tag{29}$$

which yields $(C_o)_{LHAG} = 1.8\ Aeq^{-1}$.

The measured values of ε_p obtained under the same set of conditions defined in the legend of Fig. 4 except for the change in optics from SHAG to LHAG yielded the results shown by the data points in Fig. 5. The solid line is the prediction of the model based on the value of C_o calculated from Eq. 29. The value of ε_p^* was held constant at $\varepsilon_p^* = 57$ eV since changing the optics should not affect this parameter. Clearly the model correctly predicts the variation in the plasma ion energy cost.

The same procedure of calculating a new value of C_o from the old value according to Eq. 24 was followed for the analysis of the data displayed in Figs. 6 through 9. For the data in Fig. 6 the thruster was operated with krypton propellant and SHAG optics at a discharge voltage of 40 v.

The corresponding value of C_o was calculated using the value of C_o obtained from Fig. 4 and the equation,

$$(C_o)_{Kr} = \frac{(\sigma_o)_{Kr}}{(\sigma_o)_{Ar}} \sqrt{\frac{M_{Kr}}{M_{Ar}}} \; (C_o)_{Ar} \tag{30}$$

where both the change in propellant properties and the change in discharge voltage must be accounted for. That is, $(\sigma_o)_{Kr}$ is the total inelastic collision cross section for 40 eV primary electron - krypton atom collisions, whereas $(\sigma_o)_{Ar}$ refers, in this case, to 50 eV primary electron - argon atom collisions. The cross section data needed in this equation were obtained from de Heer, et. al.[14] The new value of C_o calculated from Eq. 30 was $C_o = 5.7\ Aeq^{-1}$, and the corresponding prediction of the model is compared

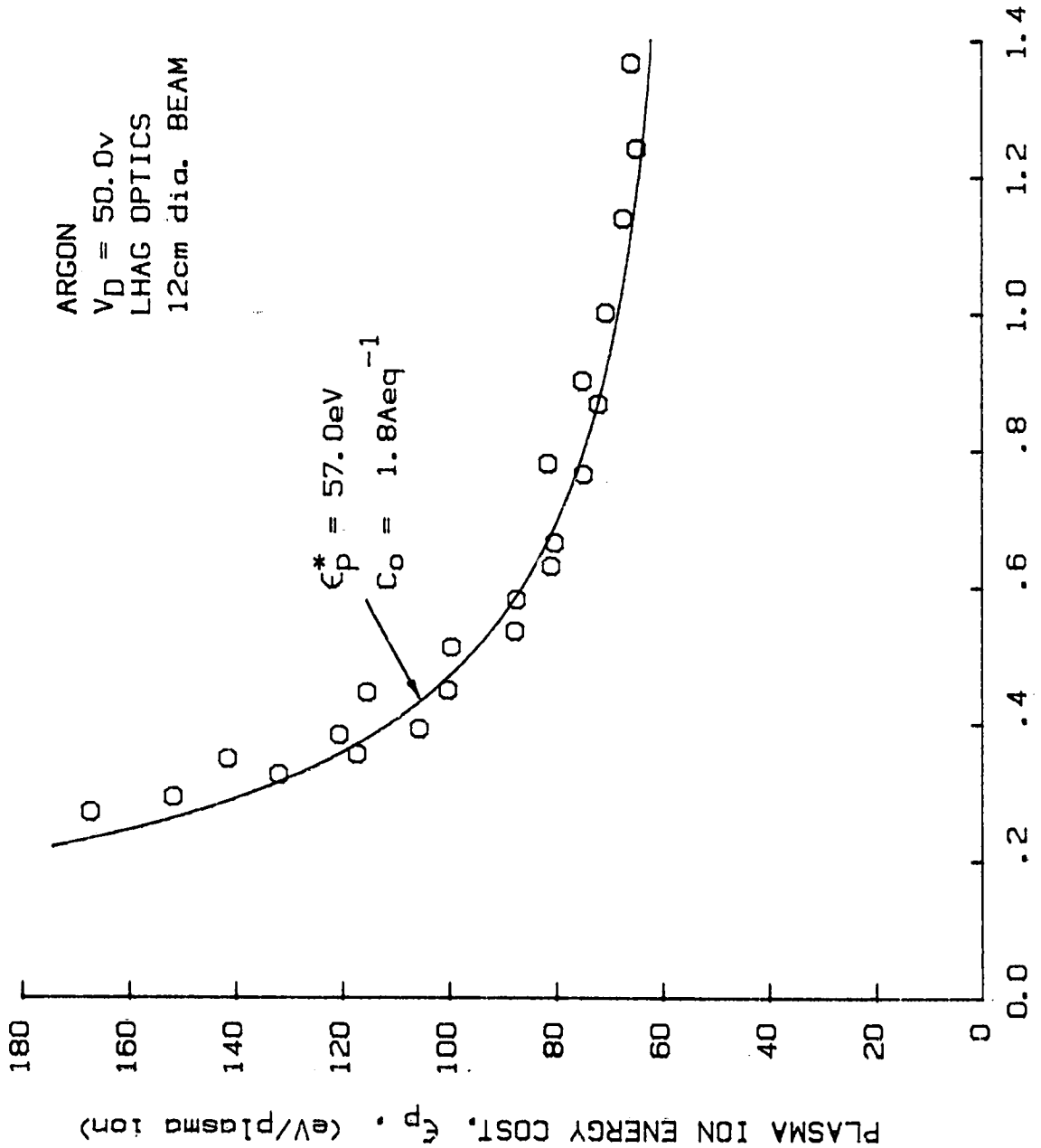

Fig. 5. Plasma Ion Energy Cost Curve with High Grid Transparency

to the measured values in Fig. 6. A new value of ε_p^* was also used for the model in Fig. 6 since this parameter should be a function of both the discharge voltage and the propellant type. Again this new ε_p^* was obtained according to the procedure outlined earlier.

Continuing the same procedure, the prediction of the model based on a calculated new value of C_o is compared to the experimental results for operation with LHAG optics, krypton propellant and V_D = 40 v, in Fig. 7. Again, the agreement between the predicted curve and the experimental data is seen to be good.

From Eq. 24 it is seen that C_o depends inversely on the area of the grids through which the beam is extracted, A_g. This parameter may be varied without changing the discharge chamber diameter by masking down the screen grid to produce ion beams of different cross sectional areas. In this case the screen grid for the SHAG optics set was masked down from a beam diameter of 12 cm to one of 6 cm. This fourfold reduction in beam area should produce a corresponding fourfold increase in the parameter C_o. Therefore, taking C_o from Fig. 6 and multiplying by four yields the new value of $C_o = 22.8\ \text{Aeq}^{-1}$. The model prediction using this value of C_o is compared to the measured values of ε_p in Fig. 8. Remarkably, the agreement between the model and the experiment is excellent. Similar agreement was obtained for operation with argon using the masked down grid set.

Next, the dependency of the plasma ion energy cost on discharge voltage for a given propellant is investigated. For operation with argon at V_D = 40 v a new value of C_o was calculated from the value given in Fig. 4 which was obtained at V_D = 50 v. Again the model agrees well with the measured values as shown in Fig. 9, provided a new value of ε_p^* = 60 eV is used.

For operation at V_D = 30 v with argon, however, the situation is quite

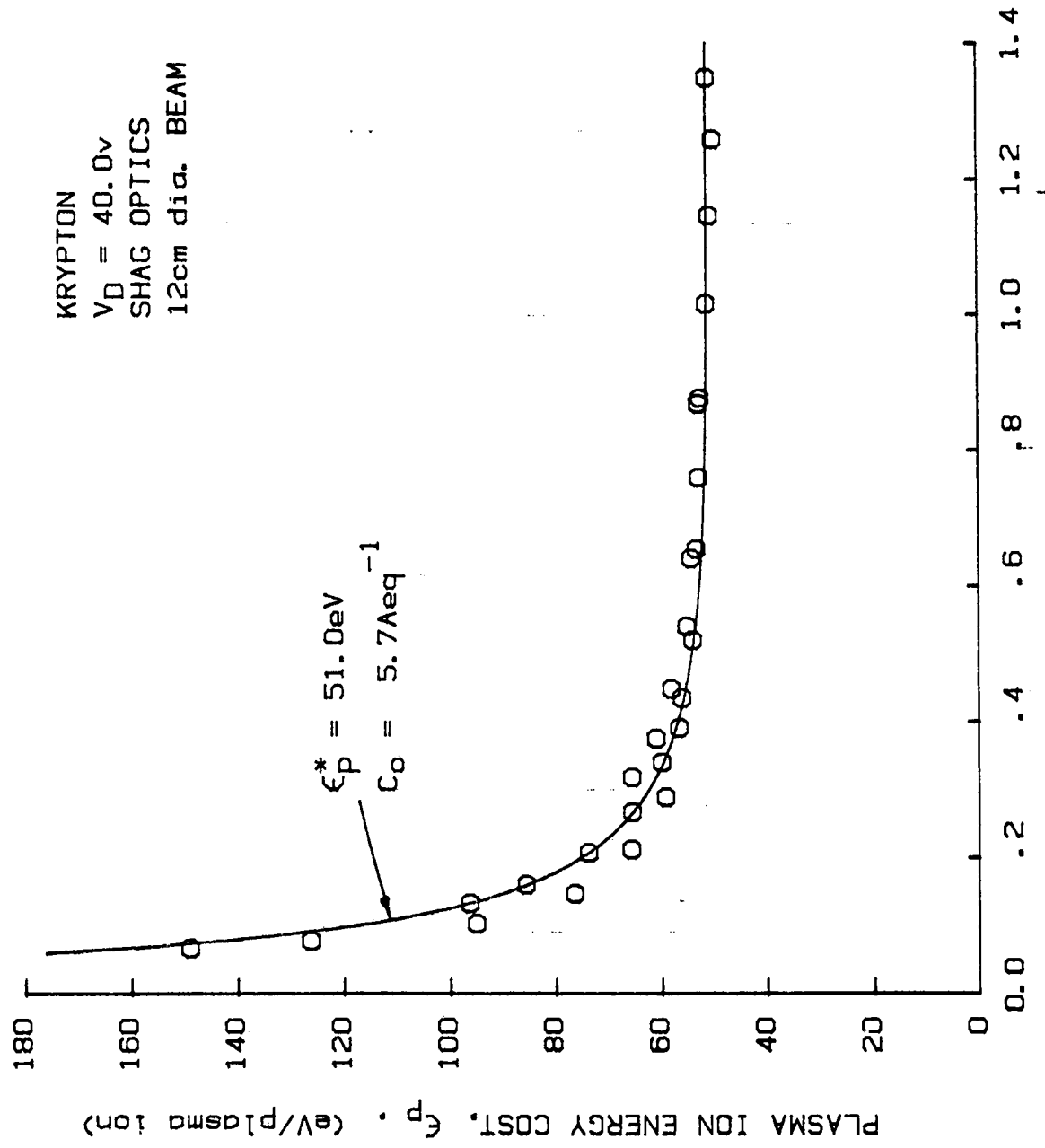

Fig. 6. Plasma Ion Energy Cost Curve for Krypton

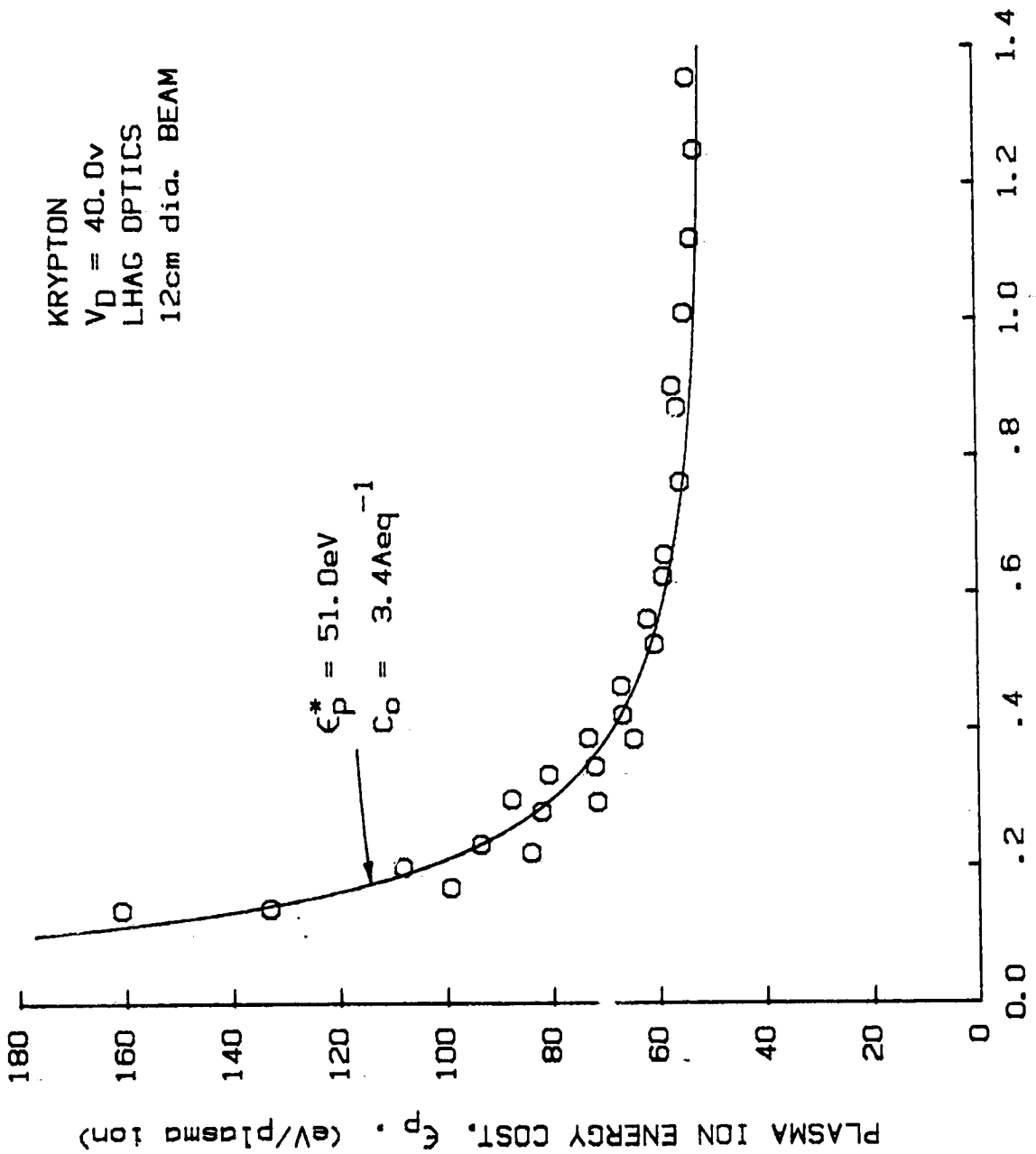

Fig. 7. Plasma Ion Energy Cost Curve for Krypton and a High Transparency Grid Set

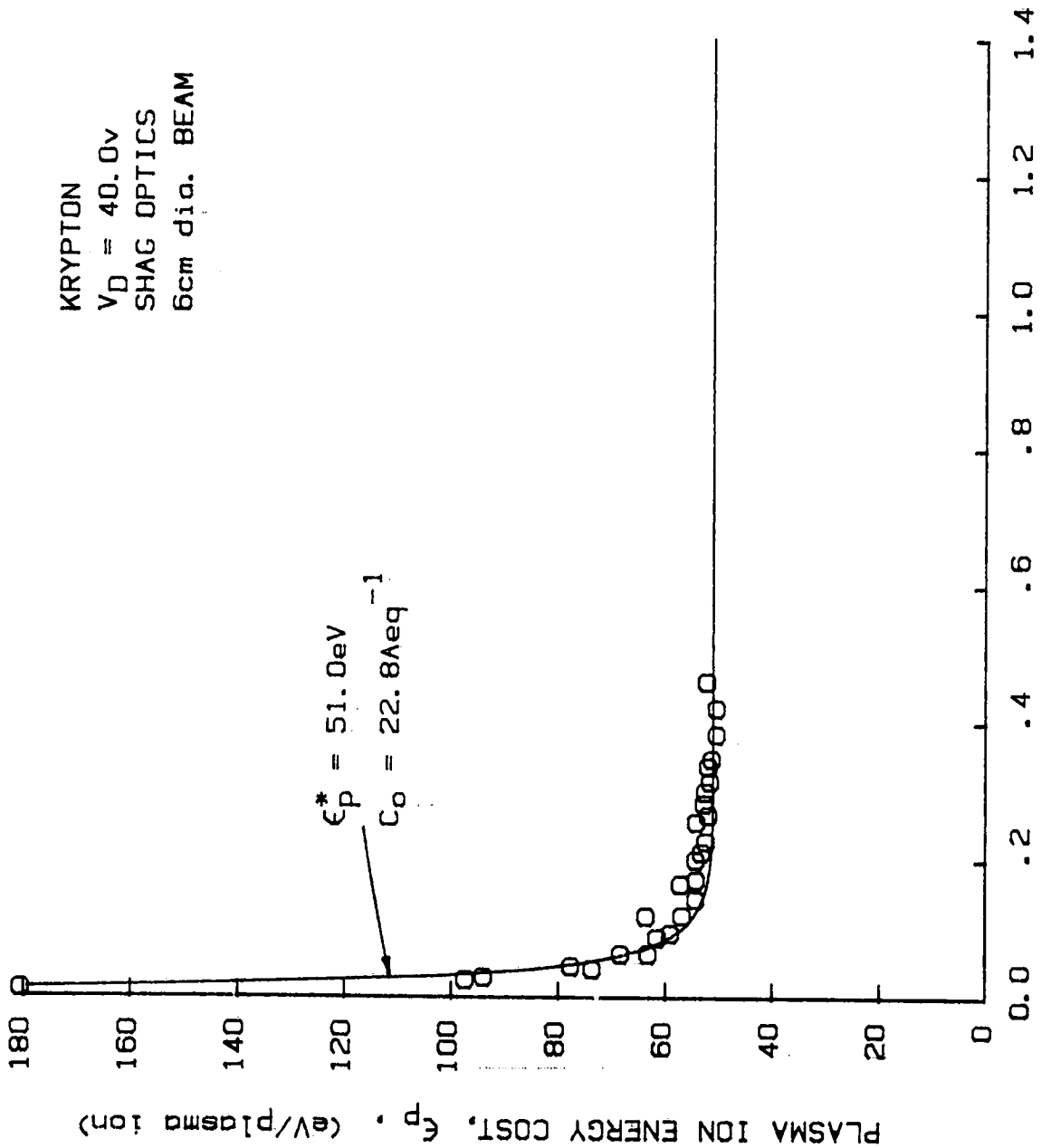

Fig. 8. Plasma Ion Energy Cost Curve for a Small Diameter Ion Beam

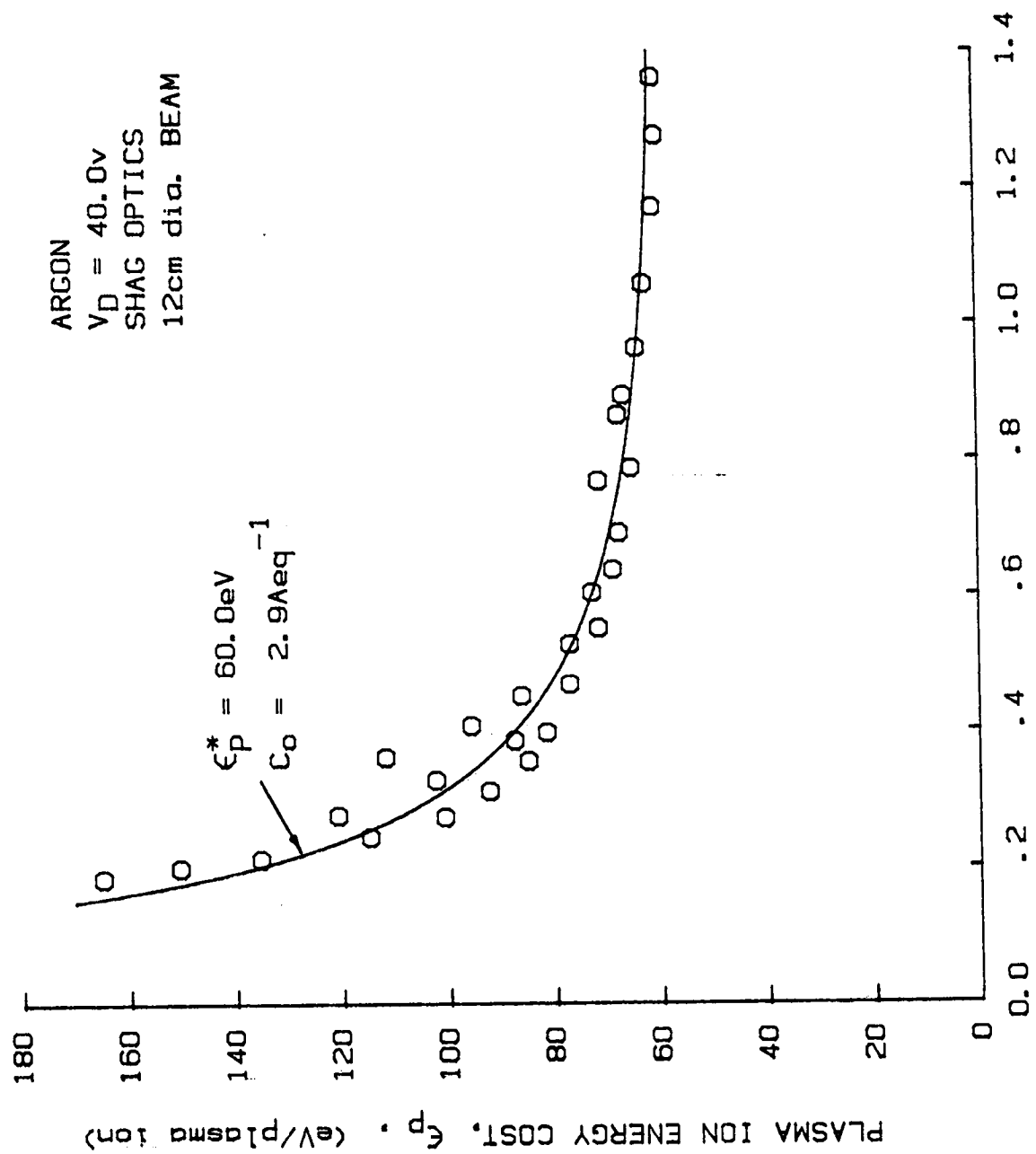

Fig. 9. Plasma Ion Energy Cost Curve at 40 v Discharge Voltage

different as seen in Fig. 10. Here a systematic difference in the data taken at different flow rates is observed. Clearly a single equation such as Eq. 24 is not sufficient to explain this behavior if C_o and ε_p^* are taken to be independent of the neutral flow rate and the utilization. Since the neutral density parameter may be expressed as $\dot{m} - J_B$ we see that a given value of this parameter obtained at different flow rates corresponds to different beam currents. Further, the different beam currents may be roughly translated into different plasma densities. Thus a possible theoretical interpretation of the data in Fig. 10 might be found by looking for C_o and/or ε_p^* to be functions of the plasma density at low discharge voltages.

For krypton propellant, this separation with flow rate was found to occur at a discharge voltage (V_D) of 20 v rather than at the 30 v value observed for argon. This indicates that the separation phenomena depends on the properties of the ions (or neutrals) in the discharge chamber as well as the discharge voltage.

Experiments performed on the line cusp configuration of Fig. 3 indicate that the model is applicable to line cusp as well as ring cusp thruster designs. An example of the results obtained with the line cusp discharge chamber is given in Fig. 11 for operation with argon propellant at a discharge voltage of 50 v. Good agreement between the model and the experiment is obtained for values of $C_o = 1.6\ \text{Aeq}^{-1}$ and $\varepsilon_p^* = 50$ eV.

The results discussed so far indicate that the model for the plasma ion energy cost correctly describes the behavior of this parameter over a wide range of operating conditions. It also indicates that, with the exception of operation at low discharge voltages, the parameters C_o and ε_p^* may be taken to be independent of the neutral flow rate and beam current.

Physically, Eq. 24 describes the plasma ion energy cost in terms of the loss of primary electrons to the anode. At high values of the neutral

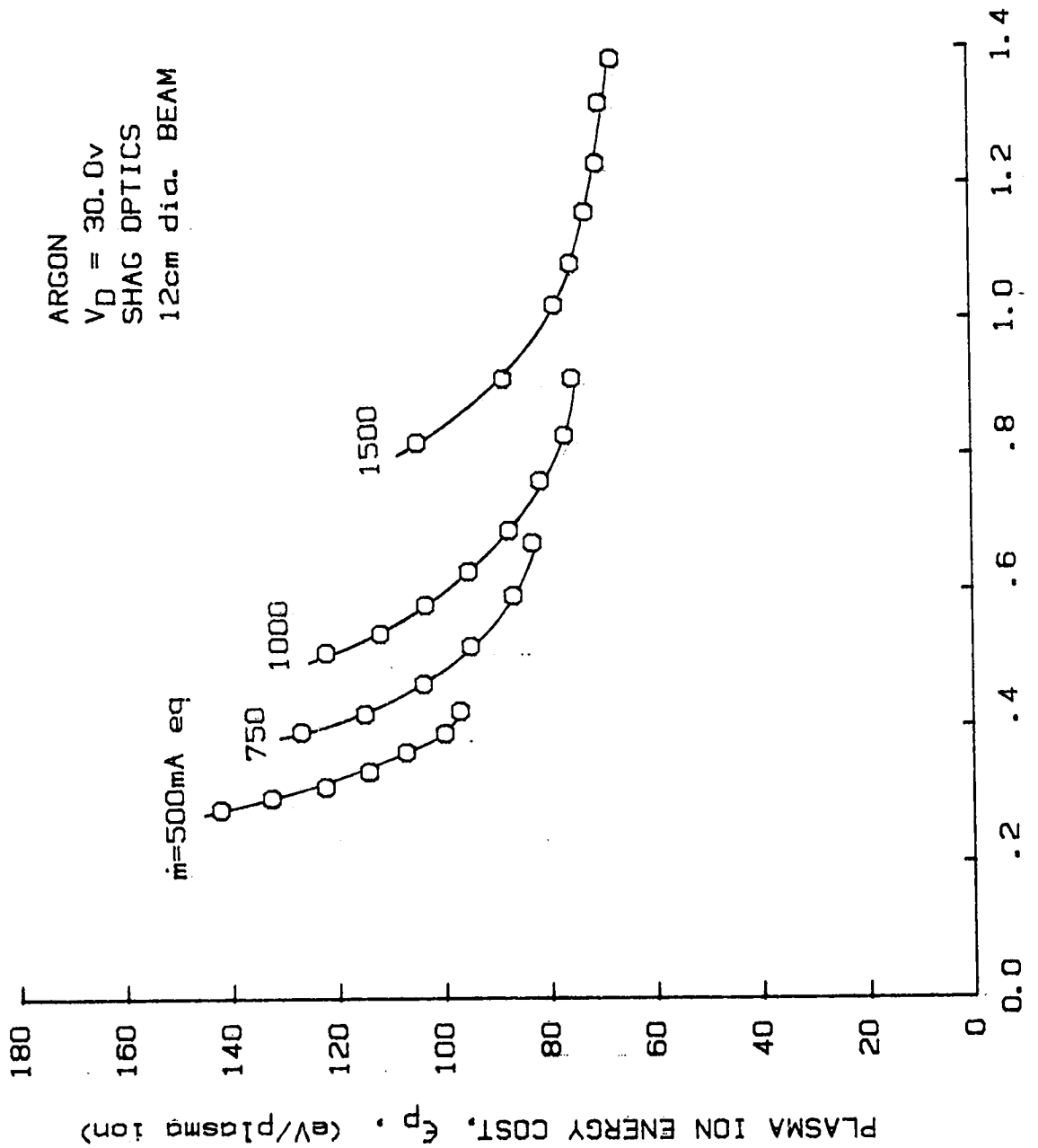

Fig. 10. Plasma Ion Energy Cost Curves at 30 v Discharge Voltage

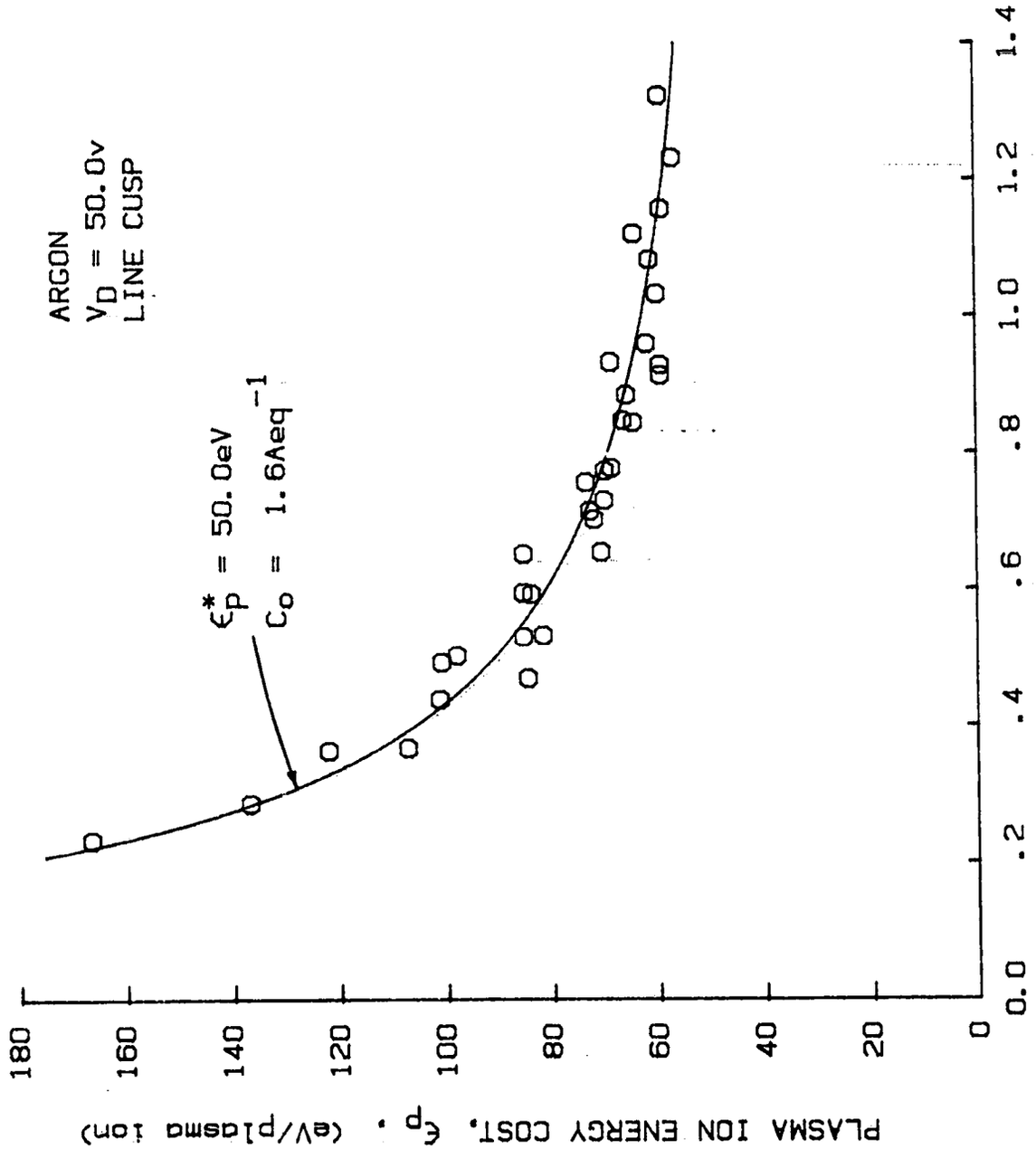

Fig. 11. Plasma Ion Energy Cost Curve for Line Cusp Design

density parameter the neutral density in the discharge chamber is large and the probability is high that all the primary electrons will undergo inelastic collisions with neutral atoms and none will be lost directly to the anode. In this case the discharge chamber will be producing ions for the minimum energy cost, ε_p^*. As the beam current is increased (for a constant flow rate) the propellant utilization increases causing the neutral density parameter and therefore the neutral density to decrease (see Eqs. 20-22). The decrease in neutral density increases the likelihood of a primary electron reaching the anode without first losing its energy. This direct loss of primary electron energy increases the overall plasma ion energy cost according to Eq. 24 and consequently increases the beam ion energy cost according to Eq. 6. Indeed, the shape of the performance curve is largely determined by the direct loss of primary electrons. Thus, any design change which decreases the likelihood of the direct loss of primary electrons (without decreasing the extracted ion fraction) should improve the thruster's performance. The probability of direct primary electron loss is determined through the parameter C_o. This parameter may be increased by either increasing ℓ_e, which makes it harder for primary electrons to escape the plasma, or by making it harder for neutral atoms to escape the discharge chamber.

Now, because the plasma ion energy cost depends on the neutral density parameter and hence on the neutral density itself we are in a position to understand the difference in discharge chamber performance observed for thruster operation with and without ion beam extraction. It has been observed that the performance (eV/beam ion) extrapolated from thruster operation without beam extraction is generally significantly better than the performance measured with beam extraction.[15,16] This may be explained by noting that thruster operation without beam extraction should be characterized by higher

discharge chamber neutral densities than operation with beam extraction at the same flow rate. This must be so since without beam extraction most of the propellant leaves the discharge chamber as neutrals. For the case with ion extraction most of the propellant leaves as ions. Consequently, fewer neutrals leak out through the grids with ion extraction as compared to operation at the same flow rate without ion extraction. This translates into lower neutral densities according to Eq. 21, for the beam extraction case. Further, Eq. 23 written as

$$\varepsilon_p = \varepsilon_p^* \left[1 - e^{- C_o \dot{n}_o} \right]^{-1}, \qquad (31)$$

indicates that the plasma ion energy cost should be higher for smaller values of $\dot{n}_o$. Thus, the performance with beam extraction should be poorer than that extrapolated from data obtained without beam extraction. Finally, it is noted that careful application of the performance model developed here should allow more meaningful extrapolation of data taken without beam extraction to operation with beam extraction.

Extracted Ion Fraction

Aside from the plasma ion energy cost, the other parameter which has a major affect on thruster performance is the extracted ion fraction (f_B in Eq. 6). It is of little use to create ions efficiently in the discharge chamber if only a small fraction are extracted into the beam. The extracted ion fraction, which is defined as the beam current divided by the total ion production current, was measured over the same set of operating conditions described earlier. The resulting data was found not to correlate well with the propellant utilization, where a systematic difference between data taken at different flow rates was observed for all cases. The extracted ion

fraction data was found, however, to correlate well with the neutral density parameter for a reason that has not yet been justified physically.

Values of f_B are presented in Fig. 12 as a function of the neutral density parameter for operation with argon propellant at discharge voltages of both 30 and 50 v over a range of flow rates from 500 to 1500 mAeq. Several things are evident from these data. First, the degree of correlation for the data taken at different flow rates and a fixed discharge voltage is quite good. Second, the extracted ion fraction is greater at the lower discharge voltage. This was true for all sets of data taken. The data taken under the same conditions but at V_D = 40 v falls between the two curves shown in Fig. 12. Third, f_B is seen to increase slightly with decreasing values of the neutral density parameter. Finally, the data taken at V_D = 30 v corresponds to the data in Fig. 10, where we see that the extracted ion fraction still correlates with the neutral density parameter at this low discharge voltage even if the plasma ion energy cost does not.

The extracted ion fractions for argon propellant are compared to those for krypton for V_D = 40 v in Fig. 13. The values of f_B for argon are seen to be generally higher than those for krypton.

It should be pointed out that none of the effects exhibited in Figs. 12 and 13 are understood at this time. Earlier studies indicate that f_B is strongly dependent on the magnetic field configuration.[17,18] However, since f_B is not a strong function of the neutral density parameter and tends to increase only slightly with decreasing values of this parameter, a simple design approach would be to take f_B to be a constant for a given discharge chamber design (magnetic field configuration), propellant, and discharge voltage.

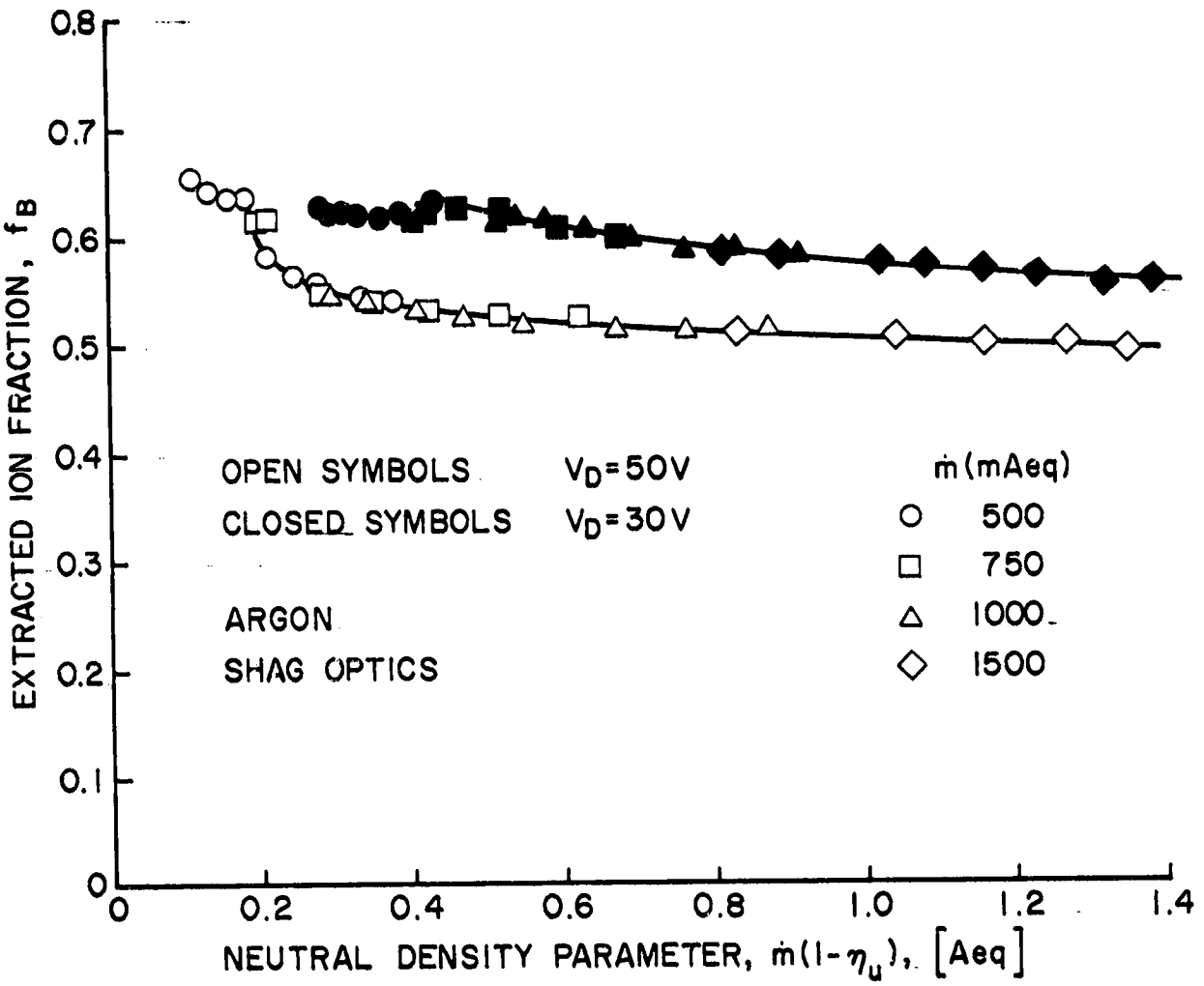

Fig. 12. Extracted Ion Fraction Results

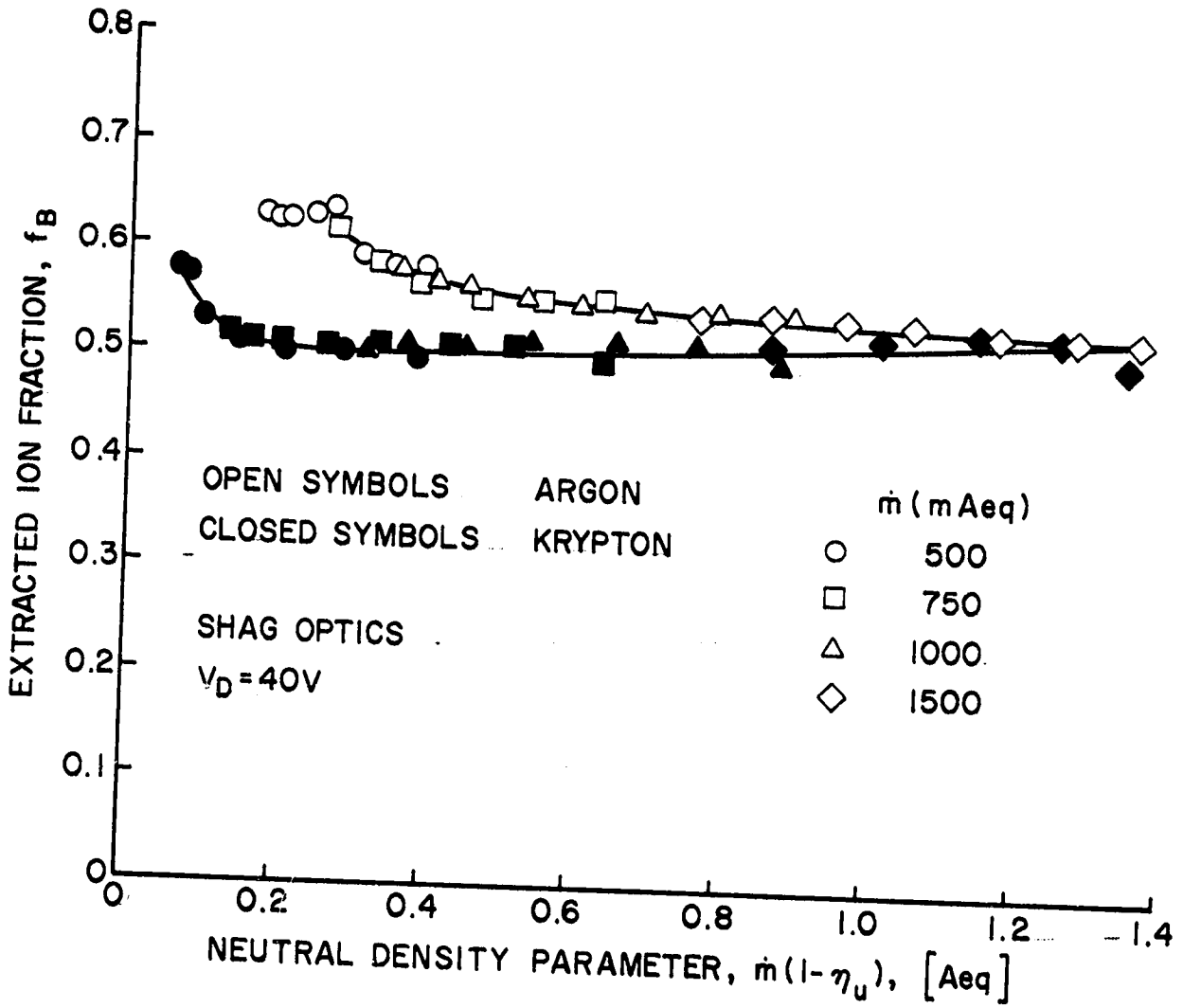

Fig. 13. Extracted Ion Fraction Results

Thruster Design Impact

Combining Eqs. 6 and 23 yields the following single equation describing the performance of a given thruster design,

$$\varepsilon_B = \frac{\varepsilon_p^*}{f_B\left[1 - e^{-C_o\dot{m}(1-\eta_u)}\right]} + \frac{f_C}{f_B} V_D \quad . \tag{32}$$

This equation along with the data just presented suggest that the performance of any thruster design depends on the values of four physical constants[+], ε_p^*, C_o, f_B and f_C; and two operating parameters, $\dot{m}$ and V_D. The effect of some of these parameters on performance was investigated analytically through Eq. 32 by choosing the following set of values as the standard set, then varying them one at a time to determine their effect on the traditional performance curves.

Standard State Parameters

$\dot{m}$ = 1000 mAeq

f_B = 0.6

f_C = 0.1

V_D = 50 v

C_o = 3.0 Aeq^{-1}

ε_p^* = 50 eV

Figure 14 shows the effect of the extracted ion fraction on performance. As expected, this parameter has a strong effect on the performance. As seen

[+] These parameters are constant in the sense that they are independent of the propellant utilization and flow rate.

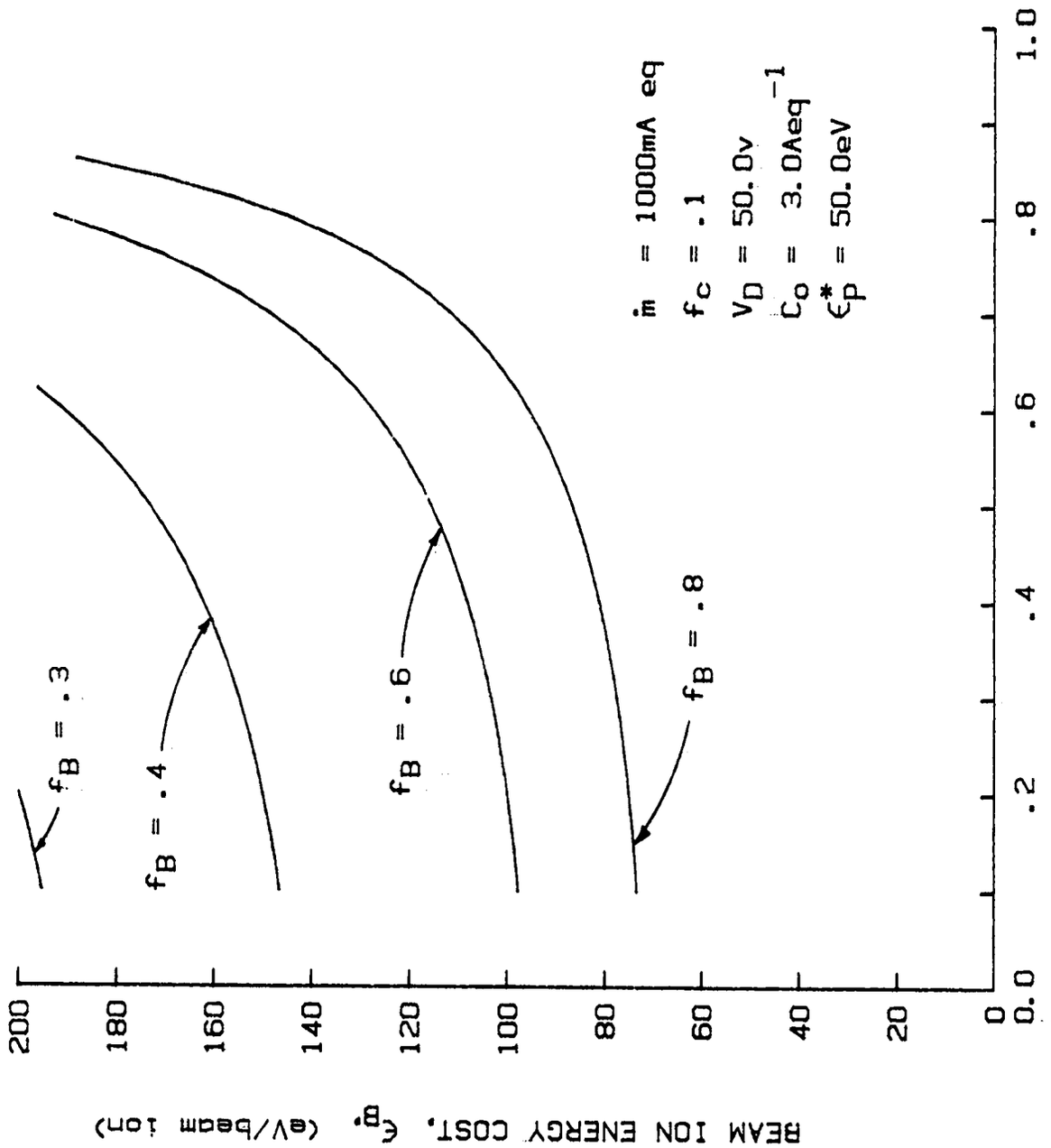

Fig. 14. Effect of Extracted Ion Fraction on Performance

in this figure, changes in f_B shift the performance curve up or down but do not change its shape. Clearly it is desirable to have f_B be as large (near unity) as possible.

The effect of the parameter C_0 on performance is given in Fig. 15. This parameter also has a strong effect on the performance. Indeed, it is this parameter which primarily determines the shape of the performance curve, with larger values of C_0 corresponding to curves with more sharply defined "knees." From the definition of C_0 given in Eq. 24 we see a number of ways in which the value of C_0 may be increased. For example C_0 may be increased by using a propellant gas characterized by a larger inelastic collision cross section σ_0, and a larger atomic mass (resulting in a lower neutral velocity v_0). One may also increase C_0 by decreasing the grid transparency to neutrals, ϕ_0. This must be done, of course, without increasing the accelerator impingement current. For thruster designs with non-uniform beam profiles tailoring the accelerator grid hole size to match the radial current density profile might be a useful way to minimize ϕ_0. Also, three grid systems might be expected to have smaller values of ϕ_0 than two grid systems.

Most importantly C_0 may be increased by increasing the parameter ℓ_e. This parameter corresponds to the average distance a primary electron would travel in the discharge chamber before being collected by an anode surface provided it had no inelastic collisions. As mentioned earlier the primary function of the magnetic field in all thruster designs is to increase this length. In cusped field thrusters primary electrons are lost to the anode through the cusps. Thus ℓ_e may be increased by decreasing the number of cusps at anode potential, but only up to a point. Reductions in anode cusp area below a certain limit will result in unstable operation of the discharge.[19]

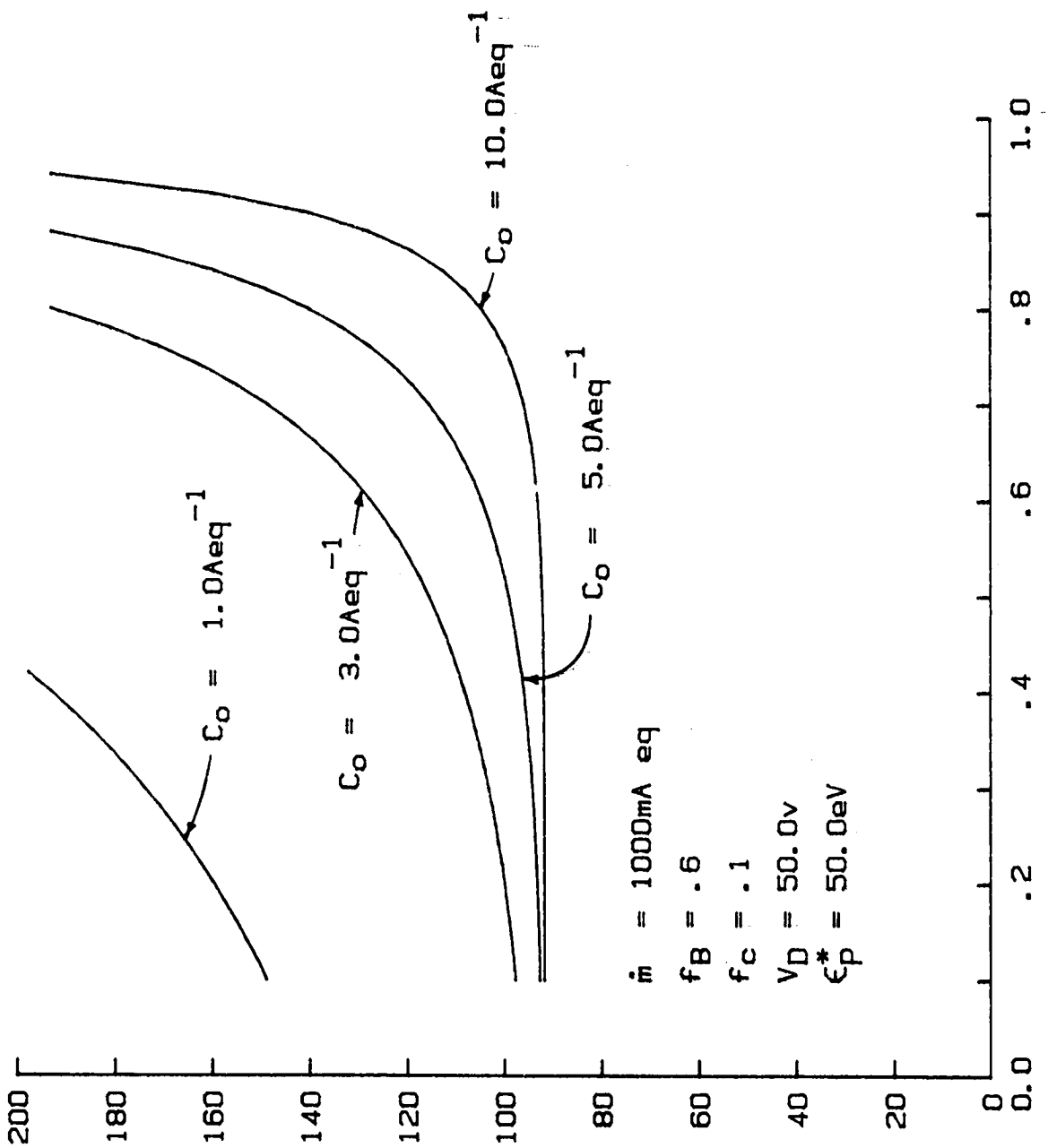

Fig. 15. Effect of C_o on Performance

Equation 24 also suggests that C_o may be increased by masking down the area of the grids through which the beam is extracted, A_g. However, decreasing A_g in this manner will lead to a large reduction in the extracted ion fraction, and therefore an overall reduction in performance.

The effect of propellant flow rate on performance is shown in Fig. 16. In general, higher flow rates produce better performance. The maximum flow rate, however, is limited by the ability of the accelerator system to extract the ion current produced (i.e. to extract $f_B J_p$). The effect of flow rate on performance is less dramatic for thruster designs characterized by larger values of C_o as shown in Fig. 17. High values of C_o would therefore be particularly desirable in thrusters designed to be throttled.

Finally, the effect of ε_p^* on performance is illustrated in Fig. 18. This parameter merely shifts the performance curves up or down. The amount of the shift increases for smaller values of f_B. For thrusters that use hollow cathodes the efficiency of the cathode operation (characterized by V_C in Eq. 25) has a strong effect on the value of ε_p^*. Further, it is the ratio V_C/V_D that is important. Thus larger values of V_D should produce smaller ε_p^*, however, large discharge voltages are undesirable for a number of other reasons. Consequently, a trade off between these conflicting requirements in discharge voltage is necessary.

Neutral Loss

Writing Eq. 20 as,

$$\dot{n}_o = \dot{m} - J_B = \dot{m}\,(1 - \eta_u)\,, \tag{33}$$

and substituting this into Eq. 31, and solving for $\dot{n}_o$ yields,

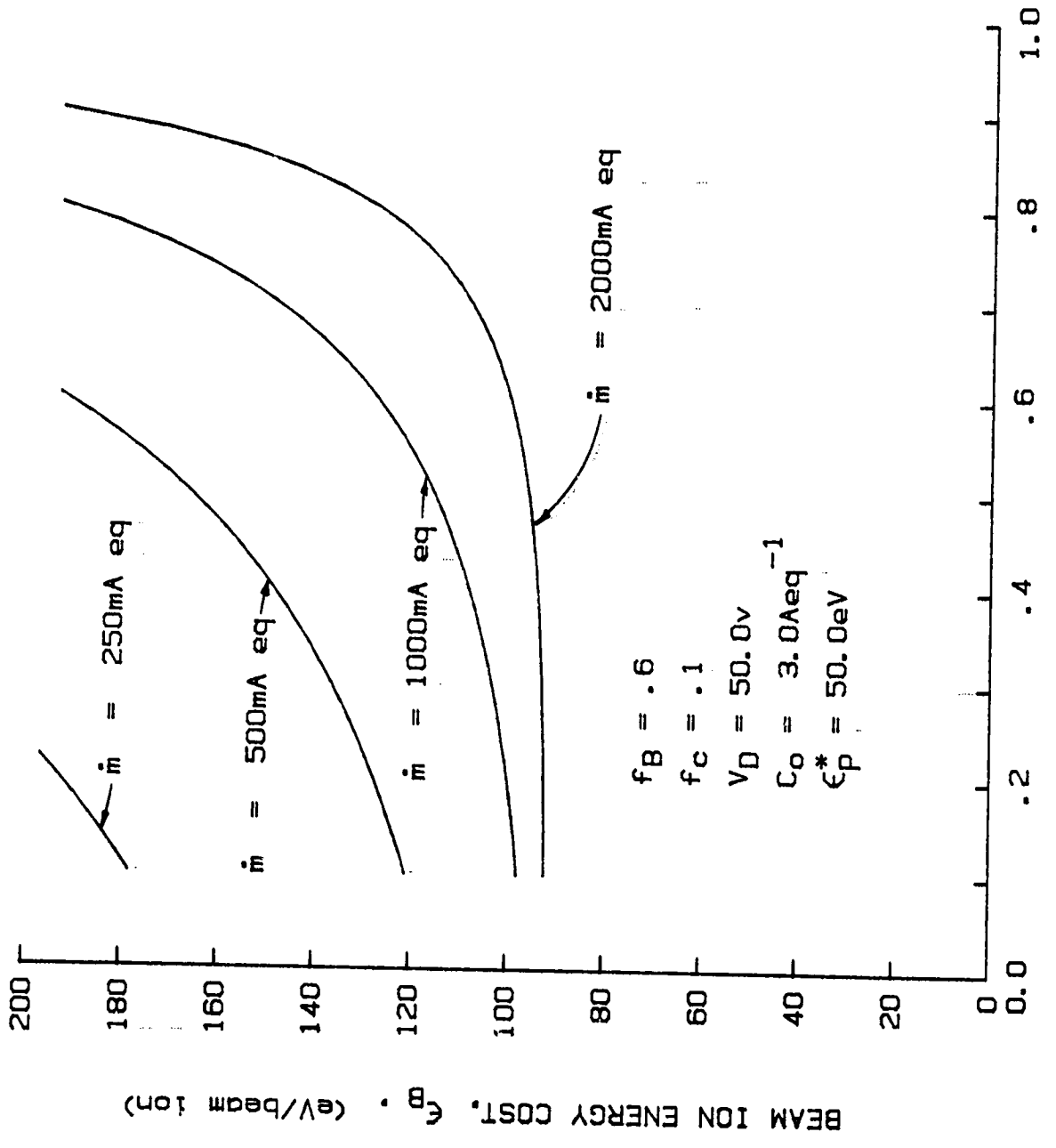

Fig. 16. Effect of Flow Rate on Performance for C_o = 3.0 Aeq^{-1}

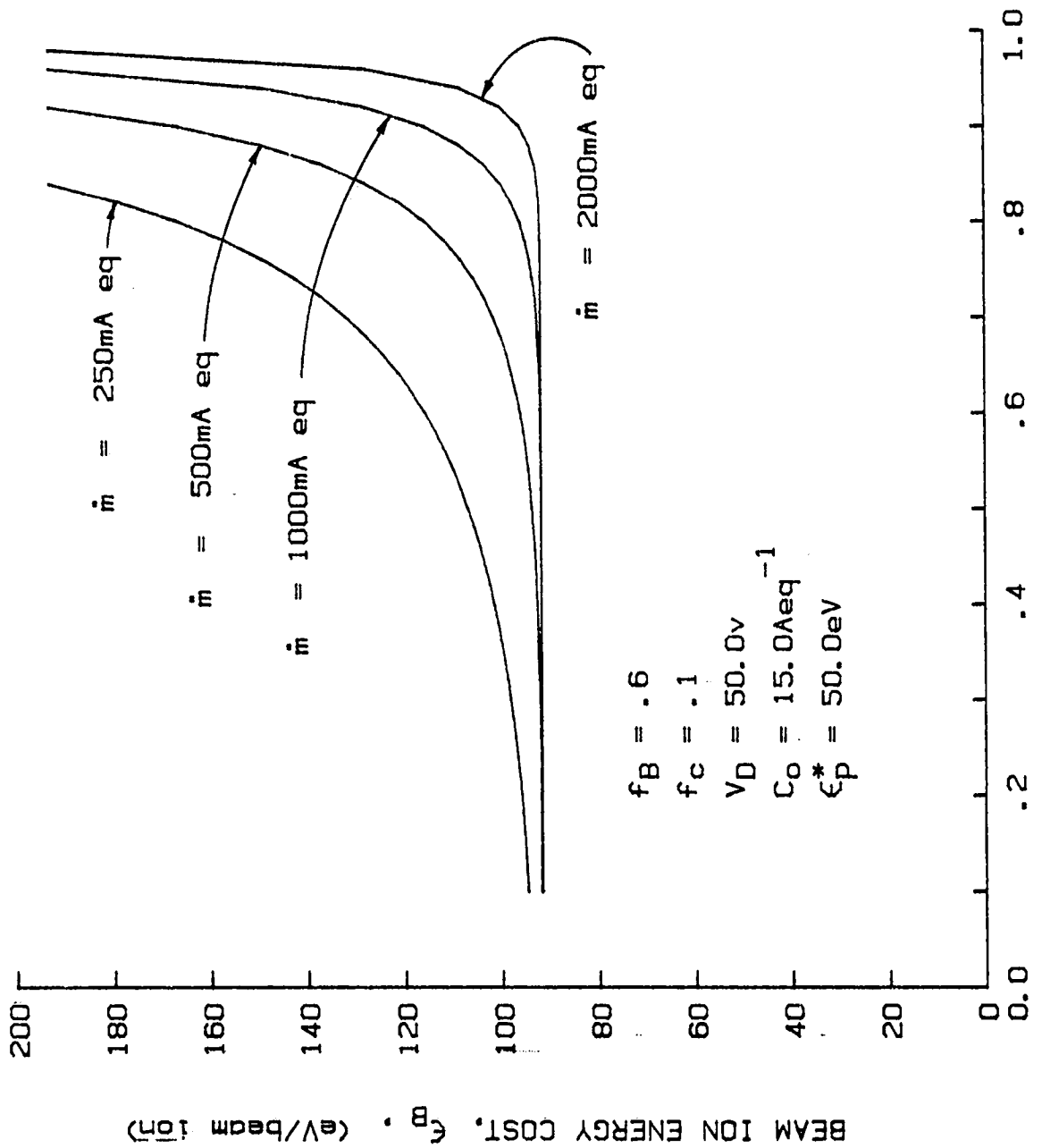

Fig. 17. Effect of Flow Rate on Performance for C_o = 15 Aeq^{-1}

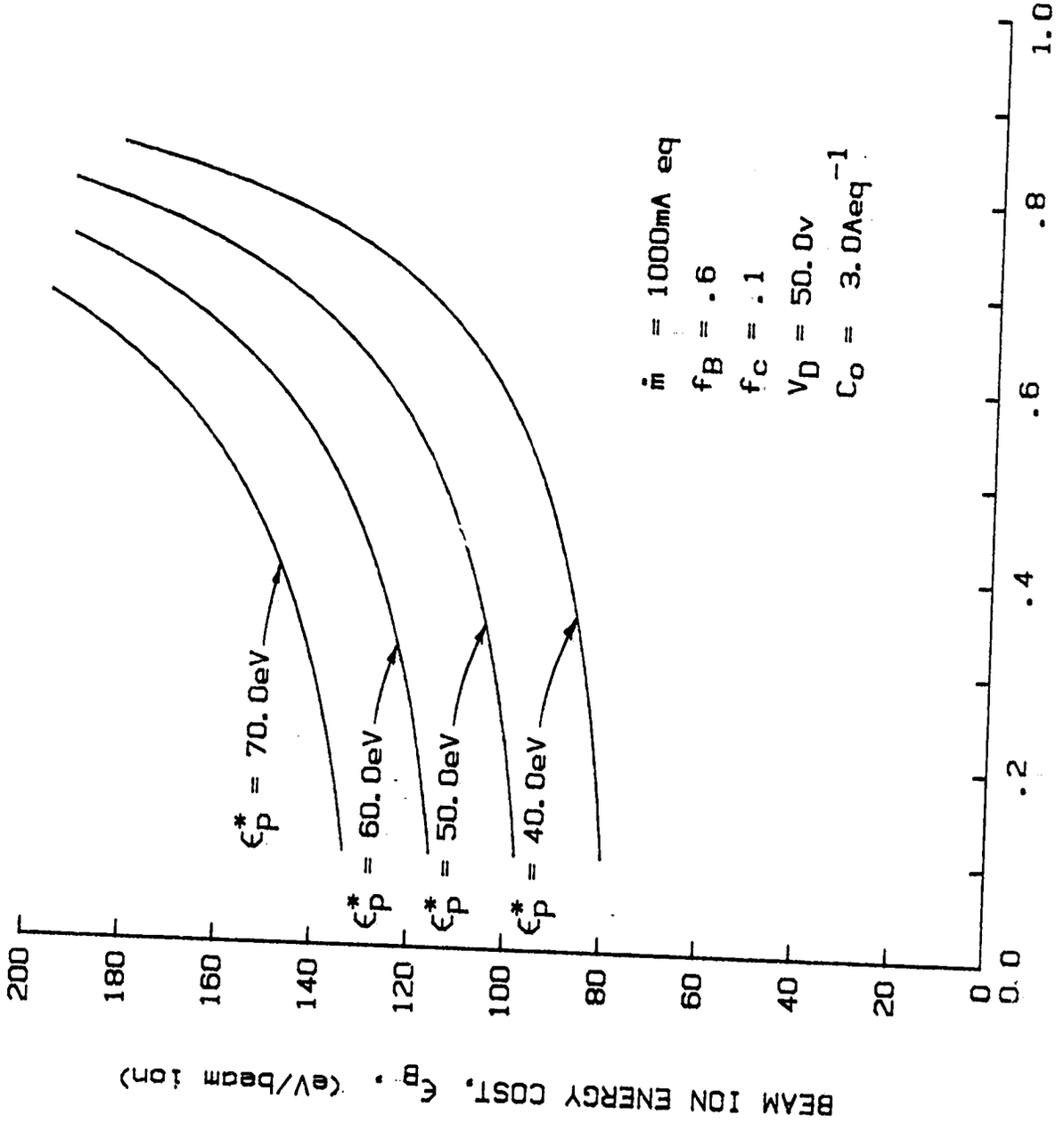

Fig. 18. Effect of ϵ_p^* on Performance

$$\dot{n}_o = -\frac{1}{C_o} \ln\left[1 - \frac{\varepsilon_p^*}{f_B \varepsilon_B - f_C V_D}\right] . \qquad (34)$$

This equation gives the value of the neutral loss rate as a function of the beam ion energy cost. For a specified thruster geometry and discharge voltage C_o, ε_p^*, f_B, g_C and V_D may be taken to be approximately constant as shown earlier. Thus, since the propellant mass flow rate doesn't appear on the right-hand side of Eq. 34, this equation predicts that the neutral loss rate $\dot{n}_o$ is independent of the flow rate for constant values of ε_B. This same conclusion was reached originally by Kaufman[20] in his constant neutral loss rate theory.

Conclusions

A very simple thruster performance model has been developed which is easy to apply as an aid for the design of new thrusters. This model describes the performance in terms of four parameters: the plasma ion energy cost (ε_p), the extracted ion fraction (f_B), the ion current fraction to cathode potential surfaces (f_C), and the discharge voltage (V_D).

The equation developed to describe the behavior of the plasma ion energy cost agrees well with a variety of experimental results. The model and experiments suggest that the direct loss of primary electrons to the anode is the primary factor determining the behavior of the plasma ion energy cost and the shape of the performance curves.

The extracted ion fraction may be taken to be independent of the propellant flow rate and utilization. It does, however, depend on the propellant type and discharge voltage.

For design purposes the thruster performance may be taken to depend

only on four physical constants, C_o, ε_p^*, f_B and f_C and two operating parameters, $\dot{m}$ and V_D.

Improved thruster performance should be characterized by high extracted ion fractions, f_B, large values of the parameter C_o, small values of the parameter ε_p^*.

Future work should focus on determining the dependence of the extracted ion faction f_B and the primary electron containment length, ℓ_e, on the thruster geometry and magnetic field configuration.

THE EFFECT OF DISCHARGE CHAMBER WALL TEMPERATURE ON ION THRUSTER PERFORMANCE

Introduction

For many years it has been assumed that neutral atoms in an ion thruster discharge chamber move at a velocity determined by the mean discharge chamber wall temperature.[5,6,21] By applying this assumption it has been possible to make useful predictions of neutral atom density levels and charge exchange ion production rates in ion thrusters. Application of the assumption also makes it possible to predict that the performance of a discharge chamber can be improved by lowering the mean discharge chamber wall temperature. The extent of the performance improvement that could be induced by such a wall temperature reduction has however not been demonstrated. Further, the validity of the presumed relationship between discharge chamber wall temperature and neutral atom velocity has not been verified experimentally.

The intent of the work described herein has been to demonstrate the extent of performance improvements induced by reductions in wall temperature and to show the discharge chamber model developed in the preceding section of this report describes the magnitude of these improvements correctly. Various perturbing effects that might cause the atom temperature to differ from the mean wall temperature are also examined theoretically.

Theory

The direct measurement of the velocity distribution function or the mean velocity of neutral atoms in an ion thruster discharge chamber is difficult to accomplish but indirect measurements based on discharge chamber performance can be used to infer the neutral atom velocities. In the present case it is assumed that the neutral atoms are in thermal equilibrium with discharge chamber walls and that the relationship between the neutral atom mean velocity and measured discharge performance variables is described in the model proposed by Brophy.[18] It is argued that agreement between measured changes in performance induced by wall temperature changes and those predicted by the model suggest both the model and the neutral atom/wall thermal equilibriation assumption are correct.

While Brophy's model in its complete form is intended to predict complete discharge chamber performance curves, only a portion of the model will be needed here. This portion describes the energy cost of a plasma ion (ε_p) which is the average energy required to produce ions in the plasma. To determine this parameter at each operating condition the following relationship is postulated:

$$\varepsilon_p = \varepsilon_p^*/P_o \tag{35}$$

where ε_p^* is the average energy required to produce an ion in the plasma assuming: 1) no primary electrons are lost to the anode and 2) the primary electrons have inelastic collisions with ground state neutral propellant atoms only. The value of this parameter reflects the facts that energy supplied to the plasma by primary electrons is lost as a result of atomic excitation reactions and Maxwellian electron losses to the anode. Typically ε_p^* is a few times the first ionization potential of the propellant atoms so

it is a function of the propellant. It is also a function of discharge voltage (i.e. primary electron energy).

The parameter P_o in Eq. 35 represents the probability that a primary electron will have an inelastic collision with a neutral atom before it is lost to the anode. Collisions between primary electrons and ions are neglected because neutral densities are typically an order of magnitude greater than the ion densities. However, at high propellant efficiences (high plasma densities) these ionic collisions probably become important and the model would be expected to be less accurate there. The probability P_o is determined by recognizing that it is the compliment of the probability that a primary electron will escape to the anode before losing its energy. This later probability is given by the survival equation,[7] hence

$$P_o = 1 - e^{-\sigma_o n_o \ell_e} \tag{36}$$

where σ_o is the total inelastic collision cross for atom/primary electron collisions at the energy of the primary electrons, n_o is the atom density, and ℓ_e is the average distance a primary electron would travel in the absence of collisions before being lost to the anode. This distance (ℓ_e) will be referred to herein as the primary electron containment length.

Considering only singly charged ions, the neutral flow rate through the grids ($\dot{n}_o$) is simply the difference between the propellant input flow rate ($\dot{m}$) and the ion beam current (J_B) extracted from the thruster

$$\dot{n}_o = \dot{m} - J_B \tag{37}$$

where it is assumed that each of the quantities in the equation are in units of amperes equivalent (A eq.). The neutral loss rate from the ion source may be expressed, however, using the expression for free molecular flow through a sharp-edged orifice.[7]

$$\dot{n}_o = \frac{n_o v_o e A_g \phi_o}{4} \qquad (38)$$

In this equation n_o is the atomic density, e is the electronic charge, A_g is the area of the extraction grid system exposed to the discharge plasma and ϕ_o is the effective transparency of the grid system to neutral atoms. The neutral atom velocity (v_o) in Eq. 38 is the mean thermal velocity for atoms having a Maxwell-Boltzmann distribution function

$$v_o = \sqrt{\frac{8\ kT_o}{\pi m}} \qquad (39)$$

where k is Boltzmann's constant and m is the mass of a propellant atom. The neutral atom temperature T_o is determined by the state of collisional equilibrium achieved between these neutral atoms and the other particles or surfaces with which they interact, in this case, the ions, electrons and discharge chamber wall surfaces exposed to the plasma. Because of the low atom and ion densities in an ion source discharge chamber, which are typically of order 10^{12} cm^{-3} and 10^{11} cm^{-3} respectively, atoms will have frequent collisions with the walls and one would therefore have the first order expectation of an atom temperature near the mean wall temperature ($T_o = T_w$). Using this equality together with Eqs. 35 to 39 one obtains

$$\varepsilon_p = \varepsilon_p^* \left[1 - e^{-C_o(\dot{m} - J_B)}\right]^{-1} = \varepsilon_p^* \left[1 - e^{-C_o \dot{m}(1 - n_u)}\right]^{-1} \qquad (40)$$

where

$$C_o = \frac{4\sigma_o \ell_e}{e A_g \phi_o} \sqrt{\frac{\pi m}{8\ kT_w}} \ . \qquad (41)$$

The suitability of Eqs. 40 and 41 to describe correctly the relationship between the energy cost of a plasma ion (ε_p) and the neutral density

parameter $\dot{m}(1 - \eta_u)$, where η_u is the propellant efficiency, has been demonstrated experimentally by Brophy in tests reported in the preceding section of this report. It has been shown that changes in grid transparency (ϕ_o), grid area (A_g) and propellant type (through the cross section [σ_o] and the propellant atomic mass [m]) are correctly modelled by these equations.

In this paper experiments, in which the relationship between energy cost of plasma ions and the neutral density parameter is quantified in terms of the coefficient ε_p^* and C_o, are described. It is argued that ε_p^* is independent of wall temperature and that C_o is affected by it only through the explicit dependence shown in Eq. 41. Changes in the values of C_o predicted by Eq. 41 due to changes in wall temperature are compared to measured changes in C_o induced by wall temperature changes in an operating ion source.

Apparatus and Procedure

In order to study experimentally the influence of discharge chamber wall temperature on discharge chamber performance, the ion source shown schematically in Fig. 19 was built. It is similar to the source shown in Fig. 2 which was built to study the effects of discharge voltage, propellant, grid extraction area and transparency on discharge chamber performance. The primary difference between these sources is the cooling coil installed for this experiment (Fig. 19). This coil, which was made using 1.3 cm dia. copper tubing compressed until it deformed plastically onto the steel shell, can be connected to a liquid nitrogen source. The liquid nitrogen flow rate through the coil is adjusted to control the steel shell temperature at values ranging from $\sim$ 80°K to $\sim$ 500°K. The heat transfer area and contact thermal conductance are sufficiently high so wall temperatures measured using the iron-constantan thermocouples shown in Fig. 19 are within $\sim$ 10°K of the liquid nitrogen boiling point (77°K) when the ion source is operated at maximum power.

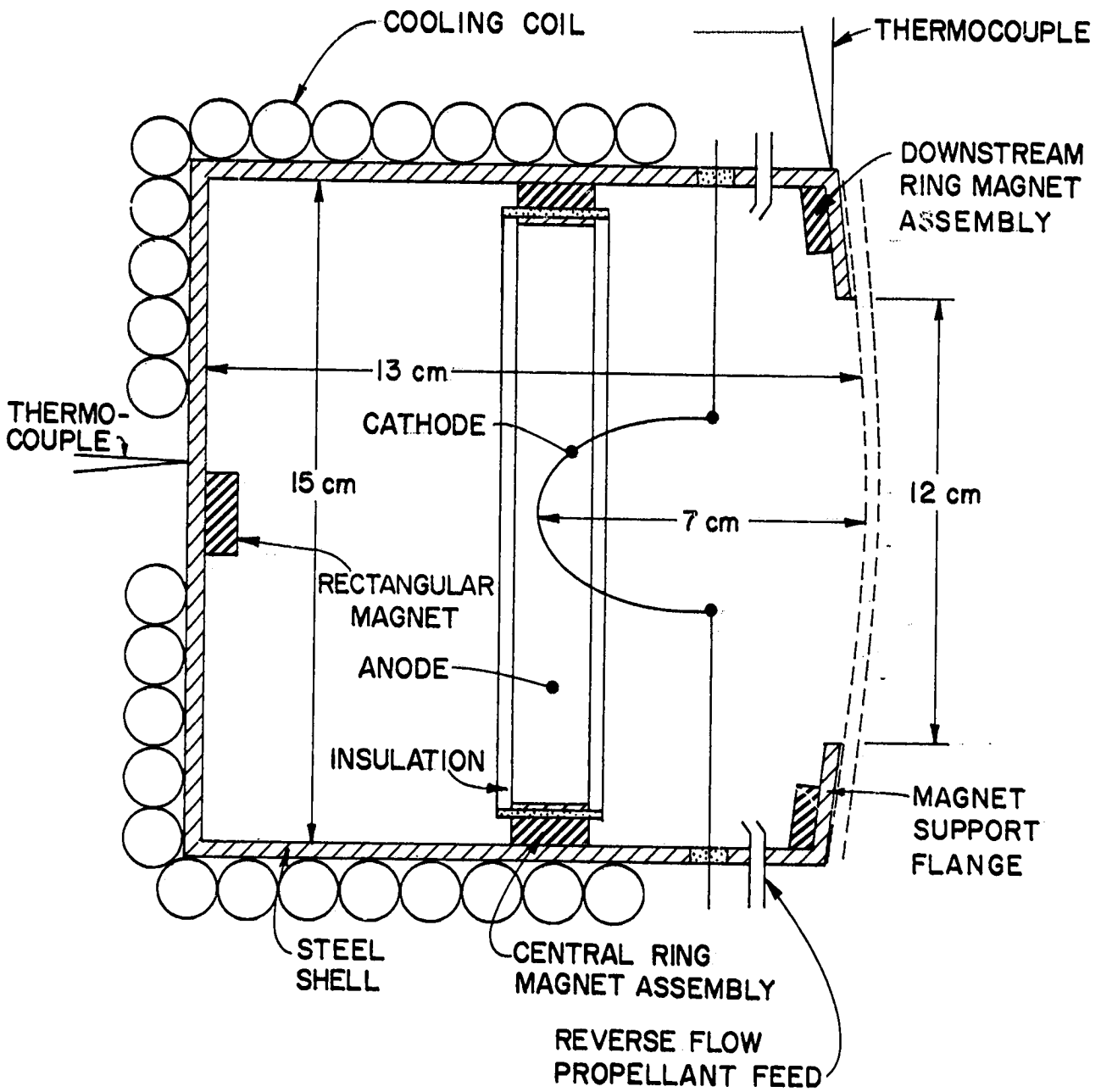

Fig. 19. Liquid Nitrogen Cooled Ion Source Schematic

The ion source of Fig. 19 has a 15 cm inside diameter steel shell but the screen grid is masked down by the magnet support flange so the ion beam diameter is only 12 cm. The magnetic field in the discharge chamber is produced by the upstream 1.9 cm x 2.6 cm rectangular magnet, the central ring magnet assembly and the downstream ring magnet assembly shown in Fig. 19. Each of the magnet assemblies shown has been made by placing 1.9 cm x 1.3 cm x 0.5 cm thick samarium cobalt magnets end-to-end and side-to-side to form the rings and the rectangle respectively. The flux density at the surface of the magnet assemblies is 0.27 T and they are arranged so the inner surface of the central ring magnet has a polarity opposite to those at the inner surface of the rectangular and downstream magnet assemblies. The central ring magnet assembly is insulated from the strip of 0.13 mm thick steel that serves as the discharge chamber anode shown in Fig. 19 by a piece of 0.076 mm thick flexible mica. Both the magnet assemblies and the anode are held in place by magnetic attraction forces between the magnets, the steel anode and the steel shell.

In designing and building the discharge chamber special attention was given to features that would minimize temperature differences between points on the discharge chamber wall and between the walls and the grid assembly. For example, the steel shell is 0.5 cm thick and joints in the shell are silver soldered together. The magnet support flange, which is made of 0.18 cm thick copper, is also soldered to the shell. A 0.7 mm thick steel ring is sandwiched in close mechanical contact between the copper flange and the magnet ring. The screen grid is clamped directly to the copper flange. The molybdenum screen grid is 0.43 mm thick and has a physical transparency of 68%. The molybdenum accel grid is 0.53 mm thick and has a physical transparency of 57%. The screen and accelerator grids were held at + 1kV and -0.5kV respectively during the conduct of the tests.

A pair of 0.25 mm dia., 8 cm long tungsten wires, connected in parallel and heated to thermionic emission temperatures by passing an alternating current through them, serves as the cathode. The maximum cathode power applied at the highest electron emission condition required for these tests was ∿ 200 w. The source was designed so that either argon or krypton propellant could be fed into it through the reverse flow feed line shown in Fig. 19. Flow rates of 500, 1000 and 1500 mAeq. were used for both propellants. With argon the discharge voltage was maintained at 50 v and with krypton 40 v was used. These voltages were selected as sufficient to yield stable discharge operation yet low enough to limit doubly charged ion production.

A special feature of the thruster was that the screen grid, downstream ring and rectangular magnet assemblies, steel shell and magnet support flange were all connected in parallel to a power supply that could be used to bias these surfaces relative to cathode potential. By biasing these surfaces ∿ 30 v negative of cathode potential all discharge chamber electrons could be repelled from these surfaces and as a result the ion current to them could be measured. Adding this current to the beam current one obtains a value for the ion production rate (J_p). The error between this measured ion production rate and the true one is equal to the ion losses to the anode which have not been included in the measurement. This error has been estimated to be less than a few percent based on the effective area for ion loss to the anode compared to other ion loss areas. Using the measured ion production rate (J_p) the energy cost of a plasma ion (ε_p) can be computed using the expression derived in the preceding section of this report

$$\varepsilon_p = \frac{(J_D - J_p)V_D}{J_p} \quad . \tag{42}$$

In order to conduct the tests, the ion source was first allowed to stabilize thermally at a low discharge current level and a fixed propellant flow rate and discharge voltage. The discharge current was then increased in increments by increasing the cathode filament current while the flow rate and discharge voltage were held constant. At each discharge current the beam current and ion current to the steel sheel and screen grid were recorded along with the discharge current. This procedure was repeated at three different flow rates for each wall temperature condition for argon and krypton propellants. The data were evaluated by computing the total ion production current as the sum of the beam current and ion current to the screen grid and shell to find the total ion production rate. Equation 42 was then used to determine the energy cost of a plasma ion. A parameter proportional to the neutral density was also computed as the difference between the neutral propellant flow rate in Aeq and the beam current.

Error Considerations

Since the temperature of propellant atoms in the discharge chamber is determined by collisions with wall surfaces and influenced by discharge plasma ions and electrons there are two general sources of errors that could cause the atom temperature to differ from the measured mean wall temperature. They are errors due to 1) variations in wall temperature that complicate the computation of the appropriate mean temperature from measured values and 2) perturbations in the atomic temperature induced either by atomic collisions with electrons and ions or an influx of atoms having energies that differ markedly from those associated with the mean wall temperature. The magnitude of errors that might be expected from these two effects will now be considered separately.

Wall Temperature Variation Effects

The worst case wall temperature variations are realized when the discharge chamber and cathode are being operated at maximum power. At this operating condition it is estimated that 200 watts of power could be radiated from the cathode and the plasma. This power would generally be assumed to be distributed uniformly over the interior surfaces of the chamber. Other power losses to the walls are associated with electron and ion losses to these surfaces. Electrons are assumed conservatively to have an average energy of 10 eV and to flow to the anode at a rate given by the discharge current (4 A maximum). Ions on the other hand are assumed to go primarily into the beam, the grid webbing and the grid support flange.

A consideration of the thermal conduction characteristics of the various component parts of the discharge chamber along with the heat loads on these parts suggests that the screen grid, anode and cathode surfaces can be expected to perturb the mean wall temperature away from the values measured on the steel shell. The worst case temperature profiles over each of the surfaces have therefore been determined and the impact of these temperatures on the mean wall surface temperature has been evaluated. The screen grid has the greatest affect because 1) it has a low thermal conductivity as a result of its thin, perforated configuration, 2) it has a substantial area and 3) it has a high distributed heat load as a result of direct ion impact over its surface.

In modelling the grids thermally it was assumed that the extracted beam current was at its maximum value of 0.9 A. Since the extracted ion fraction for this ion source was typically 60% of the total ion production this means 0.6 A of ion current goes to interior surfaces of the discharge chamber.

Assuming a screen grid transparency to ions of 80% gives an ion current of 0.22 A to the screen grid webbing and the remainder 0.38 A to other surfaces accepting ions. It was also assumed that the ion current density to the screen grid webbing was the same as that through the screen grid holes and that ions striking the webbing had been accelerated from a worst case plasma potential ($\sim$ 50 v) to screen grid bias potential (- 30 v). This heat load combined with the radiated one induced a worst case temperature at the screen grid centerline that was $\sim$ 125°K above the temperature at the inner edge of the magnet support flange (Fig. 19). It was next assumed that all ions produced in the discharge chamber that did not go into the beam or onto the screen grid webbing (0.38 A) were directed uniformly onto the magnet support flange at an energy of 80 eV. Because this plate was made of copper and was thicker than the screen grid, the worst case temperature difference computed between its inside edge (6 cm radius) and its outer one (7.5 cm radius) was only $\sim$ 7°K.

The difference in temperature between the anode surface and the steel shell was computed by considering the heat flux to the interior surface of the anode resulting from both the electron current and radiated power from the cathode and plasma. It was assumed that the relatively soft mica was pressed sufficiently firmly between the magnets and the anode itself so contact thermal resistances were small and the major resistance to heat transfer occurred in the mica. Under these conditions the temperature difference between the anode and the steel shell was approximately 1°K. The cathode wire temperatures were assumed to be the value required to assure thermionic emission ($\sim$ 1475°K).

When the area weighted mean temperature of the surfaces exposed to the plasma was computed from the worst case component temperatures just cited it was found to be only $\sim$ 7°K above the mean steel shell temperature. Hence

under worst case thermal loading conditions the mean wall temperature would be expected to be 7°K above the mean steel shell temperature. During the actual conduct of the test the two thermocouples shown in Fig. 19 agreed to within about 5°K and they were found to exhibit worst case drifts of $\sim$ 10°K during the conduct of a test in the temperature range 80 to 160°K and $\sim$ 5°K during the conduct of the higher temperature tests. Based on these measurements and calculations it is suggested that mean wall temperatures agree with measured ones to within $\pm$ 10°K for low temperature tests and $\pm$ 5°K for higher temperature ones.

Collisional Effects

The neutral atom temperature could conceivably differ from the mean wall temperature because of collisions with electrons and ions which have energies that differ substantially from those associated with the unperturbed atom temperature. Electrons, because of their mass mismatch with the atoms, would not however be expected to perturb the atomic temperature significantly even though their temperature is typically quite high ($\sim$ 10 eV = 110,000°K). Ions on the other hand could affect the atom temperature because they have a larger elastic, energy transfer cross-section, because they can undergo charge exchange reactions with atoms and because they can be accelerated to substantial energies by electric fields in the plasma. For typical discharge chamber configurations the ion energies can generally reach the electron temperature ($\tilde{<}$ 10 eV) as determined by the Bohm criterion[22] but will probably not exceed it. Typical elastic collision cross sections between argon or krypton ions and atoms lie below 10 $\mathring{A}^2$ at the low ($\tilde{<}$ 10 eV) energies involved.[23] For a typical ion density of 10^{11} cm^{-3} this corresponds to a mean free path greater than 100 m which is 700 times the discharge chamber dimensions. Hence collisions with walls should dominate and elastic collision effects should be negligible.

For the charge exchange process[24,25] the argon and krypton cross sections are higher (of the order of 50 $\mathring{A}^2$) but this still implies mean free paths that are of the order of 100 times the discharge chamber dimensions so this collisional event would still be unlikely compared to wall collisions.

Finally it is noted that ions that go to discharge chamber walls rather than being extracted into the beam are accelerated into the walls through a plasma-to-wall potential difference which is of the order of several tens of volts. These ions while they could recombine and come into thermal equilibrium with the wall before they leave it might also be expected to recombine and recoil from it with some fraction of their incident energy. While it was hoped that the error due to recombined ions recoiling from the walls with energies above those expected for particles in thermal equilibrium with the walls would be small, no conclusive evidence was found in the literature to substantiate a supposition that this would or would not be the case.

Results

When the ion source was operated on argon at a wall temperature of 390°K and a discharge voltage of 50 v the plasma ion energy cost and neutral density parameter data pairs indicated by the data symbols of Fig. 20 were obtained. Through trial and error selection of the parameters ε_p^* and C_o, Eq. 40 was fit to these data. The fit, shown by the solid line of Fig. 20, was obtained for $C_o = 3.0$ A eq^{-1} and $\varepsilon_p^* = 56$ eV. The parameter ε_p^* is determined to first order by the propellant and the energy of the primary electrons (i.e. the discharge voltage) so one would not expect it to be affected by changes in wall temperature. Changes in wall temperature should however cause the parameter C_o to change in accordance with Eq. 41, and this equation could be applied directly if values for all of the quantities appearing in it were known. While most

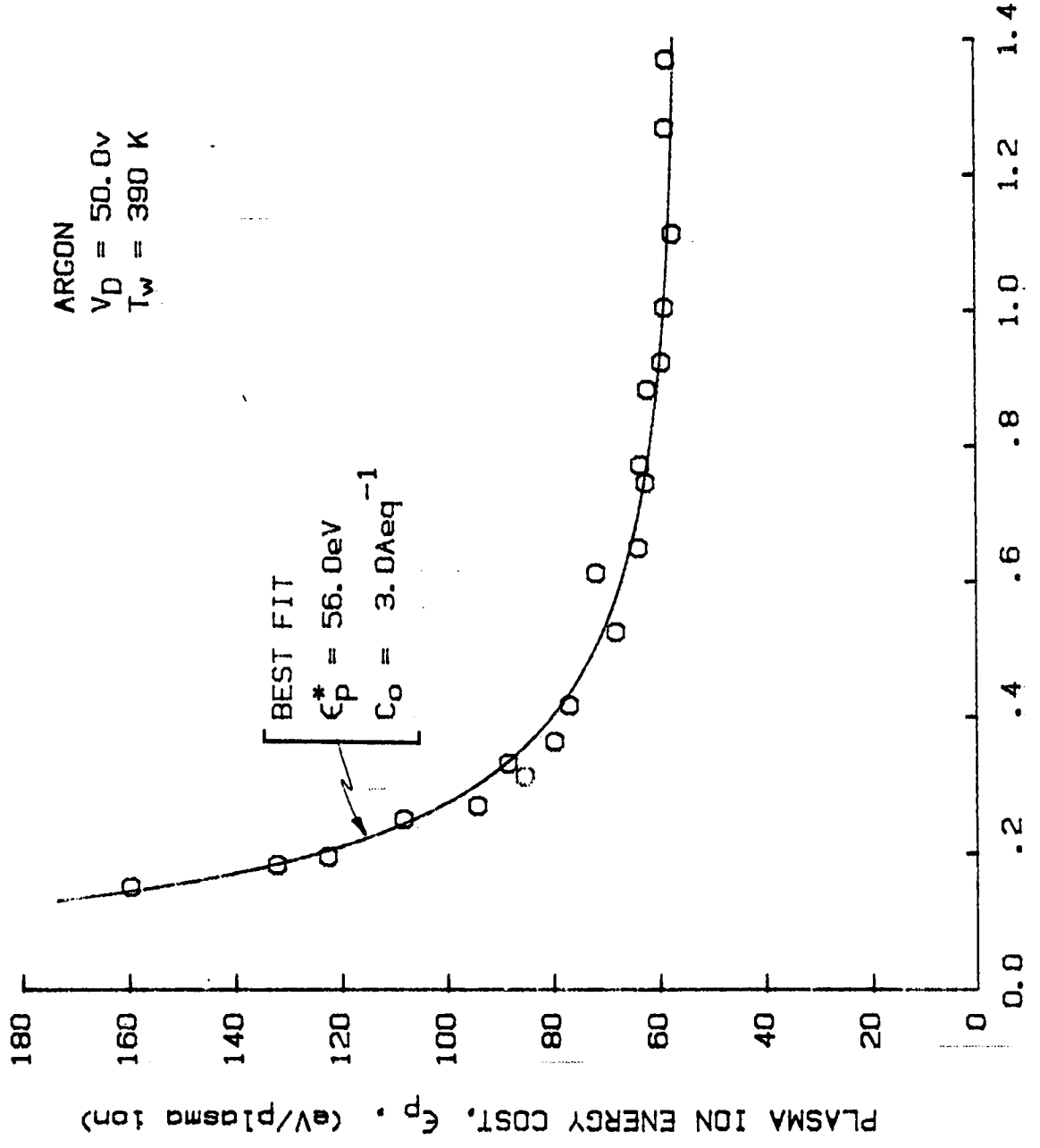

Fig. 20. Plasma Ion Performance Correlation for Argon at 390°K

of the values are known, we unfortunately do not have a model for the primary electron containment length ℓ_e. One can still see if the model describes the physical situation adequately however by determining the value of C_o appropriate to one wall temperature, then changing the wall temperature while holding all else constant and determining if the prediced change in C_o is consistent with Eq. 41. This has been done here by taking the value of C_o obtained by curve fitting the data of Fig. 20 ($C_{o\ ref}$) and computing new values of C_o appropriate to any new wall temperature from the following equation which has been obtained from Eq. 41.

$$C_o = C_{o\ ref}\sqrt{\frac{390}{T_W}} \tag{43}$$

Doing this one predicts the parameter C_o should be 3.7 A eq.$^{-1}$ for the case where the mean wall temperature is 255°K. Using this value the solid line shown on Fig. 21 is predicted. When the ion source was operated at this wall temperature the data points shown on Fig. 21 were measured. The agreement between these measured data points and the predicted curve is observed to be excellant. Applying Eq. 43 for a mean wall temperature of 90°K one obtains C_o = 6.2 A eq^{-1}. This corresponds to the solid curve shown in Fig. 22. When plasma ion energy cost/neutral density parameter data pairs were measured with the ion source operating at 90°K the results shown by the data points on Fig. 22 were obtained. Again the agreement between theory (solid line) and experiment (data points) appears to be good.

The ion source was also operated on krypton propellant at a mean wall temperature of 390°K. In order to predict the performance with this new propellant the constant C_o was computed from the expression

$$C_o = C_{o\ ref}\ \frac{\sigma_{o_{Kr}}}{\sigma_{o_{Ar}}}\sqrt{\frac{m_{Kr}}{m_{Ar}}} \tag{44}$$

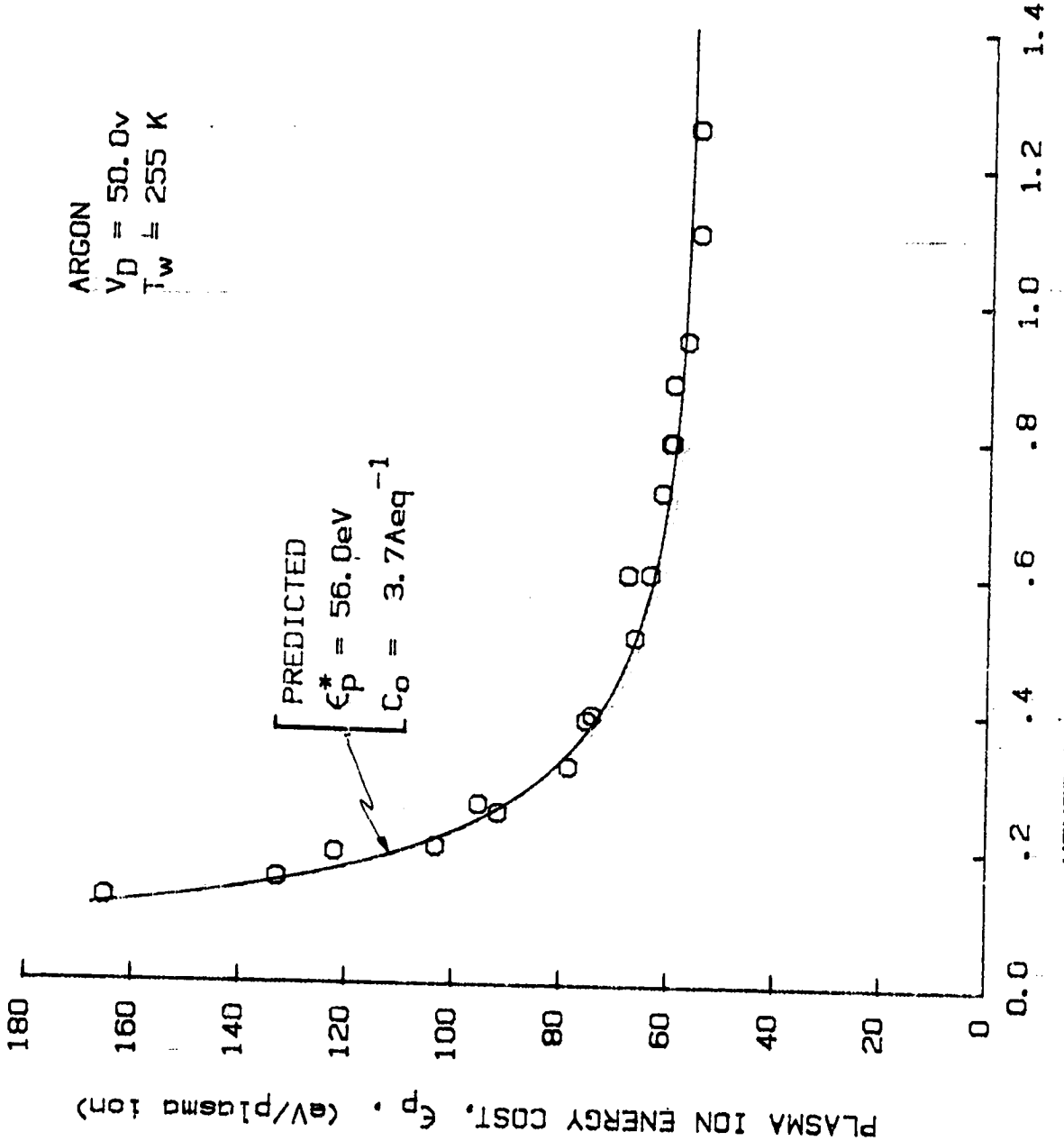

Fig. 21. Plasma Ion Performance Correlation for Argon at 255°K

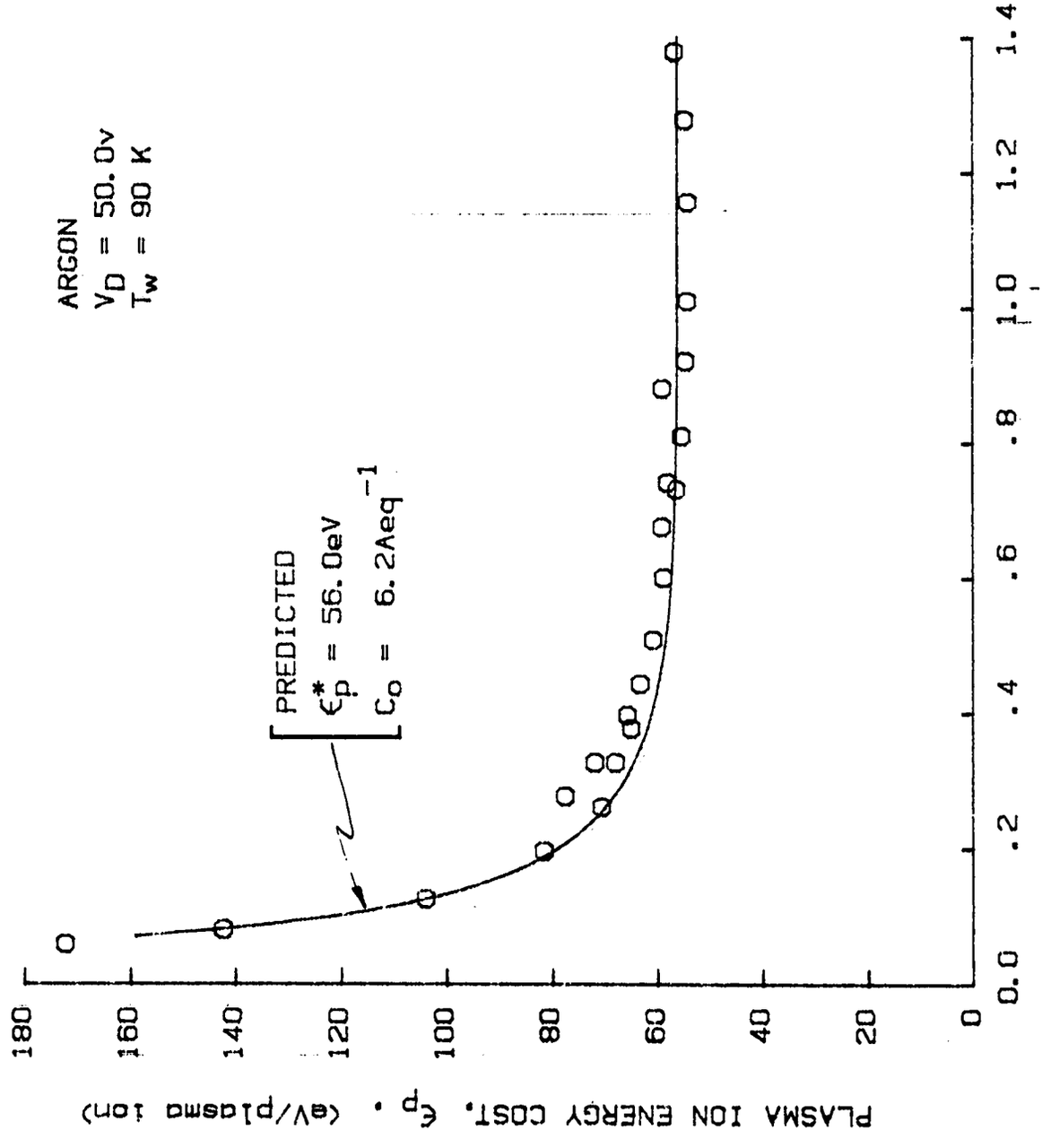

Fig. 22. Plasma Ion Performance Correlation for Argon at 90°K

where the subscripts Kr and Ar pertain to argon and krypton respectively. Using the appropriate atomic masses and total inelastic collision cross sections for argon at 50 v and krypton at 40 v as obtained from deHeer[14] in Eq. 44 one finds C_o = 5.5 A eq^{-1} should be appropriate. The baseline energy cost per plasma ion ε_p^* would also be expected to change with the propellant and discharge voltage. Its value was selected in the present case for krypton from experimental data as the plasma ion energy cost at a high neutral density parameter i.e. high flow rate/low beam current operating condition and was found to be 48 eV. Using C_o = 5.5 A eq^{-1} and ε_p^* = 48 eV in Eq. 40, the solid line shown in Fig. 23 was predicted for operation on krypton at 390°K. The discharge chamber performance data measured with krypton at 390°K are shown by the data symbols on Fig. 23. Once again the agreement between the predicted and measured performance is good. For a krypton fed discharge chamber cooled to 255°K and 155°K values of the parameter C_o equal to 6.8 and 8.7 A eq^{-1} respectively are predicted by Eqs. 42 and 43. Using these values as input to Eq. 40 the solid lines of Figs. 24 and 25 are predicted. Measured data for these temperatures are again shown by the data symbols in these two figures. As in all previous cases the measured data agree well with the predicted curves. It is noted that discharge chamber wall temperatures could not be reduced to $\sim$ 90°K when krypton propellant was being used because the propellant tended to condense.

The results shown in Figs. 21 through 25 all show sufficiently close agreement between predicted and measured performance results to suggest the effect of wall temperature is properly modelled in Eqs. 40 and 41. Changes in the constant C_o of $\pm$ 10% were generally sufficient to cause predicted curves in the figures to depart from the measured data to an easily noticeable degree. As a result it is suggested that the parameter C_o is accurate to within

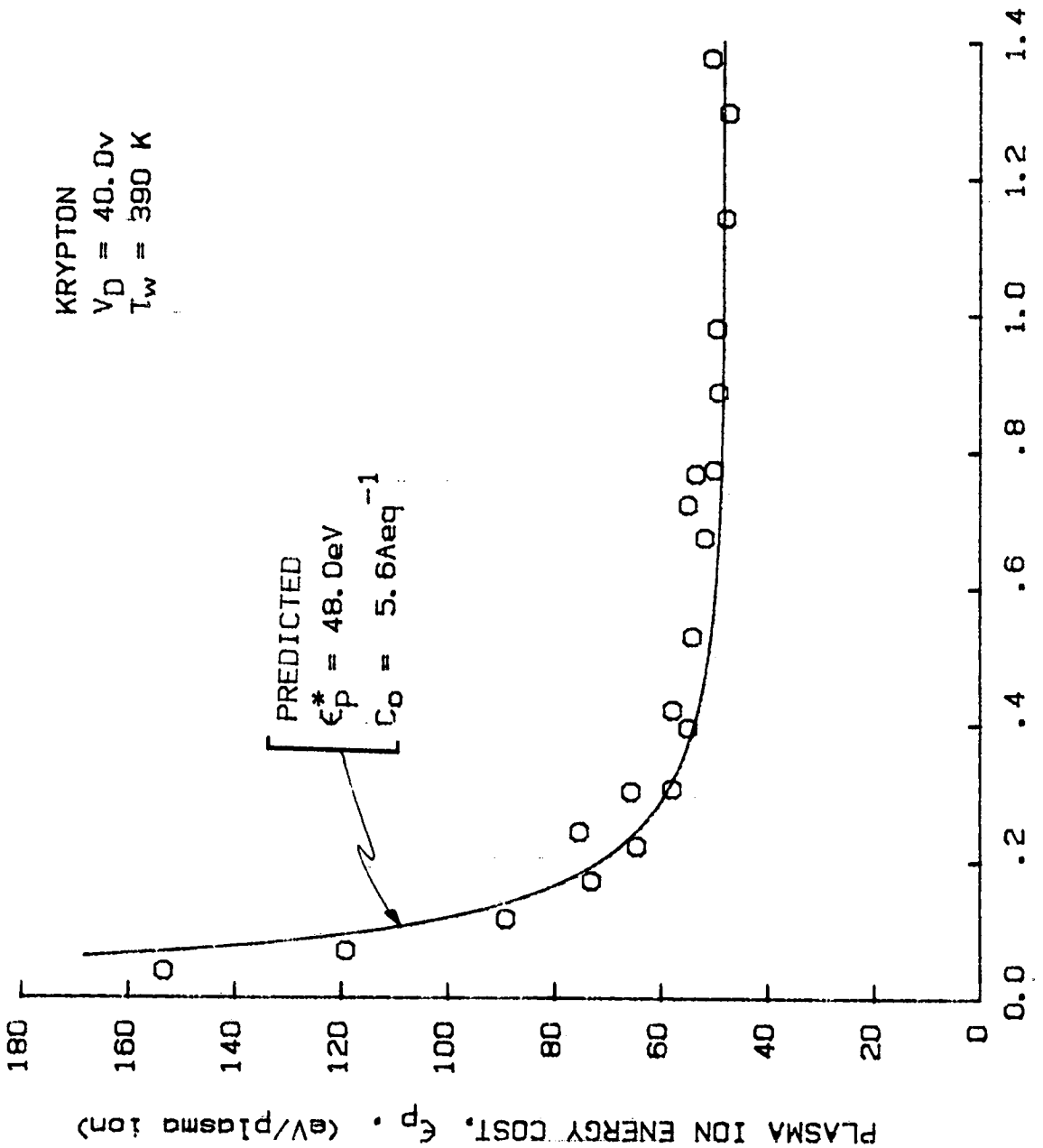

Fig. 23. Plasma Ion Performance Correlation for Krypton at 390°K

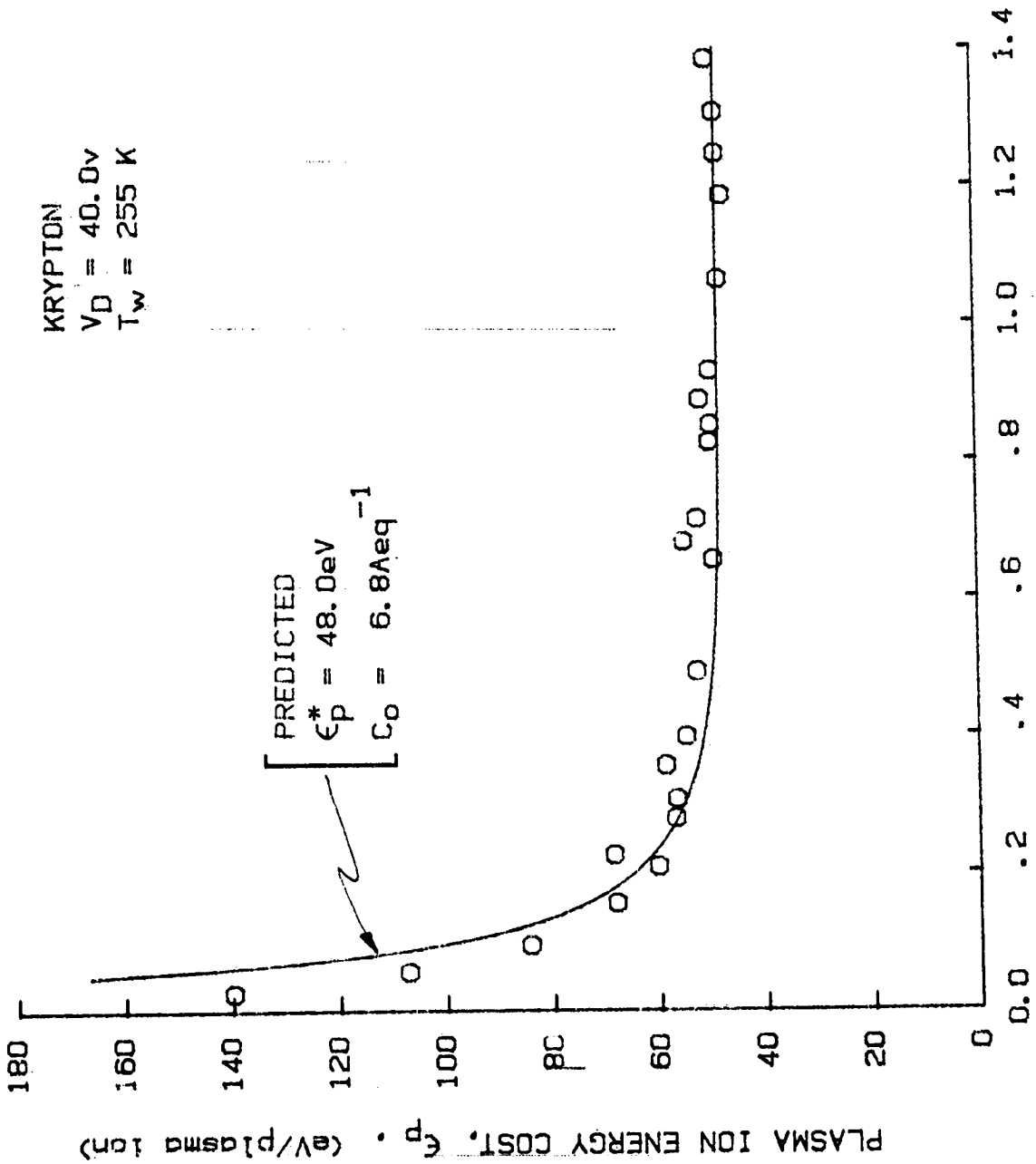

Fig. 24. Plasma Ion Performance Correlation for Krypton at 255°K

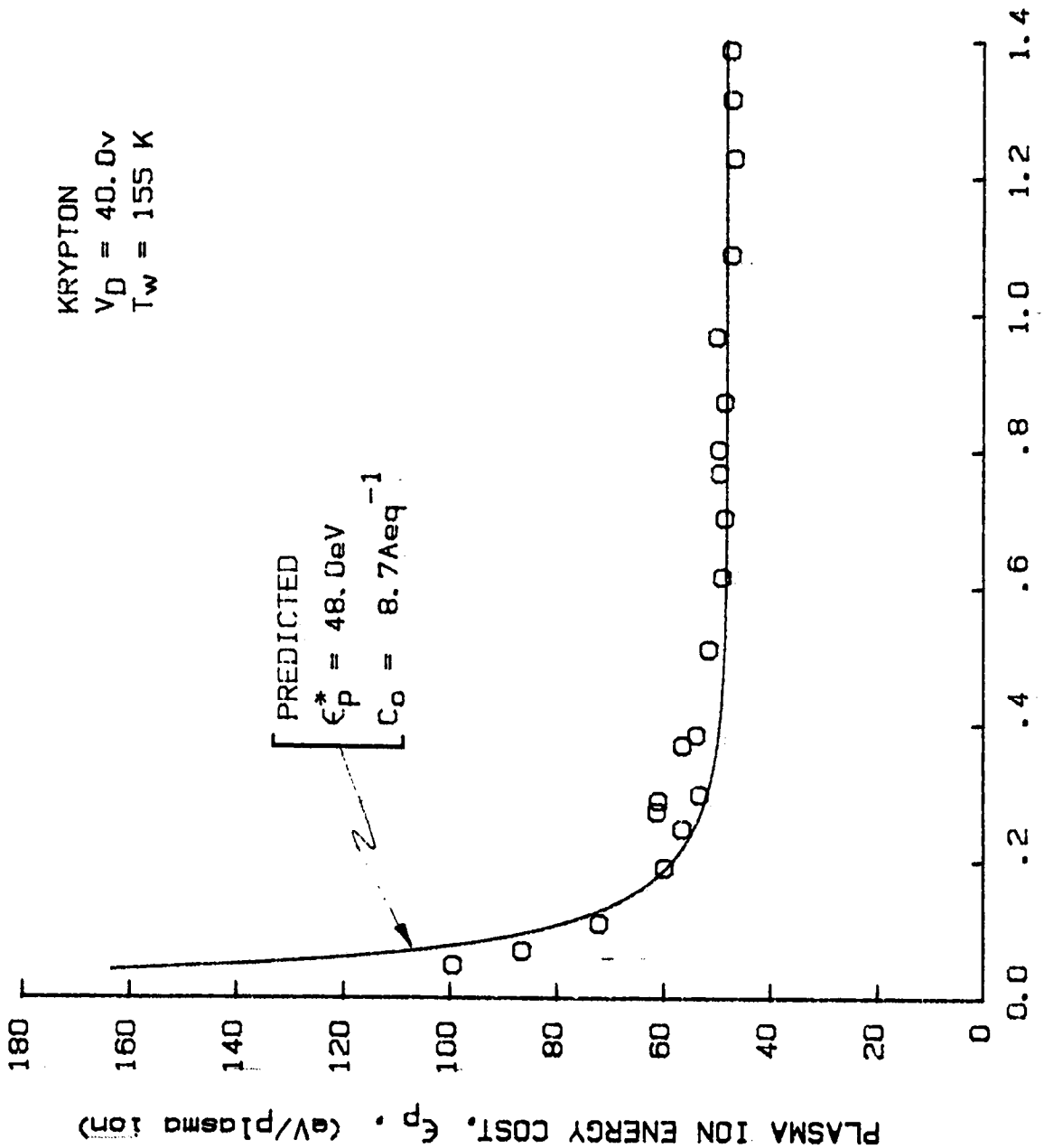

Fig. 25. Plasma Ion Performance Correlation for Krypton at 155°K

about ± 10% and the wall temperature effect is modeled accurately by Eq. 41 to within ± 20%.

The fraction of the ions produced in the discharge chamber that were extracted into the ion beam was also measured at each operating condition for these tests. These extracted ion fractions were relatively constant over the full range of neutral density parameters investigated taking on values essentially the same as those shown in Figs. 12 and 13. The extracted ion fractions were independent of discharge chamber wall temperature.

The results presented thus far, while they suggest the validity of the model proposed, do not show the extent to which the more traditional performance curves of energy cost per beam ion vs. propellant utilization are altered by changes in discharge chamber wall temperature. A typical example of the magnitude of the influence of wall cooling is shown in Fig. 26 and it is seen to be substantial. A point which should be made about the results of Fig. 26 is that the beam ion energy costs could be lowered substantially below those observed in the figure by using small hole accelerator grid optics and by increasing the propellant flow rate above the value used to obtain the data shown. Finally, it is also noted that the change in the traditional performance curves predicted by the complete theoretical model described in the previous section of this report is essentially identical to that shown by the experimental data in Fig. 26. This occurs because the high degree of agreement realized in the data of Fig. 20 through 25.

Conclusions

Substantial improvements in discharge chamber performance are induced by reductions in the mean discharge wall temperature. The extent of these improvements are predicted by the simple discharge chamber model described

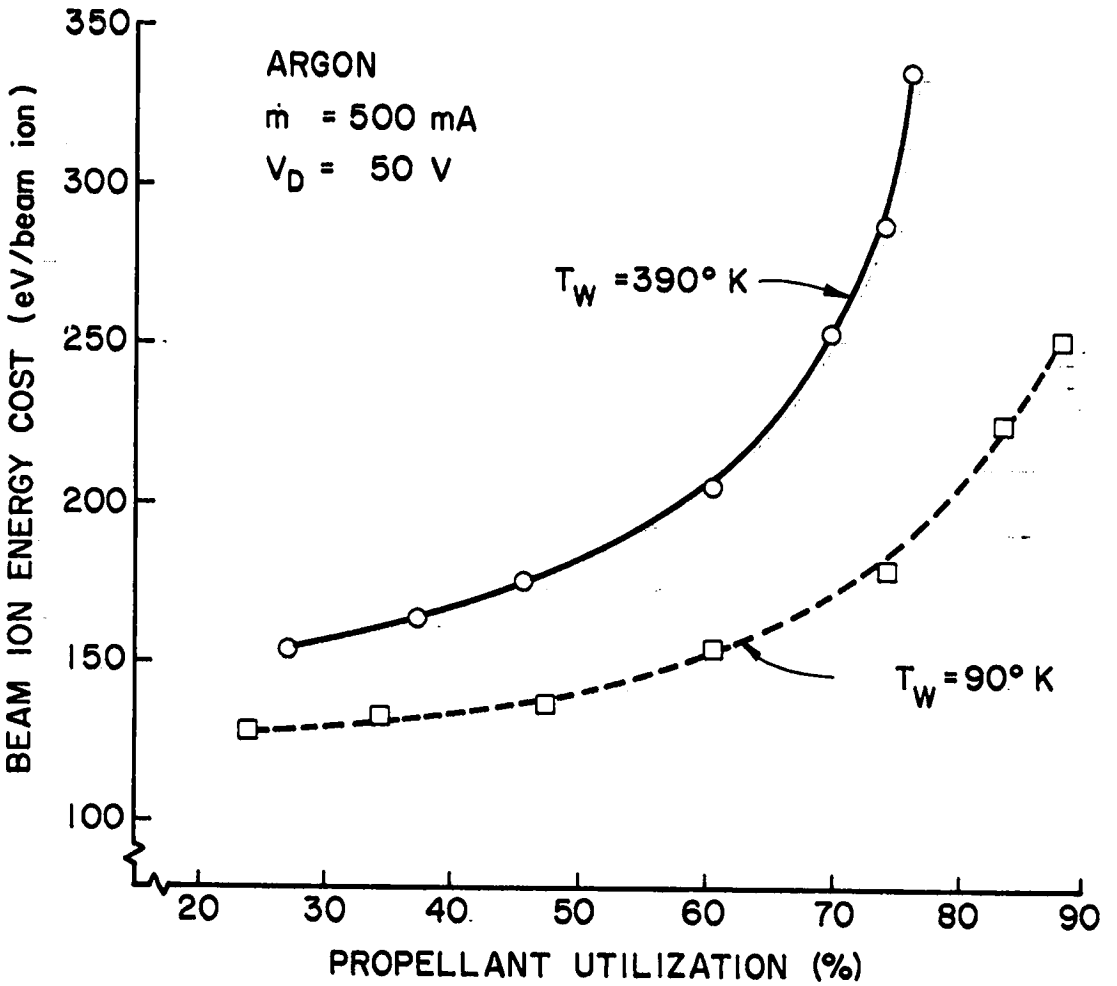

Fig. 26. Effect of Discharge Chamber Wall Temperature on Traditional Performance Curve

by Eqs. 40 and 41. Based on the high degree of agreement between the predictions of this model and experimental results it is concluded that the assumptions of the model are valid. These assumptions are 1) that the atoms present in a typical ion thruster discharge chamber move at a mean thermal velocity determined to first order by the mean discharge chamber wall temperature and 2) that this mean velocity is not perturbed significantly by collisional or recombined-ion recoil effects.

LOW MAGNETIC FIELD STRENGTH DISCHARGE CHAMBERS

J. R. Brophy

The discharge chamber model discussed in the preceding sections of this report was developed for cusp-type discharge chambers where electrons are lost predominantly into the cusps along magnetic lines-of-force. For discharge chamber configurations in which electrons must diffuse across magnetic field lines the field strengths can be considerably less than those found in the cusp-type chambers. Indeed, they must be considerably weaker in the diffusion-type discharge chamber in order to effect proper operation. In spite of these differences many of the operational features of the two discharge chamber types are similar. In both cases primary electrons are injected into the discharge chamber plasma, ions are created by electron bombardment, a fraction of the ions produced are extracted into the beam, and Maxwellian electrons are collected by the anode. In the preceding sections of this report it has been demonstrated that the performance of a cusp-type thruster is strongly dependent on the loss of primary electrons through the cusps to the anode. The similarity in the shape of the performance curves for both the cusp-type and diffusion-type discharge chambers suggests that the loss of high energy or primary electrons is also occurring in the low field strength diffusion-type configurations. It can also be argued that this is reasonable from an energy conservation standpoint. Consider the situation at high propellant utilizations where increasing the cathode emission current produces little additional beam current. This suggests that few additional ions are created. Yet, the energy contained in these additional primary electrons must go somewhere. This energy may go into excitation collisions with ions, increasing the Maxwellian electron temperature or it may be carried directly to the anode by the primary electrons.

It is this third possibility that seems the most likely based on the results of this report. In fact, calculations by Longhurst[26] support this conclusion. For this hypothesis to be viable, however, a model describing primary electron transport across magnetic field lines without energy degradation must be identified and verified experimentally.

EFFECT OF SCREEN GRID POTENTIAL ON PERVEANCE

J. R. Brophy

Introduction

It has been observed[27] that the impingement-limited perveance of a two-grid accelerator system is a function of the ratio of discharge-to-total voltage (V_D/V_T), provided the screen grid is at cathode potential and the plasma is near anode potential. These observations indicate that the perveance decreases as the ratio V_D/V_T is increased. It is believed that this effect is predominately the result of the potential difference between the plasma and the screen grid (ΔV), which in the above case is approximately equal to V_D. Other effects, such as a change in Maxwellian electron temperature or primary electron energy, resulting from a change in discharge voltage are not believed to be important.

To investigate the effect of $\Delta V/V_T$ on perveance experimentally a 15 cm dia. ring cusp ion thruster was configured with the screen grid electrically isolated from the thruster body. This allowed the screen grid to be biased negative of cathode potential while the discharge voltage (V_D) and total voltage (V_T) were held constant. In this case the potential difference between the screen grid and the plasma is given approximately by,

$$\Delta V = V_D + |V_S| \quad , \tag{45}$$

where both voltages are measured relative to cathode potential and $|V_S|$ is the magnitude of the negative bias applied to the screen grid. Earlier attempts to measure the effect of the screen grid-plasma potential difference on perveance by varying the discharge voltage while holding the total voltage constant have been limited by the range over which the discharge voltage could be varied. By biasing the screen grid in the manner described above,

the impingement-limited perveance can be measured over a large range of $\Delta V/V_T$ while the discharge voltage, total voltage and net-to-total voltage ratio are held constant.

Apparatus and Procedure

These experiments were conducted on a 15 cm dia. ring cusp ion thruster equipped with a set of dished, small hole accelerator grid (SHAG) optics. The physical open area fractions of the screen grid and accelerator grid were 0.68 and 0.30, respectively, and the cold grid spacing was .75 mm.

The following procedure was implemented for the collection of data in this investigation. The flow rate of the argon propellant used was set and maintained at 1000 mAeq, and the discharge voltage was held constant at 50 v. Total voltages of 500, 1000 and 1500v were investigated at a net-to-total voltage ratio of 0.6. At each value of the negative bias applied to the screen grid, the discharge current was adjusted until the impingement-limited perveance condition was realized. This condition was said to exist when the impingement current started to rise dramatically. The use of non-regulated high voltage power supplies necessitated the use of this somewhat imprecise definition of the impingement limit. With these power supplies an increase in impingement current causes increased power supply loading which then causes the accelerator grid potential to become less negative. This in turn induced a further increase in impingement current and these effects cascade. The perveance level at which this process begins is designated at the impingement limited perveance.

Results and Discussion

The results of these tests are shown in Fig. 27. The parameter $J_B/V_T^{3/2}$, where J_B is the beam current at the impingement limit, is proportional to

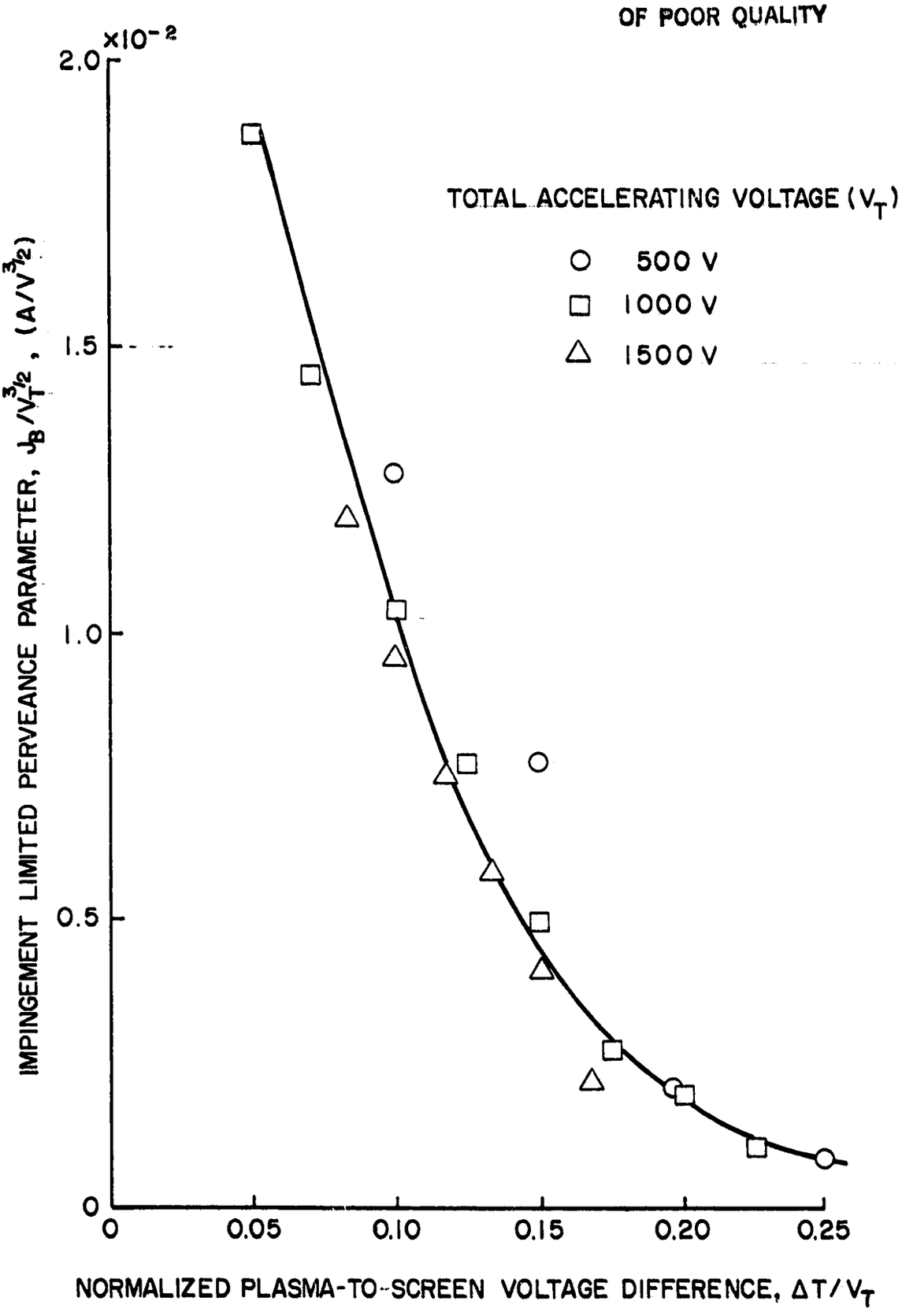

Fig. 27. Effect of Plasma-to-Screen Grid Potential Difference on Impingement Limited Perveance

the impingement-limited perveance. Clearly this parameter is a decreasing function of $\Delta V/V_T$, and is approximately independent of the total voltage. These results, obtained with a 15 cm dia. ion source, are consistant with those found by Rovang[1] on a much smaller test facility. The experiments of Ref. 1 were performed on an 8 cm dia. source masked to produce an ion beam approximately 1 cm in diameter centered on the thruster axis. This insured ion extraction from a plasma of near uniform density across the active grid area. In the present case, however, the plasma density is almost certainly non-uniform across the grid area. Thus it is considered significant that the results of the present test agree with those obtained by Rovang.[1]

Since the results of Fig. 27 indicate that the impingement-limited perveance decreases as the ratio $\Delta V/V_T$ is increased, it is desirable that $\Delta V/V_T$ be made as small as possible. It should be noted, however, that if ΔV is made smaller by biasing the screen grid more positive than the floating potential of the plasma a discharge chamber performance penality in the form of higher plasma and beam ion energy costs will be incurred. These higher ion energy costs will result from the increased removal of energetic electrons from the plasma to the screen grid.

For missions characterized by low values of specific impulse (low net accelerating voltages), the requirement for low $\Delta V/V_T$ might be expected to impact the selection of the desired net-to-total accelerating voltage ratio (R). Greater flexibility in the selection of this ratio would be afforded if $\Delta V/V_T$ could be reduced by decreasing ΔV. For direct current discharge chambers a reasonable limit on ΔV would be expected to be the discharge voltage/floating potential difference for the reasons mentioned above. For RF discharge chambers, however, ΔV could presumably be made as small as a few volts.

XENON AND ARGON HOLLOW CATHODE RESEARCH

Dan Siegfried

Introduction

Recent research has provided a better understanding of the basic physical processes underlaying operation of orificed hollow cathodes[28] and has led to the development of an analytical model describing these processes. That work was done for cathodes operating on mercury, the propellant currently used in flight-certified ion thrusters. The development of advanced ion thrusters which operate on xenon and argon has resulted in the need for main and neutralizer hollow cathodes which operate efficiently and and reliably on these gases. At present, hollow cathodes operating on these gases under neutralizer conditions have relatively high electrical power and propellant flow rate requirements. In order to develop a more efficient hollow cathode for this application, it would be useful to understand how the use of argon and xenon affect the operation of the cathode.

The objective of the research described here is to determine what effect operation with these propellants has on the basic physical processes previously identified for mercury, orificed hollow cathodes and to determine if the analytical model developed for mercury cathodes can also be used with argon and xenon. In order to do this, experiments similar to those conducted with mercury were performed using a special quartz-body test cathode and mounting fixture. This apparatus allows the simultaneous measurement of cathode internal pressure, the insert temperature profile, internal plasma properties, and the emission currents from various cathode surfaces. The results of these experiments will be presented here and compared with calculated results based on the analytical model.

Apparatus and Procedure

The cathode test configuration used in the experiments is shown in Fig. 28. The cathode outer tube was made of quartz to allow direct visual observation of the insert for temperature measurement and to provide electrical isolation of the insert for current measurement. The cathode used a single layer tantalum foil insert dip-coated in the chemical R-500.* The insert was 15 to 20 mm long and had a diameter of 3.8 mm; the cathode was operated with orifice plates having 0.51 and 0.76 mm diameter orifices. A movable Langmuir probe mounted on the cathode axis was used to measure plasma properties within the cathode. A manometer having diffusion pump oil as a working fluid was used for sensing the upstream stagnation pressure in the cathode and the insert temperatures were measured with a micro-optical pyrometer.

The apparatus and procedures used in the experiment were essentially the same as those used in the earlier experiments with mercury. The reader is referred to the report on those earlier mercury experiments[28] for details of construction and procedure, since only the few notable differences will be pointed out here.

Because the recent experiments were run with a non-condensing gas, the heater on the manometer was not needed and was not used. In addition, gas flow rate adjustment was accomplished with a micro-adjustable needle valve in the propellant feed line rather than the vaporizer heater required for mercury. Adjustment of the flow rate was, therefore, much simpler than with mercury and the throttle valve shown in Fig. 28 was not necessary. This valve

---

* A double carbonate mixture - (Ba/Sr) CO_3 manufactured by the J.R. Baker Chemical Co., Phillipsburg, New Jersey.

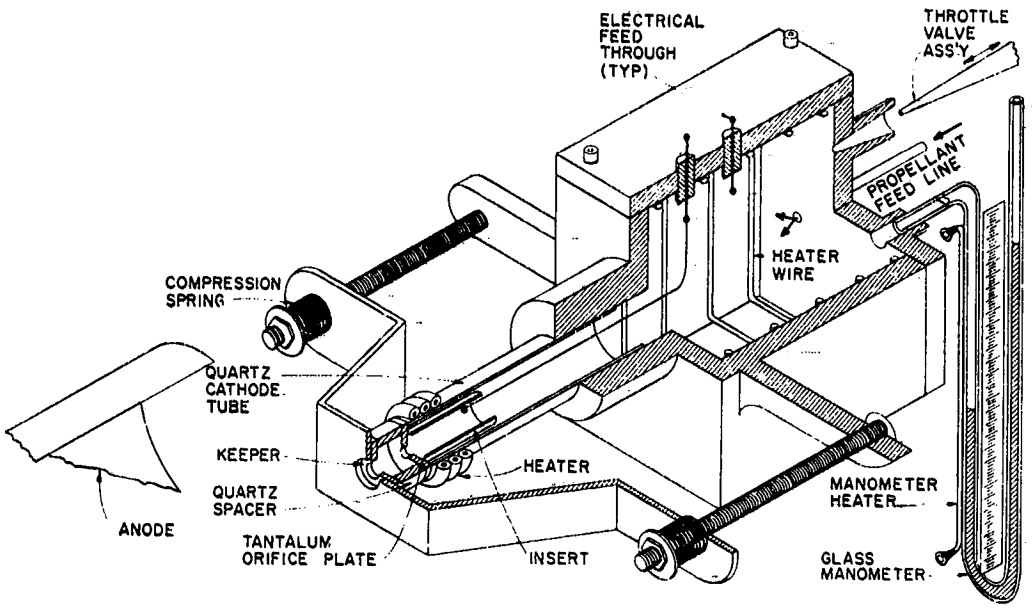

Fig. 28. Hollow Cathode Test Configuration

was left closed in the present tests.

In the earlier tests, the electrode used in the probe was a tungsten sphere with a diameter of ~ 0.76 mm formed on the end of a 0.25 mm diameter wire. Using that probe, perturbation of the internal discharge appeared to be somewhat greater with argon and xenon than that experienced with mercury. For this reason, probes having a smaller electrode surface area were used in the present experiment. Spherical probes ranging in diameter from 0.48 to 0.58 mm and a planar probe with a surface 0.25 mm in diameter were used.

Depletion/contamination of the insert was a significant problem in the argon and xenon experiments presented here. Obtaining and maintaining an insert surface having a relatively low, uniform and stable work function proved to be extremely difficult. This was somewhat of a problem, though much less severe, when the experiments were performed with mercury. In the experiments with all of the gases including mercury, the materials and construction, were the same; and a great deal of care was taken in fabricating and conditioning the insert. However, because of the severity of the problem in the present case, two additional precautions were taken which were not used in the mercury experiments. One was the installation of a liquid nitrogen cold finger in the bell jar near the cathode. The purpose of this was to help remove residual water vapor and other condensable contaminants present in the bell jar. The cold finger was operated during insert conditioning and during cathode operation. In addition, greater care was taken in constructing and outgassing the Langmuir probe used in the tests. Although both of these procedures seemed to improve the problem of insert degradation to a small degree, it now appears that the degradation may be directly related to the use of xenon and argon as propellants. This will be discussed in more detail with the presentation of the results.

The problems with insert degradation mentioned above affected the method in which data was taken during the experiments. The insert work function has a significant effect on such cathode operating parameters as insert temperature and plasma properties. Since insert work function tended to change during the course of an experiment, an attempt was made to take data as quickly as possible to minimize the effect of this work function variation. In addition, complete data sets (plasma property profiles, insert temperature profiles, and current distributions) for each operating condition were not always recorded simultaneously. The reason for this was related to the fact that the effect of a parameter such as flow rate on, say, insert temperature could be masked easily by changes in insert condition during the time required to record a complete data set. Because of this, there were a number of instances in which a single measurement such as plasma density or insert temperature were made as a particular operating parameter such as flow rate was rapidly varied. Such a procedure has an obvious advantage in showing the effect of one parameter on another, but does not solve the problem of obtaining complete and consistent sets of data over a range of operating conditions in the presence of changes in work function. There was little that could be done about the latter problem. The considerable scatter found in some of the results is believed to be due in a large part to this difficulty.

The Phenomenological Model

The earlier work done with mercury resulted in the development of phenomenological model describing the important physical processes underlying the operation of the cathode. One of the purposes of the present work is to determine whether that model applies to cathodes operating on argon and xenon. It will be useful, therefore, to begin by stating the

key aspects of the model developed for mercury. This will then be used as a background for dicussing the results obtained with xenon and argon.

The experiments with mercury showed that the electrons which exit through the cathode orifice are produced within the cathode both by surface emission ($\sim$ 70%) and by volume ionization processes ($\sim$ 30%). The surface emission is due primarily to field-enhanced thermionic emission from a relatively well defined band on the downstream end of the insert; while volume ionization occurs primarily within the region circumscribed by the emitting portion of the insert. Acceleration of surface emitted electrons across the plasma sheath results in the formation of a nearly monoenergetic population of primary electrons. The primaries are essential for sustaining the volume ionization process. They represent the sole energy input into the "ion production region" and are estimated to be directly responsible for $\sim$ 65% of the ion/electron pairs produced in the plasma. The rest of the ionization is attributable to the high energy tail of the Maxwellian electron population. Since for mercury the cathode internal plasma potential is typically $\sim$ 9 v, the ionization is predominantly a multi-step process, relying heavily on the production of ions from intermediate metastable and resonance states. The ions produced in the "ion production region" diffuse out of it at the Bohm velocity and are accelerated across the plasma sheath striking the insert with sufficient energy to heat it to the emission temperature. These ions are neutralized at the insert surface and thus complete the current path between the cathode surface and the volume-produced electrons which exit through the cathode orifice.

The processes described above are discussed in detail in Ref. 28 where it is shown that they can be represented analytically in a rather simple form if two assumptions are made. First, the emitting length of the insert

and, therefore, the length of the ion production region is assumed to be on the order of the energy exchange mean free path for a primary electron. The rationale here is that the primary electrons are essential for the processes in the region and that as soon as they sustain a significant energy loss in a collision they are quickly thermalized and cease to exist as primary electrons. Having defined the length of the ion production region based on the primary electron energy exchange mean free path, it is next assumed that the plasma properties (plasma density, plasma potential, and electron temperature) and the insert surface temperature are uniform throughout this region. In addition to the two assumptions above, an experimentally determined value is assumed for the Maxwellian electron temperature. The reason for this is that there is a priori no simple means of predicting the electron temperature and the model is relatively insensitive to this parameter over its normal range of values.

Results

Results will be presented in four sections in the following order. First, typical results will be presented which show the qualitative effect of the propellant type and the insert surface work function on cathode parameters such insert temperature and plasma properties. These results will provide general information regarding the effect of propellant type on the basic physical processes occurring within the hollow cathode. In the next section, inelastic cross-section data will be presented for argon and xenon and will be used to shed light on the nature of the collisional processes taking place in the ion production region. In the third section, detailed results for argon and xenon will be presented which show the effect of discharge current and flow rate on plasma properties and insert temperature; and a comparison will be made with predictions of the analytical

model. The final section will present a correlation of pressure-flow rate data for argon and xenon. The results of that section can be used to predict the cathode internal pressure when applying the analytical model to situations where the pressure is unknown.

Propellant and Insert Surface Work Function Effects

The effects of propellant gas and insert surface work function on the internal plasma density profile are shown in Fig. 29 for similar cathodes operating at discharge currents of 2.3 A and an internal pressure of $\sim$ 4 Torr. The solid curves represent results obtained in quick succession with the same cathode by simply turning off the xenon supply and turning on the argon supply (the two gas supplies were connected in parallel). Since the probe and insert surface conditions are believed to be nearly the same in both cases, this provides a direct comparison of the effect on plasma density of varying the propellant from xenon to argon. The results show that the peak plasma density for xenon is nearly double that for argon and suggests that the ion production region is on the order of 5 mm long for xenon while for argon it is closer to 7 mm. A comparison can also be made between operation with mercury (dashed curve) and with xenon (center-dash curve) for similar cathode conditions where both cathodes are operating with inserts having surface work functions of $\sim$1.9 eV. The xenon cathode achieves a peak plasma density $\sim$ 50% higher than the mercury and the ion production region for the xenon appears to be about twice the 1 to 2 mm length found with mercury.

The effect of insert surface work function on plasma density can be seen by comparing the difference between the two curves for xenon in Fig. 29. The main consequence of a lower work function appears to be a reduction in the length of the emission/ion production region. The difference in peak

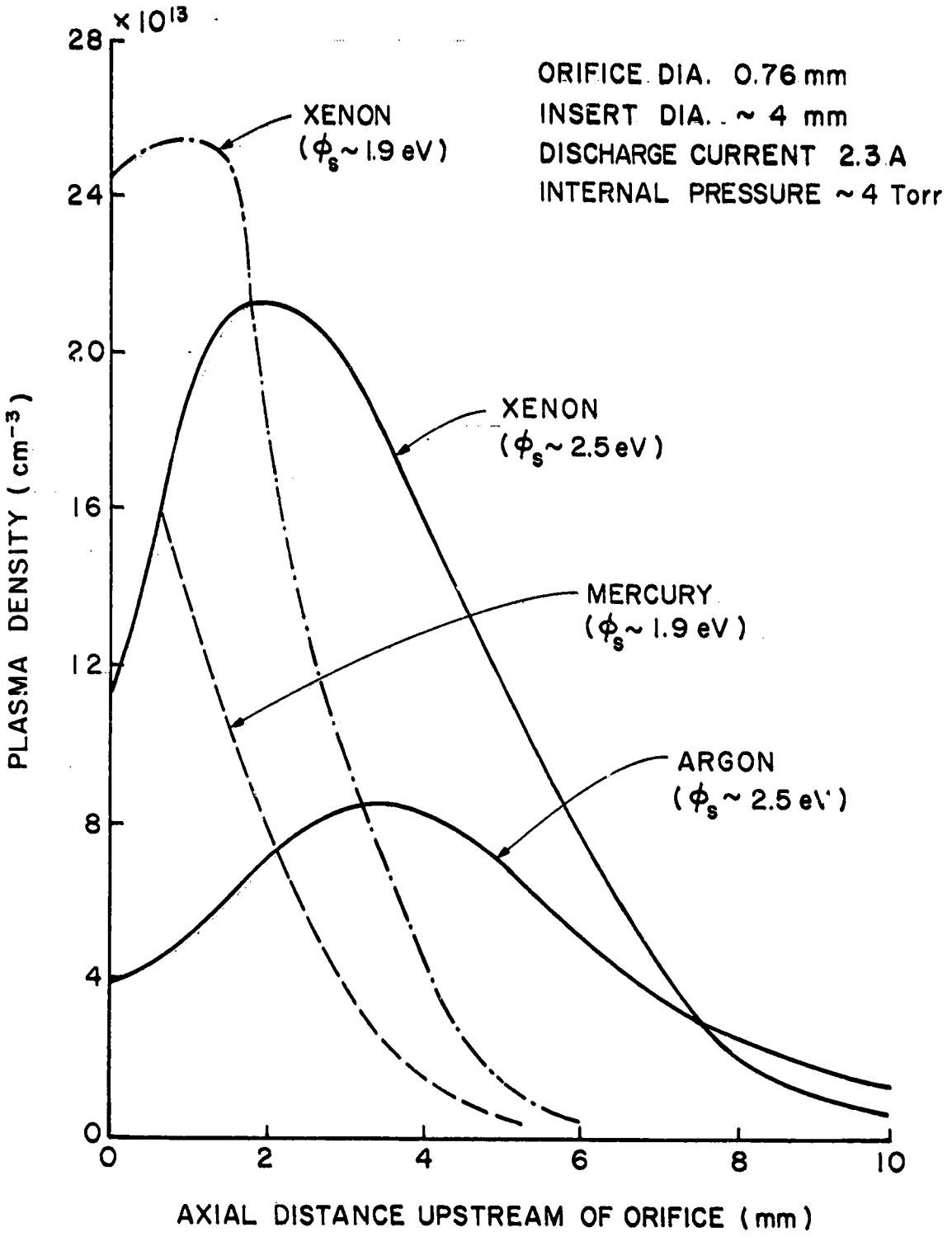

Fig. 29. Effect of Propellant and Insert Surface Work Function on Plasma Density Profile

plasma density between the two xenon curves in Fig. 29 is not believed to be significant. It is less than typical scatter found in the data and, in fact, other results have indicated that the peak plasma density may increase with increases in surface work function.

A similar comparison is presented in Fig. 30 for insert temperature profiles, again with propellant type and surface work function as parameters. The results of Fig. 30 suggest that the peak insert temperature is relatively independent of the propellant type for a given value of the insert surface work function. It is also worth pointing out in Fig. 30 that the insert temperature peaks correspond approximately with the plasma density peaks in Fig. 29 and that the emission lengths indicated by the temperature profiles are also consistent with the length of the ion production region indicated by the plasma density profiles in Fig. 29.

Figure 31 shows the effect of propellant type and insert work function on plasma potentials inside the cathode. The difference between the two xenon curves indicates that the plasma potential increased significantly with surface work function. The two solid curves shown in Fig. 31 are again the results obtained using the same cathode and simply switching from xenon to argon. A comparison of these two curves shows that under similar surface work function conditions ($\phi_s \sim 2.5$ eV) that the internal plasma potential with argon is ~ 3 volts greater than that with xenon. This is consistent with the ~ 3 volt difference both in first excitation and first ionization energies between the two gases. On the other hand, the xenon and mercury cathodes each operating under similar conditions with a similar surface work function ($\phi_s \sim 1.9$ eV), the internal plasma potentials are similar (Fig. 31, dashed and center-dashed curves) while on the basis of either first excitation or ionization potential xenon might be expected to exhibit

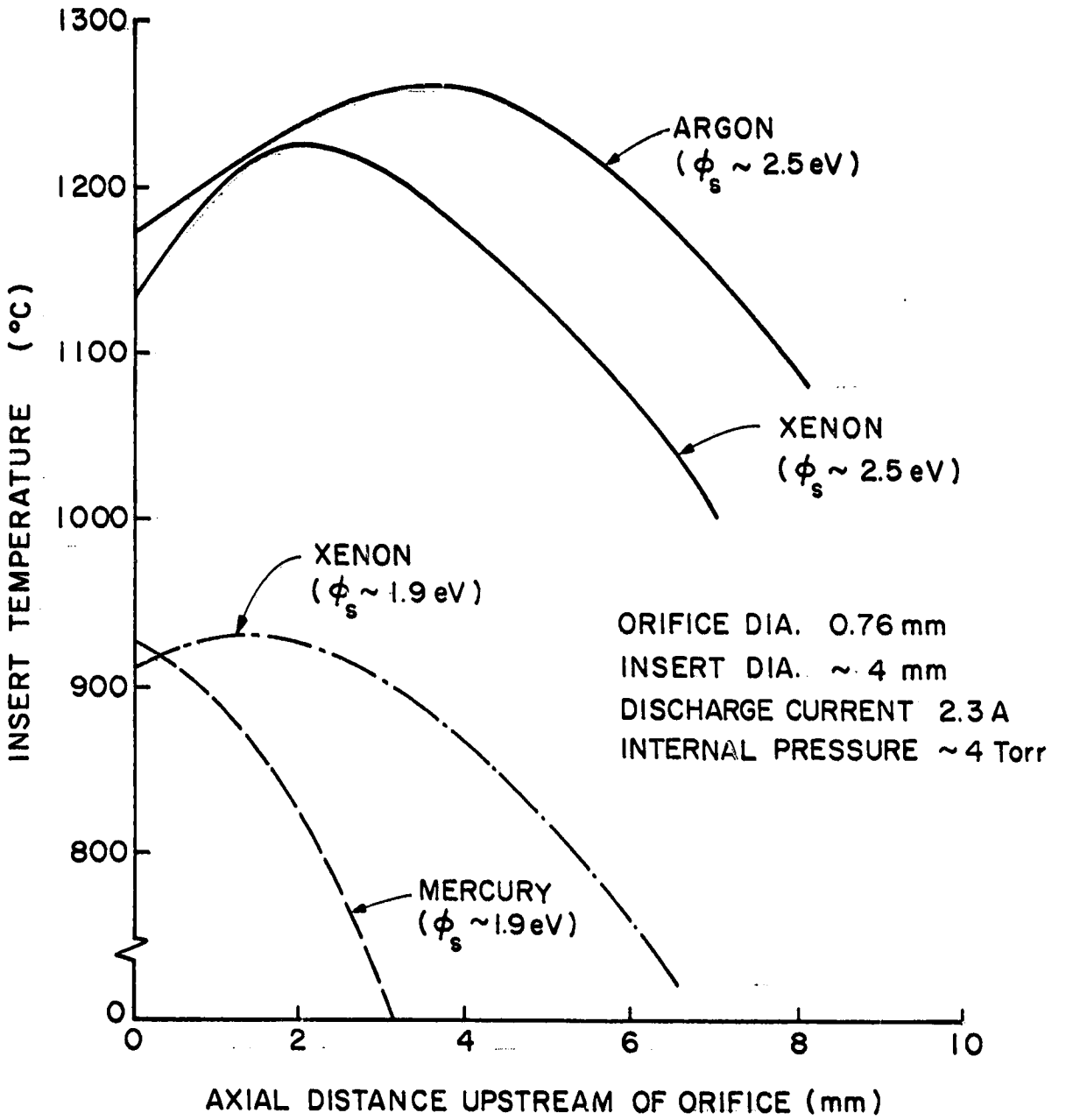

Fig. 30. Effect of Propellant and Insert Surface Work Function on Insert Temperature Profile

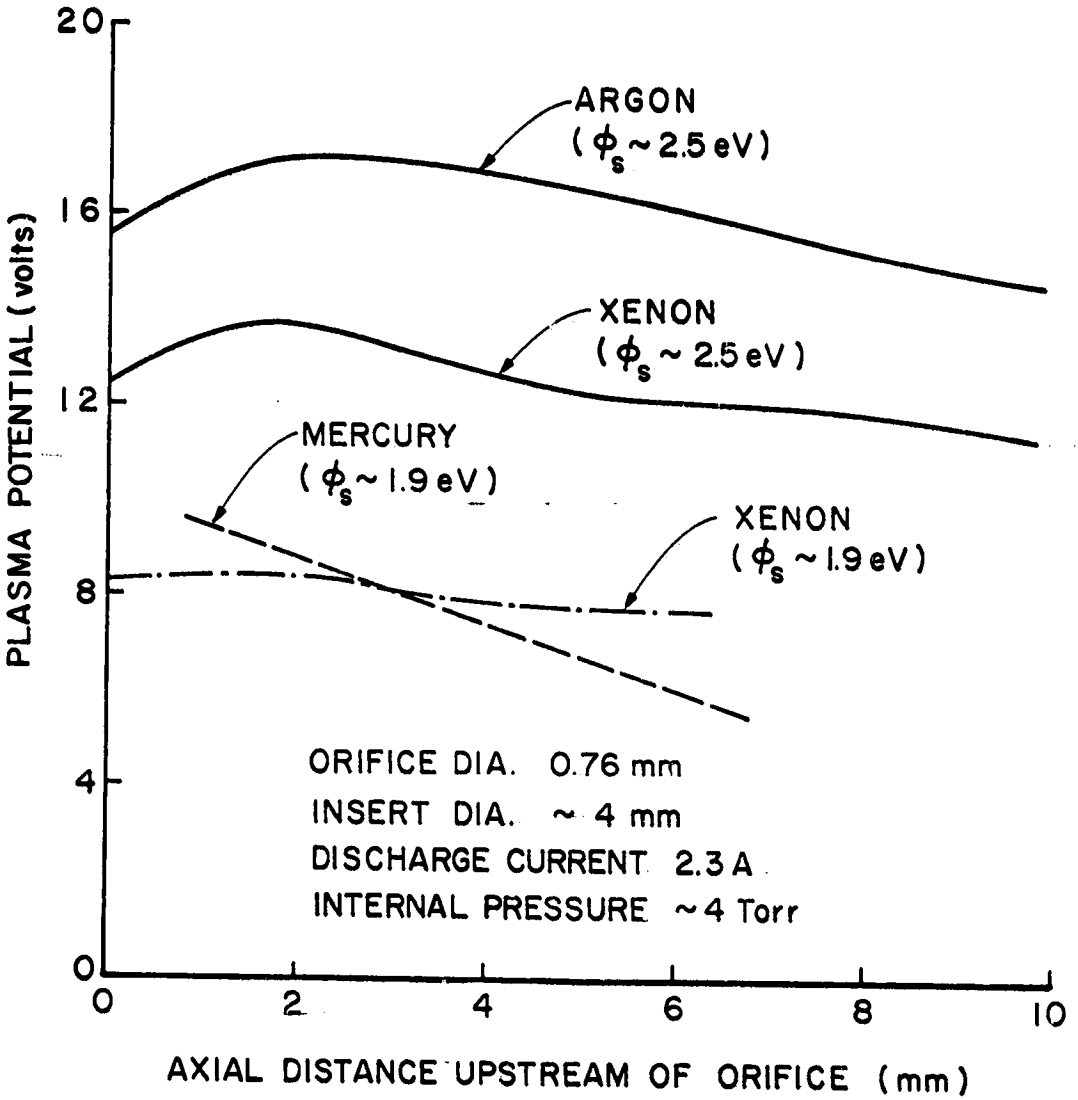

Fig. 31. Effect of Propellant and Insert Surface Work Function on Plasma Potential Profile

a higher plasma potential than mercury. It is unclear as to why this is not the case.

The effect of insert surface work function and propellant type on the electron temperature is shown in Fig. 32. In the upper plot of Fig. 32 the solid curves show the electron temperature of xenon plotted as a function of discharge current with surface work function as a parameter, while the lower plot shows similar results for xenon plotted as a function of internal pressure. The dashed curves in Fig. 32 are for a similar cathode operating on mercury and having an insert with a work function of $\sim$ 1.9 eV. No curve is shown for the argon data because of the few data points available. There are two significant points to be noted in Fig. 32: 1) the electron temperature for xenon and mercury are similar with average values near $\sim$ 0.8 eV, when the surface work function is $\sim$ 1.9 eV, while argon has a significantly higher electron temperature near 1.3 eV; and 2) the electron temperature increases as the insert surface work function increases (indicated by the xenon curves).

In addition, to the propellant effects noted in Figs. 29 to 32 there are some qualitative differences which were observed during the experiments and are worth noting here. One of these is the apparently greater sensitivity of the insert to depletion or contamination seen when operating the cathode on xenon and argon as compared to operation with mercury. The reason for this is not clear. One possibility is increased surface damage/depletion due to sputtering by ions returning to the surface from a plasma at a higher plasma potential, an explanation that appears particularly likely in the case of argon. Another possibility is increased sputtering due to higher ion current densities to the surface, particularly with xenon. The ion flux to the surface is directly proportional to the local plasma density and inversely proportional to the square root of the atomic mass. Xenon

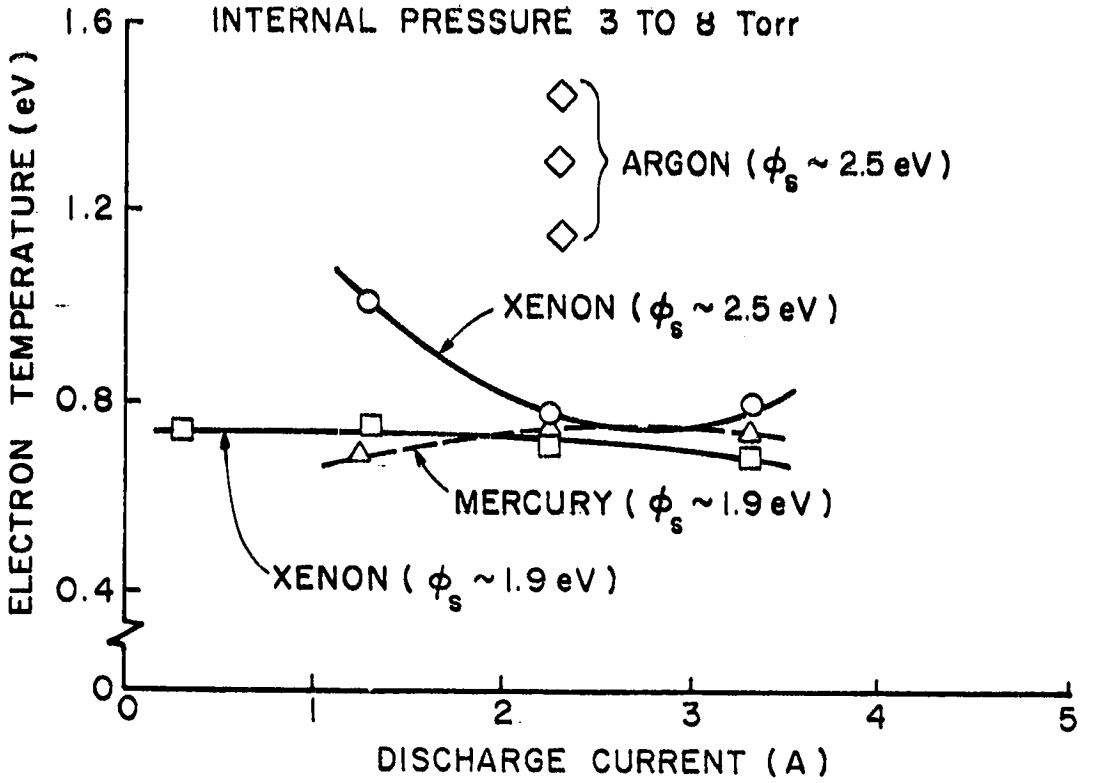

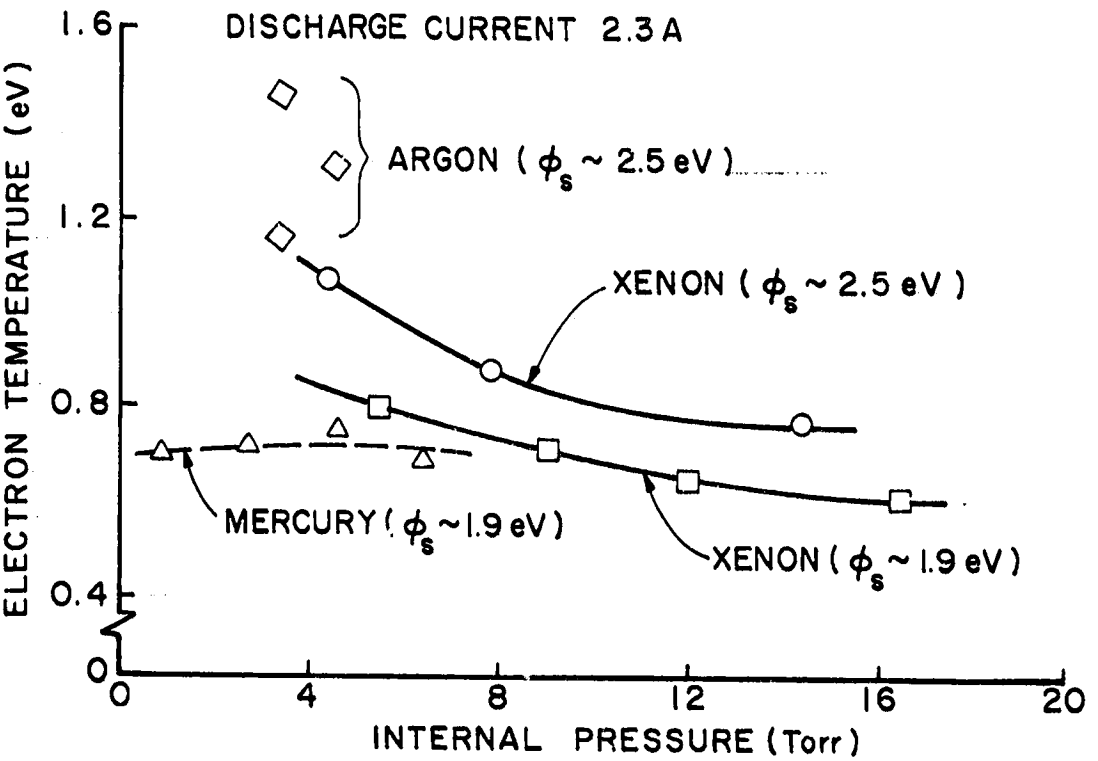

Fig. 32. Effect of Propellant and Insert Surface Work Function on Electron Temperature

exhibits higher plasma densities than does mercury under similar conditions and has a lower atomic mass, both of which result in greater ion fluxes to the surface than those seen with mercury. These higher ion fluxes to the surface could also be a factor in enhancing the depletion rate for the low work function oxide on the insert.

Another difference seen when operating with argon and xenon was a greater tendency for the electron emission region to locate itself at some upstream point on the insert. Although, as with mercury, the most stable emission site is apparently at or near the downstream end of the insert, a relatively large number of instances of emission from other sites was observed in the case of argon and xenon. In addition, when electron emission was established at an upstream location with argon and xenon, the alternate site was relatively more stable and less likely to shift back to its normal downstream location than it was in similar situations observed with mercury. Emission from regions other than the downstream end of the insert may be a reflection of the greater insert depletion rate discussed above, because such behavior was usually observed during operation under higher surface work function conditions.

Another related phenomenon observed with argon and xenon was the tendency to form localized emission spots one to two millimeters in diameter. Although these were also observed occasionally during operation with mercury, their occurrence was more common with argon and xenon. This was in part due to the fact that a considerable amount of the operating time particularly in the initial xenon experiments was at a relatively high internal pressure, and the occurrence of these localized spots exhibited a definite correlation with operation at high internal pressure. In fact, initiating such localized emission could be readily accomplished by operation at pressures

above ~ 10 Torr. The results of the experiments suggest that operation at such high pressures should probably be avoided because the intense local activity accelerates depletion of low work function materials from the insert.

The results presented in Figs. 29 to 32 and discussed above suggest that the basic physical processes for cathodes operating on argon and xenon are probably very similar to the ones found in mercury cathodes. That is surface emission normally takes place from a relatively well defined region near the downstream end of the insert, predominantly as a result of field-enhanced thermionic emission. The emission from this region coincides with and, indeed, sustains the intense excitation and ionization in the volume adjacent to the surface emission region. The length of the emission/ion production region is different for the three propellant types as are the magnitudes of the plasma properties but, at least at first glance, the basic physical processes would appear to be similar.

Collisional Processes in the Ion Production Region

In the next section more detailed results will be presented which show the effect of discharge current and mass flow rate on the operation of the hollow cathode with xenon and argon. Those results will provide an opportunity for comparison with the predictions of the analytical model. However, in order to make calculations with the model, it is first necessary to know the total inelastic cross-sections describing electron/atom and electron/ion collisions at energies near the primary electron energy. This energy is numerically the same as the plasma potential. These cross-sections are needed to determine the primary electron energy exchange mean free path and also to provide general information about important collisional processes taking place within the cathode. This section will present the necessary cross-sections for argon and xenon and discuss them in terms of the relevant collisional processes.

C-2

The total inelastic cross-section for electron impact is shown as a function of electron energy in Fig. 33 for argon and xenon. For energies below the first ionization level (15.7 eV for argon; 12.1 eV for xenon,) the data come exclusively from Ref. 29. They are presented in the form of a composite excitation cross-section containing all of the excitation levels lumped together. For energies above the first ionization energy, the ionization cross-sections (Ref. 30) are added to the excitation cross-sections (Ref. 29) to obtain the results shown in Fig. 33.

Argon and xenon cathodes both behave very much like cathodes operating on mercury. However, in the case of xenon there appear to be significant differences in the details of the important collisional processes. For example, Fig. 34 shows the inelastic mean free path for a primary electron colliding with xenon atoms as a function of xenon atom density and with primary electron energy as a parameter. The same plot for mercury is shown for comparison in Fig. 35. For typical operating conditions (neutral density = 3×10^{16} cm^{-3} and plasma potential ~ 9 v) xenon is seen to have an inelastic mean free path about 25 times the ~ 1 mm value shown for mercury. In addition, Fig. 34 shows that for xenon the mean free path exhibits a very strong energy dependence particularly for electron energies in the range observed in a typical cathode (8.5 - 10 eV). For xenon, the mean free path is very sensitive to energy over this range because the energies are near the excitation threshold energy, while for mercury electron energies in the 8.5 to 10 eV range are considerably above the first excitation level (4.8 eV).

In the model developed for mercury cathodes, the energy exchange mean free path for a primary electron is used as a criterion for the length of the emission region. This quantity depends not only on the inelastic mean free path (λ_{IN} shown in Figs. 34 and 35), but also on the energy exchange

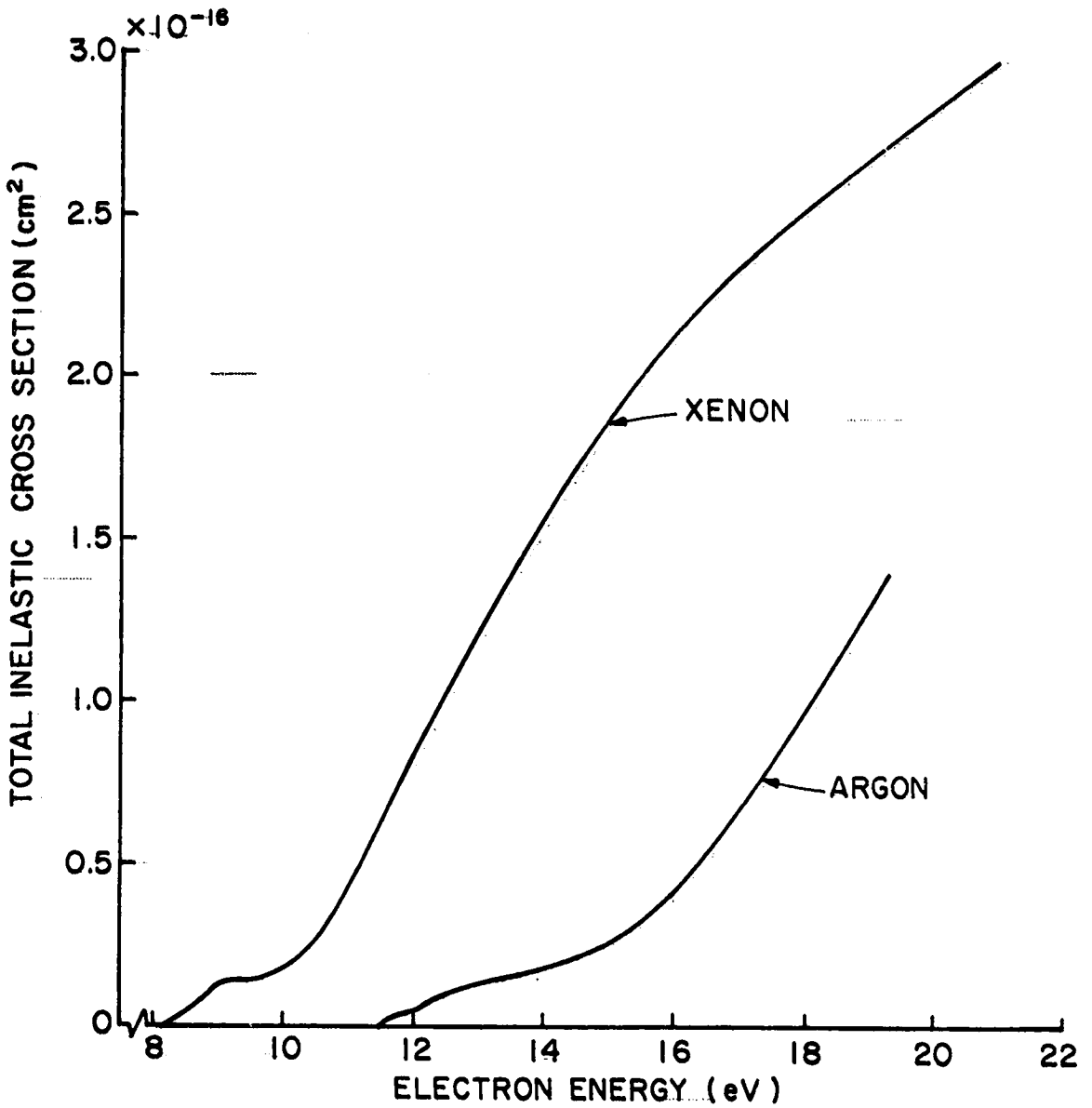

Fig. 33. Argon and Xenon Inelastic Cross Sections

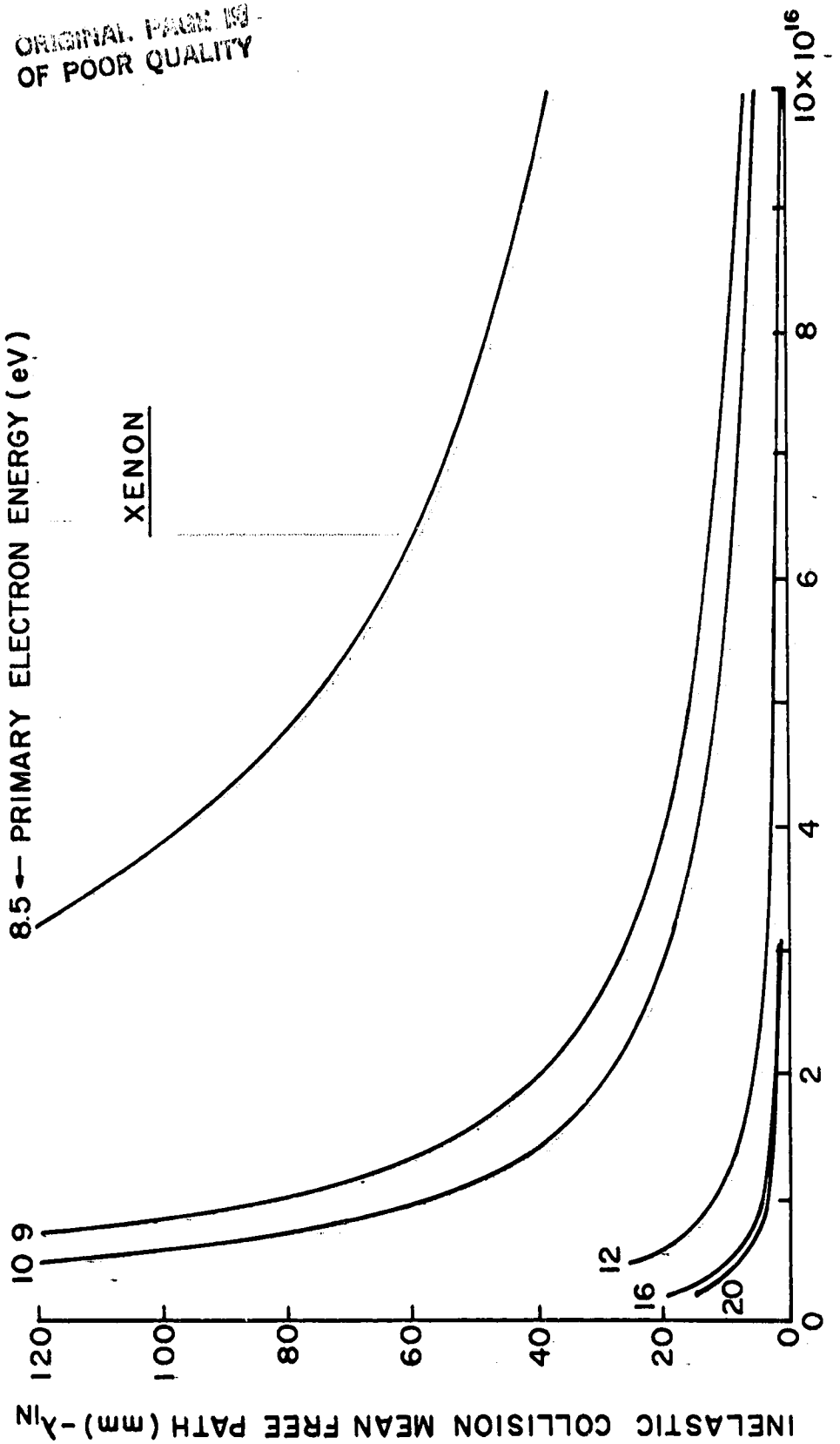

Fig. 34. Electron Inelastic Mean Free Paths in Xenon

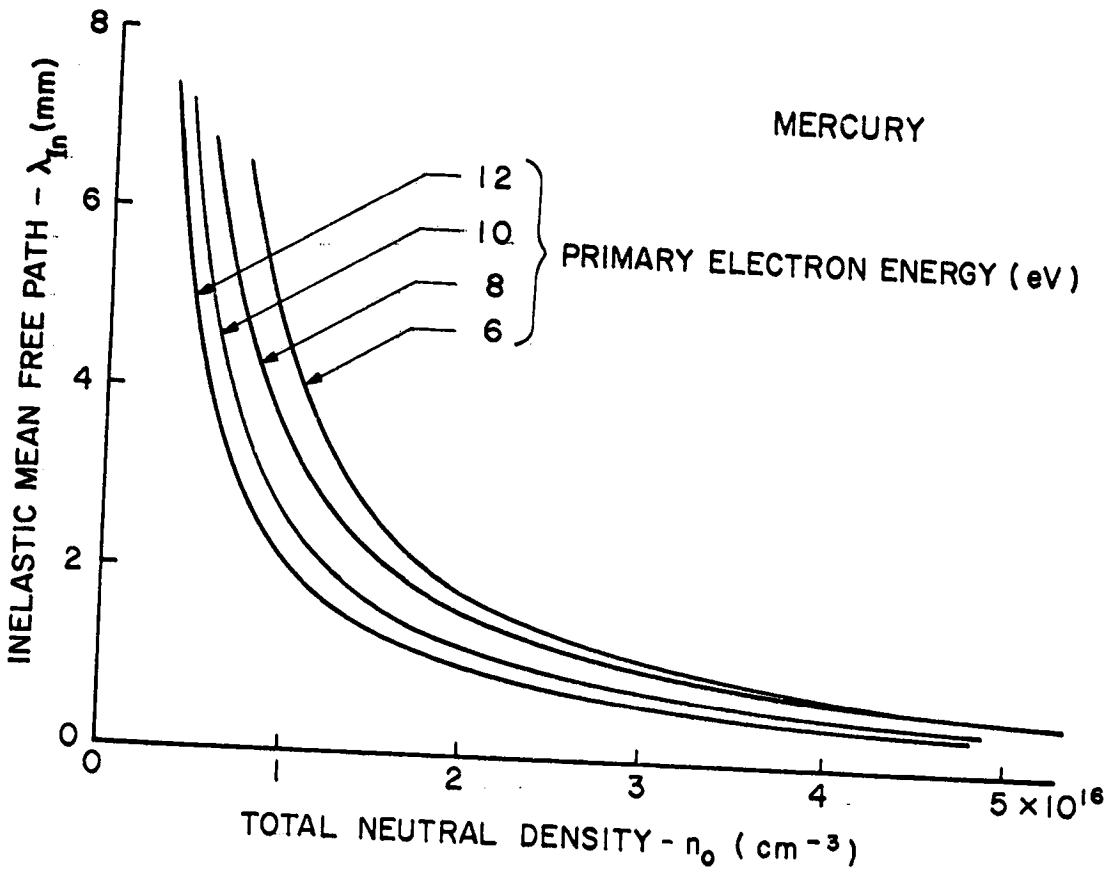

Fig. 35. Electron Inelastic Mean Free Paths in Mercury

mean free path associated with elastic scattering collisions between primary electrons and the low energy Maxwellian electrons (λ_e); specifically

$$\lambda_{pr} = (1/\lambda_{In} + 1/\lambda_e)^{-1} \quad . \tag{47}$$

The electron scattering mean free path (λ_e) is given by

$$\lambda_e(mm) = \frac{\varepsilon_{pr}^2\ (eV)}{6.5 \times 10^{-20} n_e(m^{-3})} \tag{48}$$

This quantity is plotted in Fig. 36 as a function of plasma density with primary electron energy as a parameter.

There are some significant features of Fig. 36 that are noteworthy. Typical internal plasma conditions for both mercury and xenon cathodes are described by a plasma density of $\sim 2 \times 10^{14}$ cm^{-3} and a plasma potential (and hence primary electron energy) of ~ 9 v. Figure 36 shows these conditions result in an electron elastic scattering mean free path on the order of 6 mm. Because the energy exchange mean free path for primary electrons (λ_{pr}) goes as the sum of the inverses of λ_{In} and λ_e (Eq. 47), its numerical value is dominated by the shorter of these two mean free paths. For mercury λ_{In} is typically ~ 1 mm and this term dominates so λ_{pr} is ~ 1 mm. On the other hand for xenon, λ_{In} is typically much larger than λ_e, so that λ_{pr} is generally close in length to λ_e. Physically, this means that in the case of the mercury plasma the primary electrons give up most of their energy in excitation and ionization reactions, while for xenon they tend to be thermalized by elastic scattering with Maxwellian electrons. This suggests that for the xenon plasma much of the excitation and ionization is induced indirectly from the high energy tail of the Maxwellian electrons. Such a situation is also consistent with the fact that the xenon discharge is

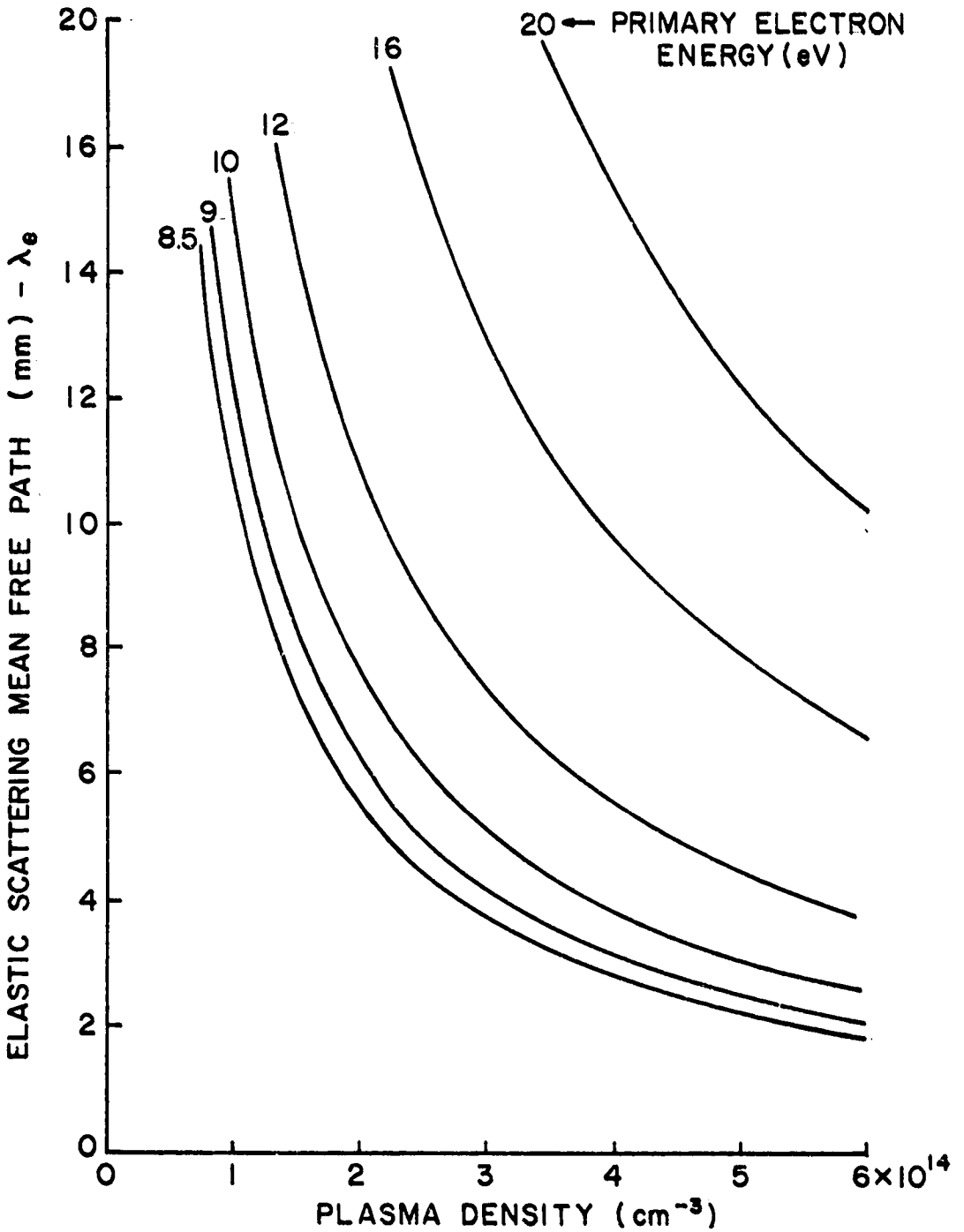

Fig. 36. Electron Elastic Mean Free Path in Electrons

observed to operate at plasma potentials close to the first excitation level.

It is also interesting to note that the effects of primary electron energy on the inelastic and elastic scattering mean free paths (λ_{In} and λ_e) shown for xenon in Figs. 34 and 36 are opposite. Hence, while elastic mean free path dominates at low primary electron energies, the situation reverses at energies above $\sim$ 12 eV. Above this primary electron energy the inelastic reactions begin to dominate and the situation resembles that found in the mercury discharge where most of the primaries give up their energy in excitation and ionization reactions. In fact, such a shift probably does occur if the insert surface work function increases significantly, since the work function increase is accompanied by an increase in plasma potential (see Fig. 31).

Comparison of Results with Model Predictions

Data were collected for the hollow cathode operating on xenon and on argon over a range of discharge currents and flow rates. The results of these experiments will be presented here and compared with predicted results based on calculations made using the analytical model.

The key points of the analytical model were described briefly in an earlier section of this report and are discussed in detail in Ref. 28. A summary of the equations used in the model are reproduced from Ref. 28 in Appendix B. If controllable operating parameters (discharge current and mass flow rate) and the cathode physical configuration (dimensions, surface work function and thermal characteristics are specified, the equations of the model, as summarized in Appendix B, can predict cathode operating conditions such as insert temperature and plasma potential. Calculations using the model were performed for both xenon and argon based on the following considerations.

1) Experimentally determined pressures were used as input to the model rather than mass flow rate. In design applications where measured pressures are not available, the empirical relationship given in Eq. B1 of the model can be used to estimate the pressure from the flow rate and orifice diameter. The experimental results used in determining the parameters of the empirical pressure-flow rate relation (Γ . B1) for argon and xenon are presented in the next section.

2) The surface work function ϕ_s for the insert was not known. The value used in the calculations was chosen to give agreement between the calculated temperature and the average measured temperature at one arbitrarily chosen experimental condition. The comparison between the calculated and measured average temperatures will, therefore, be a relative one valid mainly for checking the functional dependence on discharge current and pressure predicted by the model.

3) The thermal power loss from the insert ($\dot{Q}_{th}$ in Eq. B6) used for the calculations was based on the thermal analysis described in Appendix C of Ref. 30 for what is essentially the same insert-cathode tube configuration used in the present experiments. The following equation represents an approximation to that analysis.

$$\dot{Q}_{th} = (526\ T_s - 3.99 \times 10^5)\ L_e\ d_{in} . \qquad (49)$$

In this equation, T_s is the average emission surface temperature in °K and the emission length L_e and insert diameter d_{in} are both in meters. Equation 49 was used in calculating the results presented here.

4) The electron temperature was assumed to be 0.8 eV for the xenon calculations and 1.3 eV for argon.

5) The ratio of emission length to mean free path L_e/λ_{pr} was chosen to be one half in applying the model to argon and xenon. A ratio of unity

would indicate that the active region of the cathode was indeed one primary energy exchange mean free path long. Such a criterion for the active region was, however, never expected to be precise and the ratio of one half used in the calculations was simply chosen to give reasonable agreement with the experimentally observed emission lengths. For mercury, a ratio of two was found to give good results. The fact, that a value of 0.5 gives good results for both argon and xenon may be related to the fact that the excitation cross-section data for both gases were drawn from the same source (Ref. 29). Other cross-section data for xenon,[31] showed the excitation cross-section increasing almost twice as fast near threshold as that used here from Ref. 29. If the data of Ref. 31 were used, it would significantly alter the ratio of L_e/λ_{pr}, pushing it closer to unity.

6) Because Eq. B10 cannot be solved explicitly for the surface temperature T_s the equations in the model were solved in an iterative manner. Such a solution requires a determination of the total inelastic cross-section at each iteration. Since the calculations were made on a computer, this was handled by entering the cross-section data from Fig. 33 as arrays of data pairs and using an interpolation routine to determine intermediate values.

The results of calculations using the model based on the assumptions discussed above are shown in Figs. 37 through 40 for argon and Figs. 41 through 44 for xenon. The predictions of the model are plotted as the solid curves, while experimental data points corresponding to the predicted parameter are indicated by the circles. All of the experimental data were obtained using a cathode operating with a 0.76 mm diameter orifice. In each pair of plots, the upper plot shows the indicated parameter as a function of discharge current at a constant flow rate (287 mA for argon; 92 mA for xenon); while the lower plot shows the parameter plotted as a function of

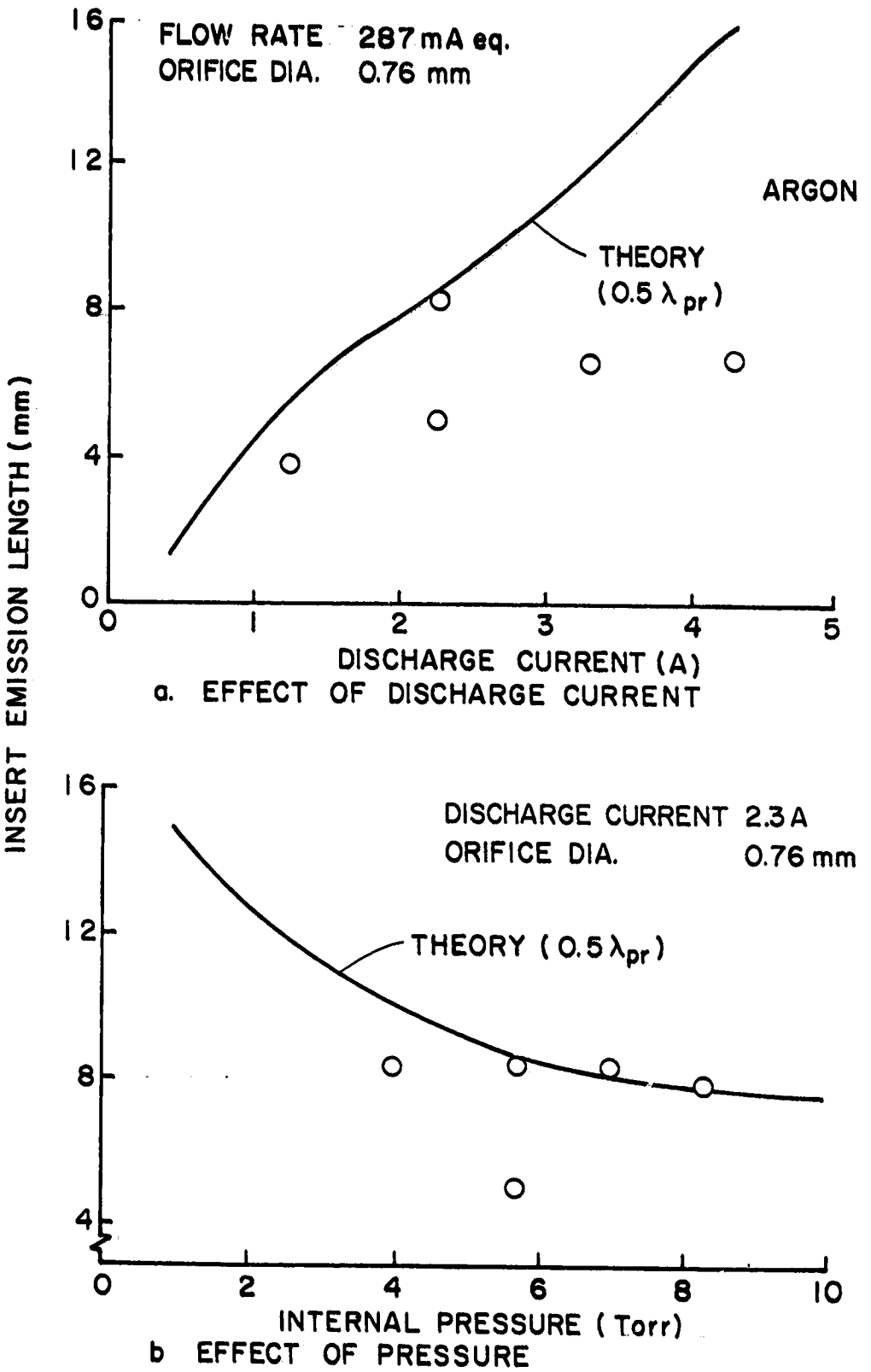

Fig. 37. Insert Emission Length Behavior for Argon

ARGON

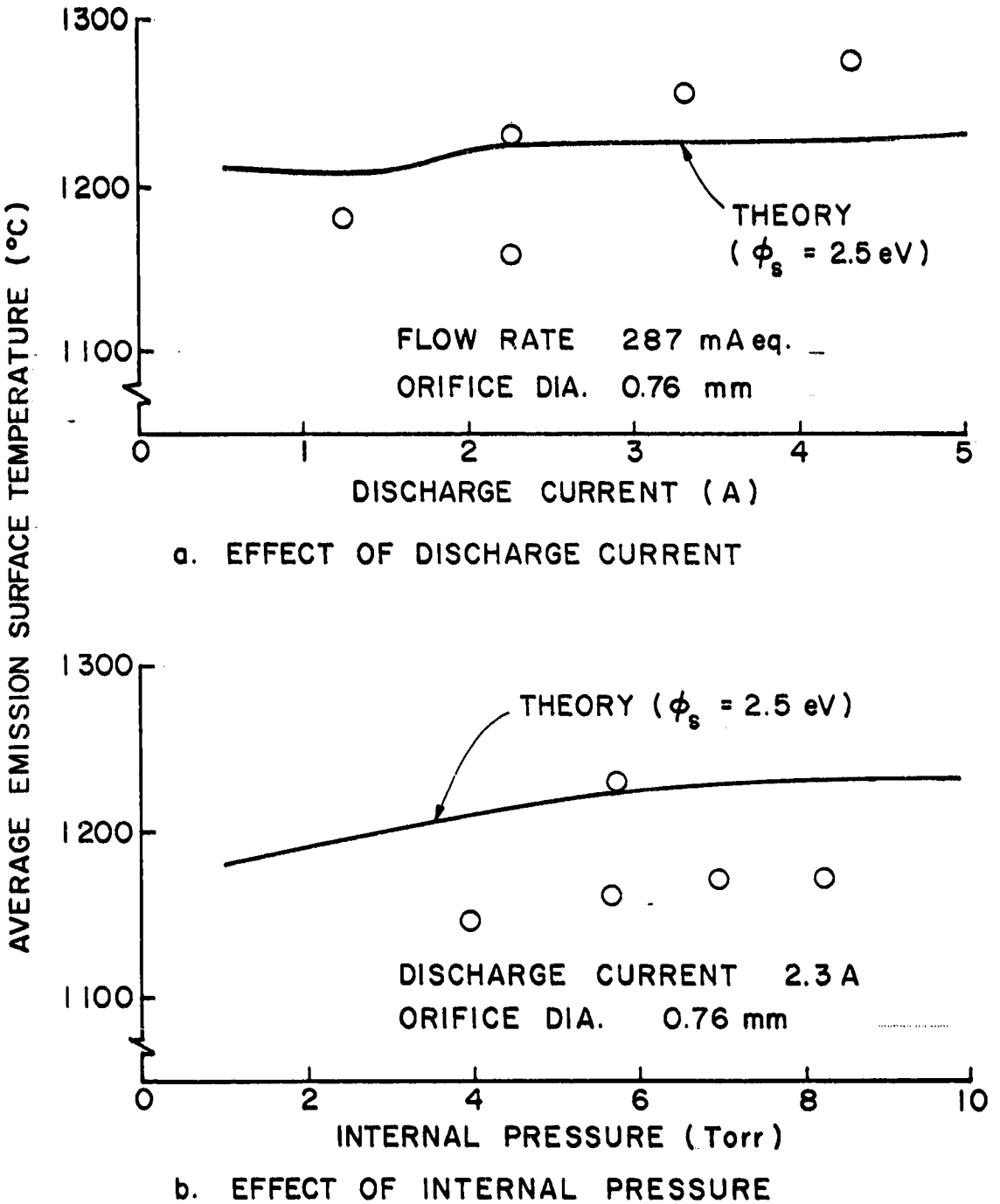

Fig. 38. Emission Surface Temperature Behavior for Argon

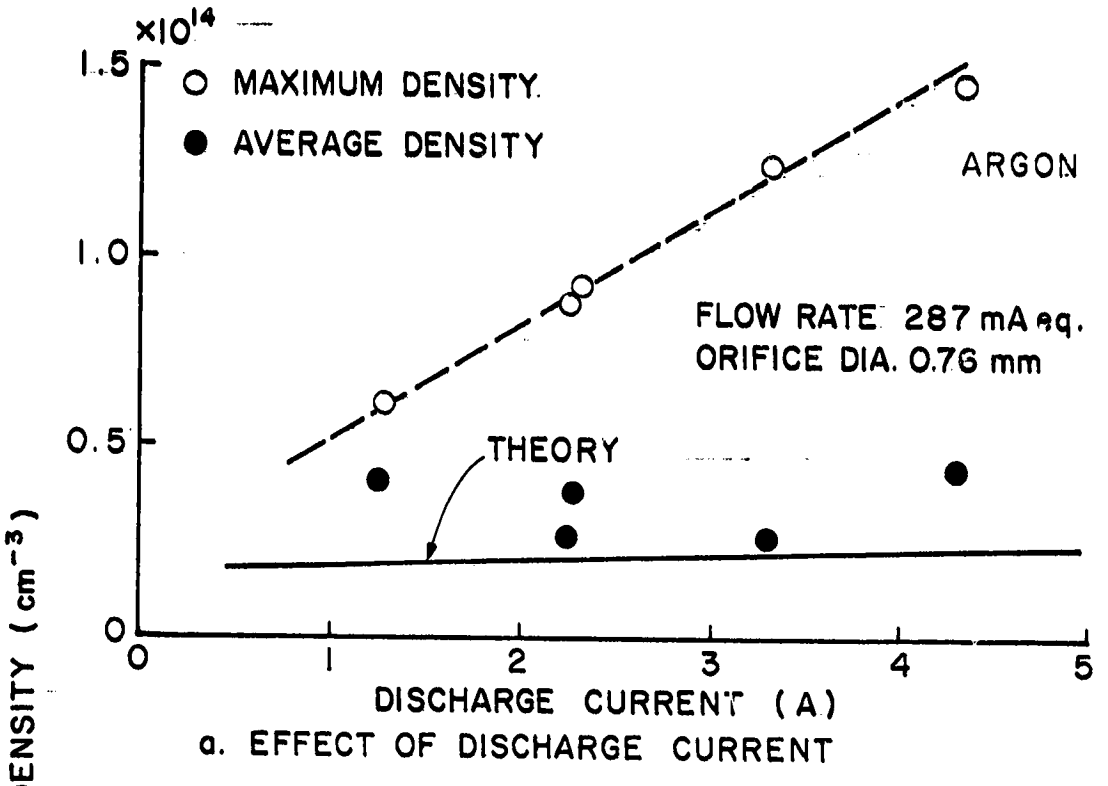

a. EFFECT OF DISCHARGE CURRENT

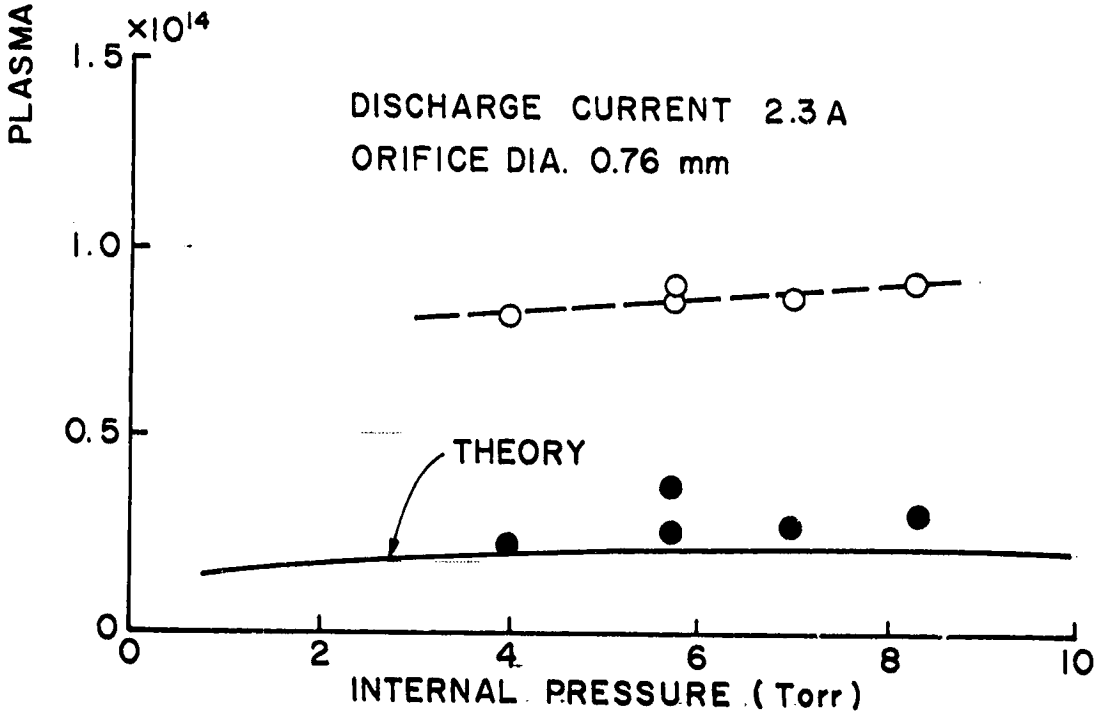

b. EFFECT OF INTERNAL PRESSURE

Fig. 39. Plasma Density Behavior for Argon

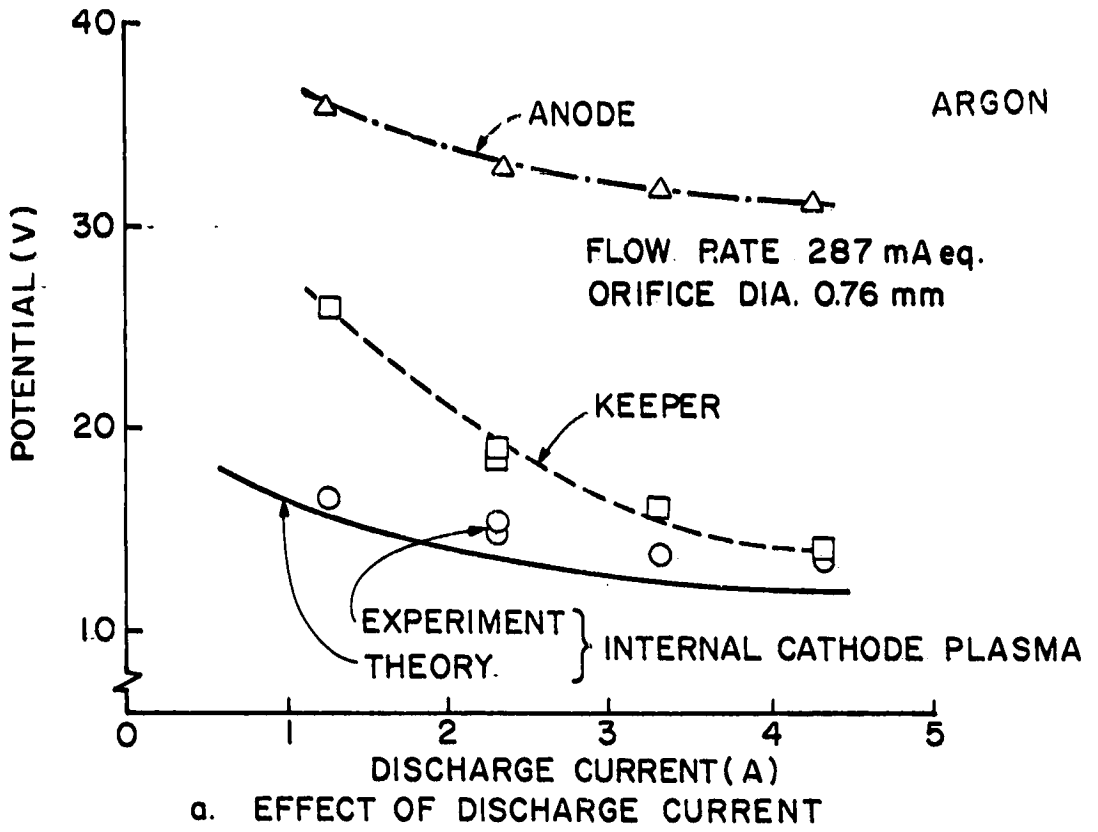

a. EFFECT OF DISCHARGE CURRENT

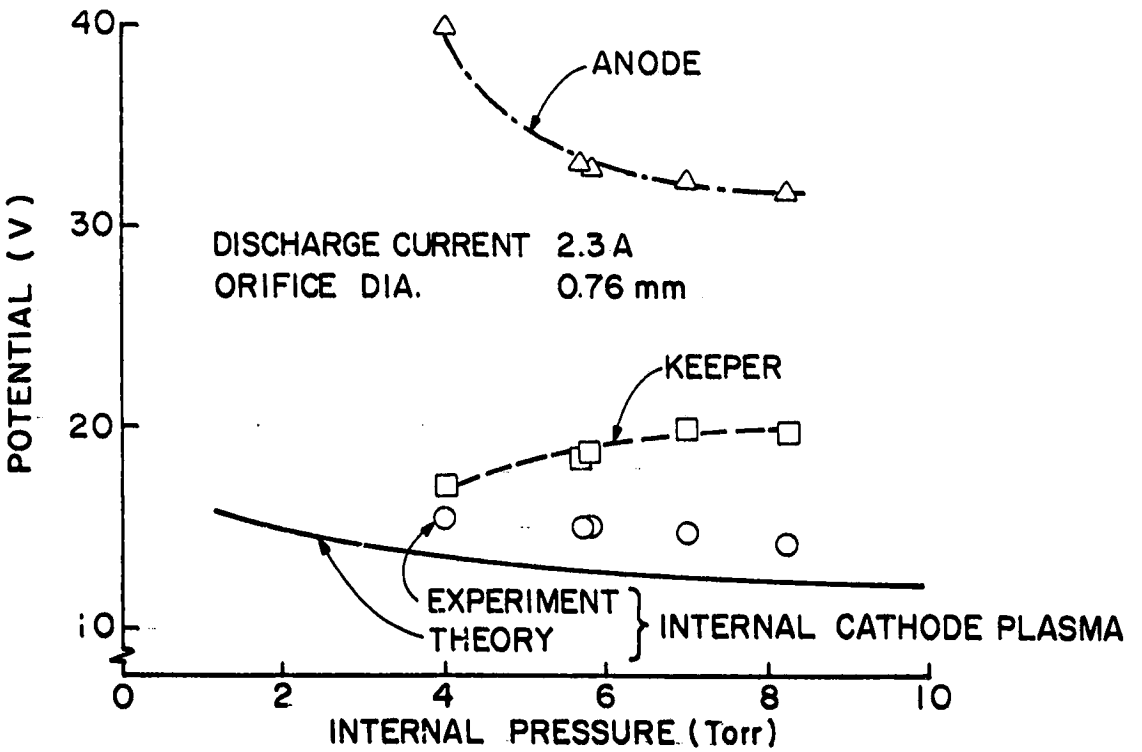

b. EFFECT OF INTERNAL PRESSURE

Fig. 40. Behavior of Potentials for Argon

XENON

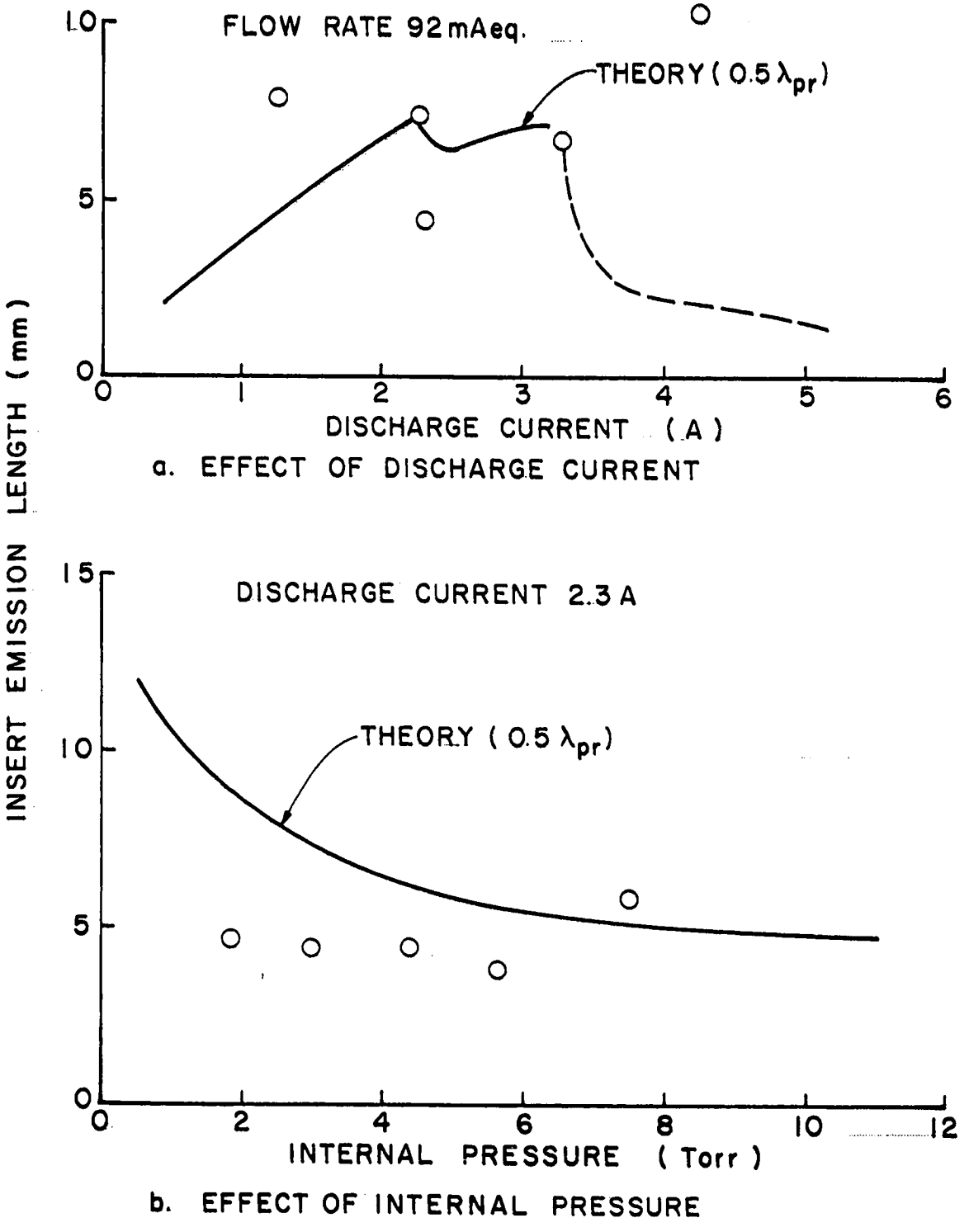

Fig. 41. Insert Emission Length Behavior for Xenon

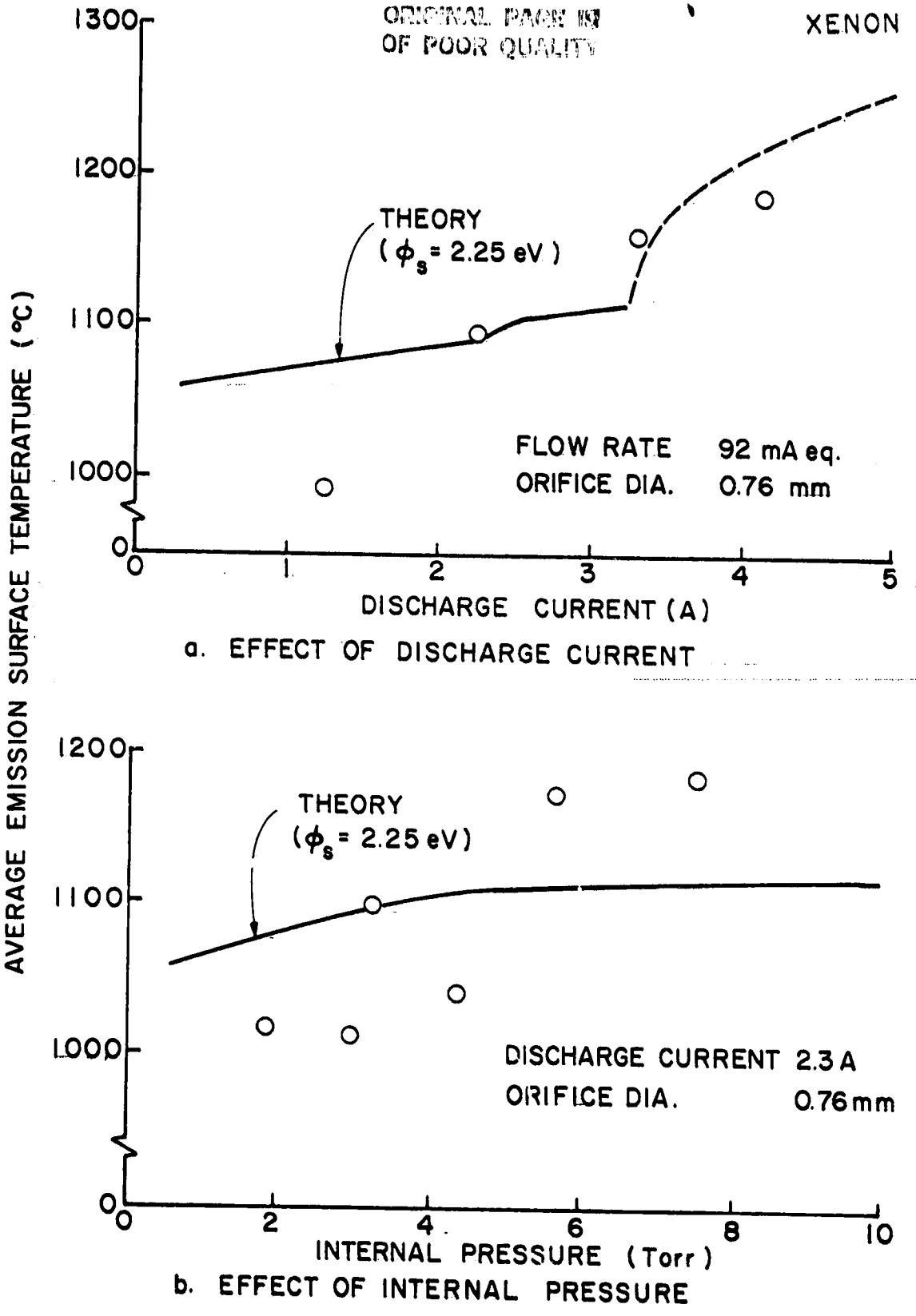

Fig. 42. Emission Surface Temperature Behavior for Xenon

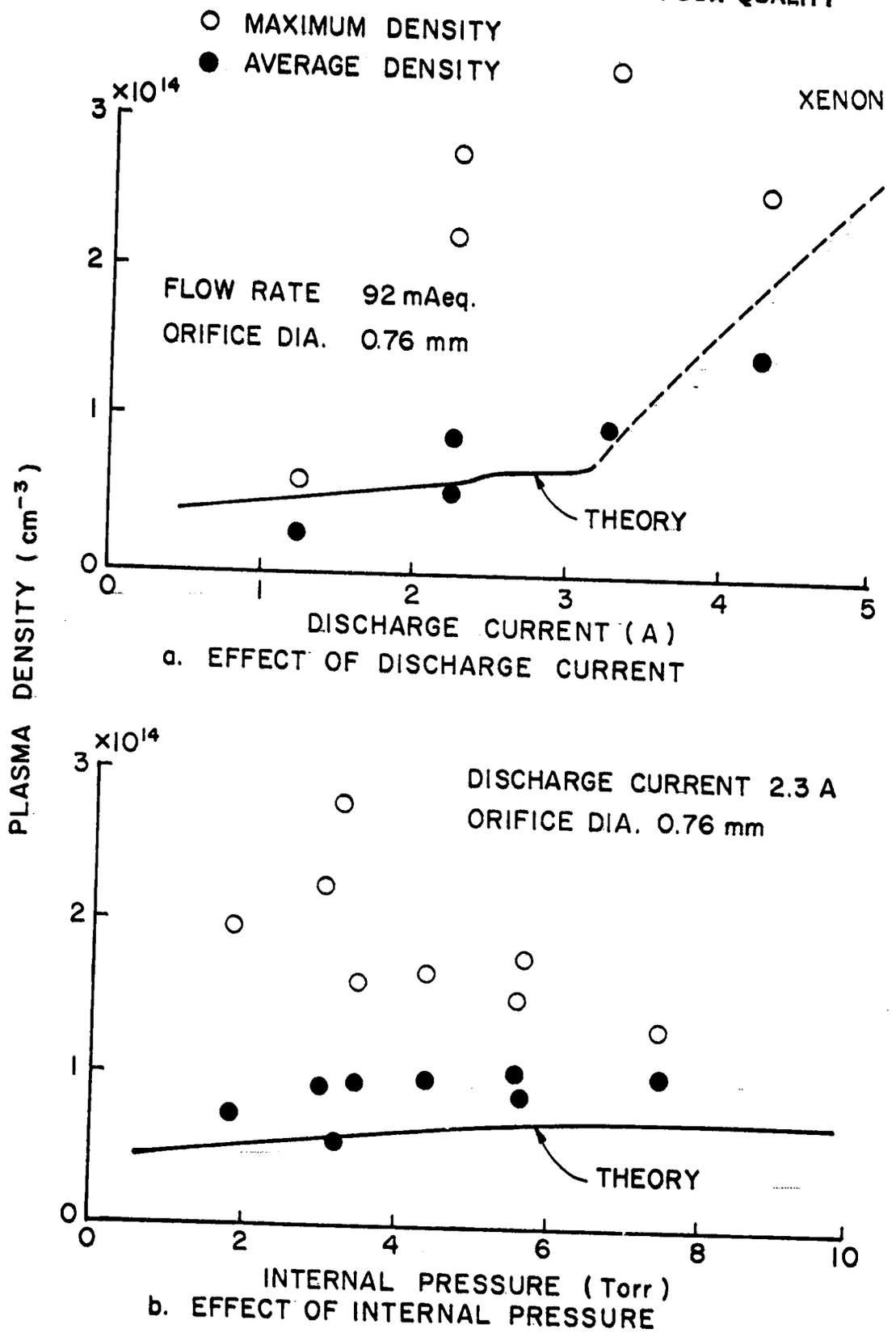

Fig. 43. Plasma Density Behavior for Xenon

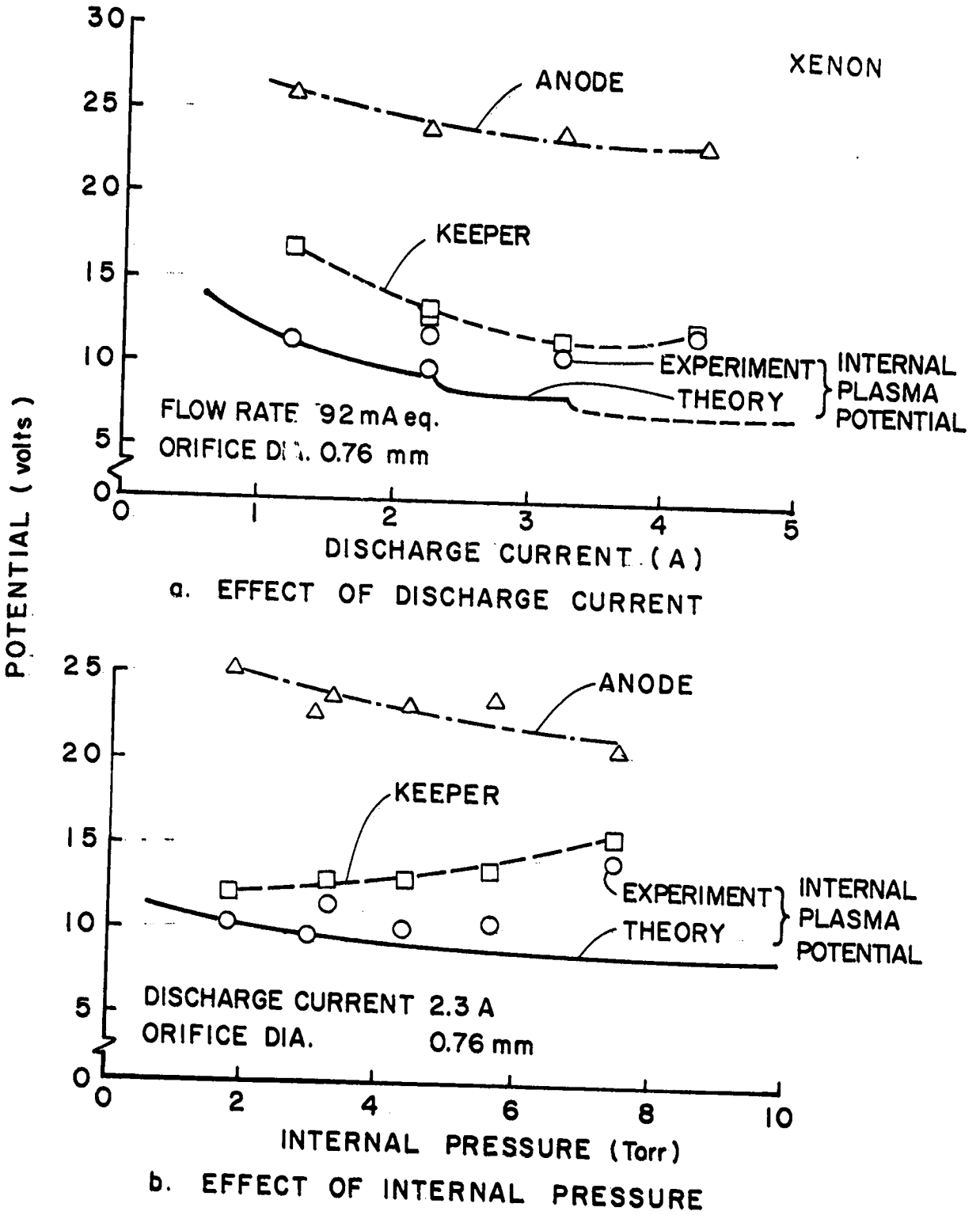

Fig. 44. Behavior of Potentials for Xenon

internal pressure at a constant discharge current of 2.3 A. The calculations for argon were based on an insert surface work function of 2.5 eV; while those for xenon were for a work function of 2.25 eV.

The effects of discharge current and internal pressure on emission surface length are shown in Fig. 37 for operation on argon. The experimental emission lengths were determined from the measured insert temperature profiles using the criterion that the emission extended upstream to a point where the temperature (in °K) had dropped to 90% of the maximum temperature. It is estimated that a length based on this criterion accounts for ~ 90% of the total insert emission current. Figure 37 shows that the experimentally determined emission length increases moderately with increasing discharge current at a constant flow rate (upper plot) and is relatively independent of internal pressure (lower plot) over the range of pressures covered in the experiments. The calculated emission lengths based on a criterion of one half of the primary energy exchange mean free path are shown in Fig. 37 by the solid curve. The solid curves show discharge current and pressure trends similar to the experimental data.

At this point, it is worth pointing out a general feature of the experimental results shown in Fig. 37 which is also present in most of the other figures. In both the upper and lower plots of Fig. 37 all of the data fall along a single trend line except for one data point. The data along the trend line were all taken in sequence. For example, in the upper plot the discharge current was varied while holding the flow rate constant to obtain the data which follow the trend line. The odd point in that plot comes from the corresponding experiment used in obtaining the trend line data in the lower plot. That is the experiment in which the discharge current was held constant while the pressure was varied. The difference

between the odd data point and the trend line is an indication of the change in operating conditions which took place between the different phases of the experiment and is believed to be due mostly to the changes in the insert surface condition which were discussed earlier.

Figure 38 shows the effect of discharge current and internal pressure on the average emission surface temperature for the cathode operating on argon. The average temperatures represented by the circles are an integrated average (over the emission length) determined from the measured insert temperature profiles. Both the experimentally determined and the calculated surface temperature are seen in Fig. 38 to increase with increases in discharge current and with increases in internal pressure. As mentioned earlier, the calculated results were based on a surface work function of 2.5 eV chosen to give agreement at one arbitrary experimental condition (apparent in Fig. 38). The comparison between the calculated and experimental results is, therefore, on the basis of curve shape and slope. Based on this criterion the agreement between the calculated and experimental temperature results is reasonably good, particularly for the temperature as a function of internal pressure (lower plot).

The increase in emission temperature with increasing pressure (lower plot, Fig. 38) seen with argon is just opposite to the mercury results which showed a decrease in temperature with increased pressure.[28] In both cases (argon and mercury), the model predicts an increase in temperature of the magnitude and shape shown in Fig. 38. This predicted behavior is linked to the decrease in emission area with increasing pressure (lower plot, Fig. 37). It is unclear why, in the case of mercury, the measured temperature did not also follow such a trend.

The effects of discharge current and internal pressure on the plasma density in the ion production region are shown in Fig. 39 for the cathode

operating on argon. Again the solid curve indicates the behavior predicted by the model. The experimental results indicated by the circles were obtained from two different measurements. The open symbols and dashed line were based on the spherical probe measurement and are the maximum value of the plasma density along the cathode axis. The solid circles are results calculated from the measured current to the upstream surface of the orifice plate assuming that the current was due solely to the Bohm flux of ions to that surface. As such, the solid symbols represent what is really an average plasma density across the downstream boundary of the ion production region. Since the model assumes uniform properties within the ion production region, the plasma density calculated with the model is really an average density and is more appropriately compared with the average measured values indicated by the solid symbols than with the maximum values (open symbols). Such a comparison shows the predictions of the model to be quite good both in magnitude and functional dependence on the independent variable.

It is interesting to note here that the plasma density, both measured and predicted, are relatively constant as the pressure is increased at a constant discharge current (lower plot, Fig. 39). This is somewhat surprising since one would expect that to first order the plasma density would increase as the neutral density increases. The fact that this does not occur suggests competing effects such as reductions in excitation and ionization cross-sections due to decreased electron energy. This is, in fact, observed since both electron temperature (Fig. 32) and primary energy (see plasma potentials, lower plot, Figs. 40 and 44) were observed to decrease with internal pressure.

In Fig. 40, the effects of discharge current and internal pressure on anode, keeper, and internal plasma potential are shown for argon operation.

The keeper and anode potential are highly dependent on electrode geometry and spacing and downstream conditions such as background pressure. They are shown in Fig. 40 for two reasons. First, to give a general indication of where the potential drop occurs in the cathode; and second, to allow a comparison of similar results obtained with xenon using the same anode and keeper configuration. The parameter predicted by the model is the internal plasma potential and is indicated in Fig. 40 by the solid curves. Comparison between those curves and the circular symbols suggests that the plasma potentials predicted by the model are reasonably close both in their magnitude and in their functional dependence on the indicated parameters.

The model consistently predicts a plasma potential somewhat lower than the measured potential. This was also the case with mercury[28] and will be seen to be the case with xenon (Fig. 44) as well. The cause for the consistently low predicted values is believed to be related to a term neglected in the energy balance on which the plasma potential calculation is based. That term is the energy flux from the ion production region associated with the resonant and metastable atoms which leave the region. With the present model there is no reasonable way of accounting for that term and, as the results indicate neglecting the term still results in good qualitative agreement between the model and the experiment.

Results of the kind discussed above are shown in Figs. 41 to 44 for a similar cathode operating on xenon. It should be noted that the insert used in the tests in which these results were obtained had a work function somewhat lower (2.25 eV) than that used in the argon tests (2.5 eV). However, with one exception the results shown in Figs. 41 to 44 are qualitatively very similar to those presented in Figs. 37 to 40 for argon and will not be discussed in detail except to make a few brief points of comparison.

The main difference to be pointed out is the numerous inflection points and discontinuity in the slope of the calculated results for the constant flow rate case (upper plot, Figs. 41 to 44). The inflections in the curves for the calculated results correspond to the inflections in the inelastic cross-section curve for xenon (Fig. 33) at low primary electron energies. The dashed portion of the curve following the discontinuity in slope (upper plot, Figs. 41 to 44) indicates the conditions where the model predicts primary electron energies below the 8.3 eV excitation threshold of xenon. This is apparent if one examines the predicted plasma potential curve in the upper plot of Fig. 44. At discharge currents above $\sim$ 3.3 A, the model predicts an internal plasma potential less than 8.3 eV. The discontinuity in the slope of the plasma potential curve at a discharge current of 3.3 A is, therefore, just a reflection of the discontinuity in the slope of the cross-section curve at the threshold energy of 8.3 eV. Physically, the solutions at discharge currents above 3.3 A represent the situation where most of the excitation and ionization must be due to the energetic tail of the Maxwellian electron distribution since the primaries have insufficient energy to excite or ionize ground state atoms. (Excitation and ionization of excited neutrals would still be possible.) This is the extreme case of the situation discussed earlier where it was noted that for xenon at lower primary energies the elastic scattering term for the primaries dominates over the inelastic one in determining the primary energy exchange mean free path. In such a situation most of the primary energy would be deposited in the Maxwellian electron population, and it is that population which must sustain the discharge.

It is worth making a couple of additional comparisons between the xenon and argon results. Both the predicted and the measured values of

emission length for xenon (Fig. 41) were substantially shorter than for argon (Fig. 37). The average plasma density is greater for xenon than for argon (lower plot, Figs. 39 and 43). Finally, the anode potentials with xenon (Fig. 44) are 8 - 10 volts less than with argon (Fig. 40).

Pressure-Flow Rate Correlations

In the experiments just described, the internal pressure was determined by direct measurement using the manometer shown in Fig. 28. However, normally the internal cathode pressure is unknown and mass flow rate is the parameter controlled during cathode operation. For most applications of the model, it is, therefore, desirable to have some means of relating internal cathode pressure to mass flow rate. Predicting this pressure from cathode dimensions, mass flow rate, and operating conditions is, however, a complex problem made particularly difficult by the following effects. For normal cathode dimensions and flow rates, the cathode operates in the transition regime between free molecular and continuum flow. In addition, because the gas is ionized, the flow is subject to energy input from plasma processes and is affected by the forces due to the electric fields set up within the plasma. Because of the complexity of the problem, the model developed for cathodes operating on mercury used an empirical formula for predicting cathode internal pressure.[28] The same approach will be taken here for argon and xenon.

In order to determine an empirical relation between the pressure and the flow rate, an experiment was run in which the stagnation pressure in the plenum chamber immediately upstream of the cathode was measured with the manometer for a wide range of emission currents (0-4.3A), orifice diameters (0.25 to 1.0 mm), and mass flow rates (50 to 1300 mA). The throttle valve shown in Fig. 28 was, of course, closed during these tests. The results

are shown in Figs. 45 and 46 respectively for argon and xenon where the parameter $P_o/(\dot{m}/d_o^2)$ is plotted as a function of total discharge current. Here P_o is the total stagnation pressure in Torr, $\dot{m}$ is the mass flow rate in milliamps equivalent, and d_o is the orifice diameter in millimeters. The circles in Figs. 45 and 46 represent the average value for all of the data collected at that discharge current. A straight line can be used to fit the average values reasonably well. The equations shown in Figs. 45 and 46 represent the least squares fit of the data points to a straight line.

The bar on the symbols in Figs. 45 and 46 represents the range of the data for the various orifice sizes and flow rates. The full range is shown by the bars rather than the standard deviation because the spread in the data is not believed to be due so much to random experimental error but to the fact that the form of the correlation factor $P_o/(\dot{m}/d^2)$ does not completely account for the influence of the flow rate and the orifice diameter. It is believed that if the correlation factor fully accounted for the parameters of the problem, the range indicated by the bars would be much smaller. This form of the correlation factor was chosen, however, because it was used earlier in the mercury work[28] and it has a theoretical basis. Both the theory of free molecular flow and the theory of continuum, choked flow predict that the pressure-mass flow relation takes the form

$$P_o/(\dot{m}/d_o^2) = C\sqrt{T/M} \tag{50}$$

where T is the stagnation temperature at the orifice and M is the atomic mass of the gas. The parameter C is a constant of proportionality which is different for the two cases (free molecular and continuum). The gas temperature for the zero discharge current case was maintained during the tests

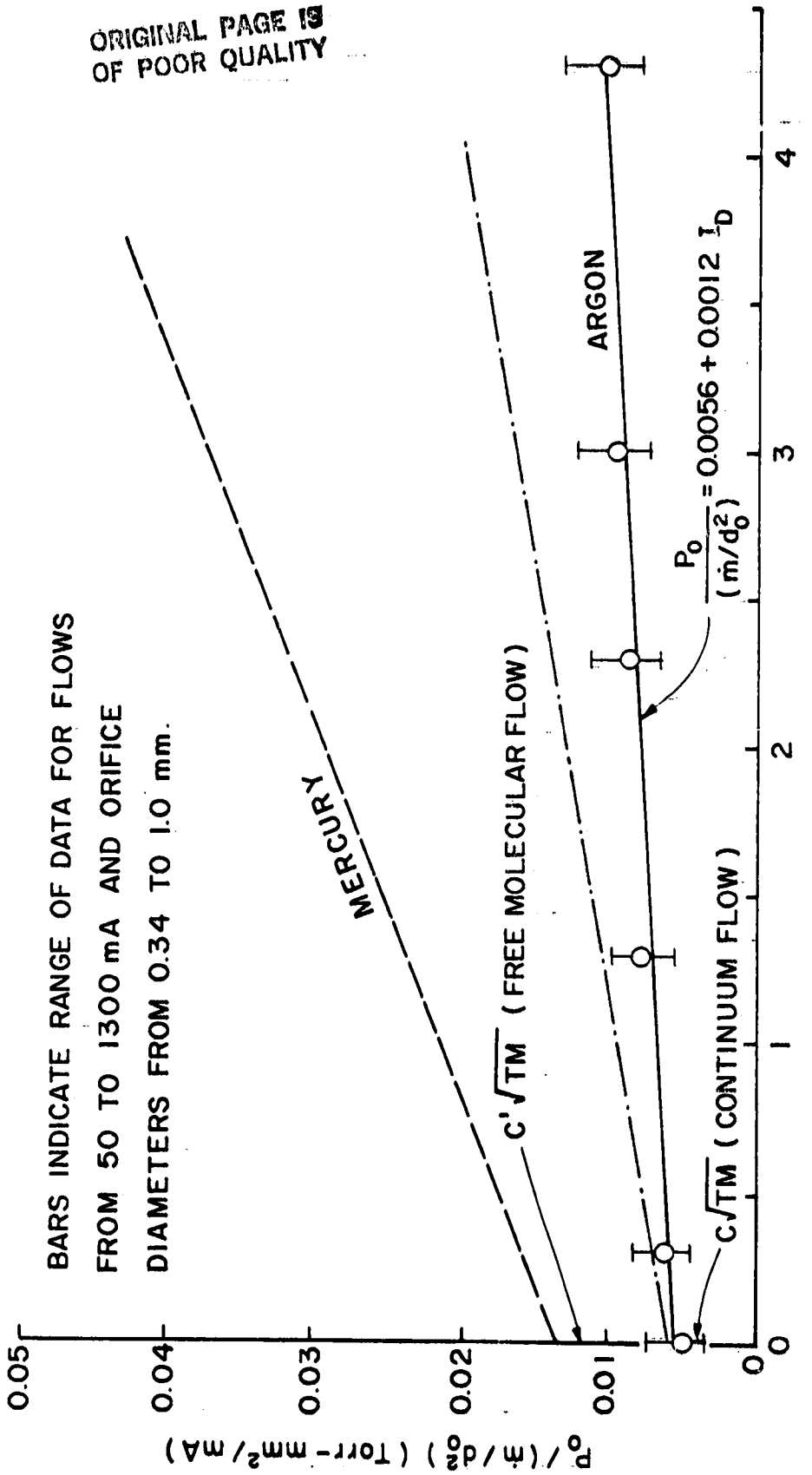

Fig. 45. Internal Pressure/Flow Rate Correlation for Argon

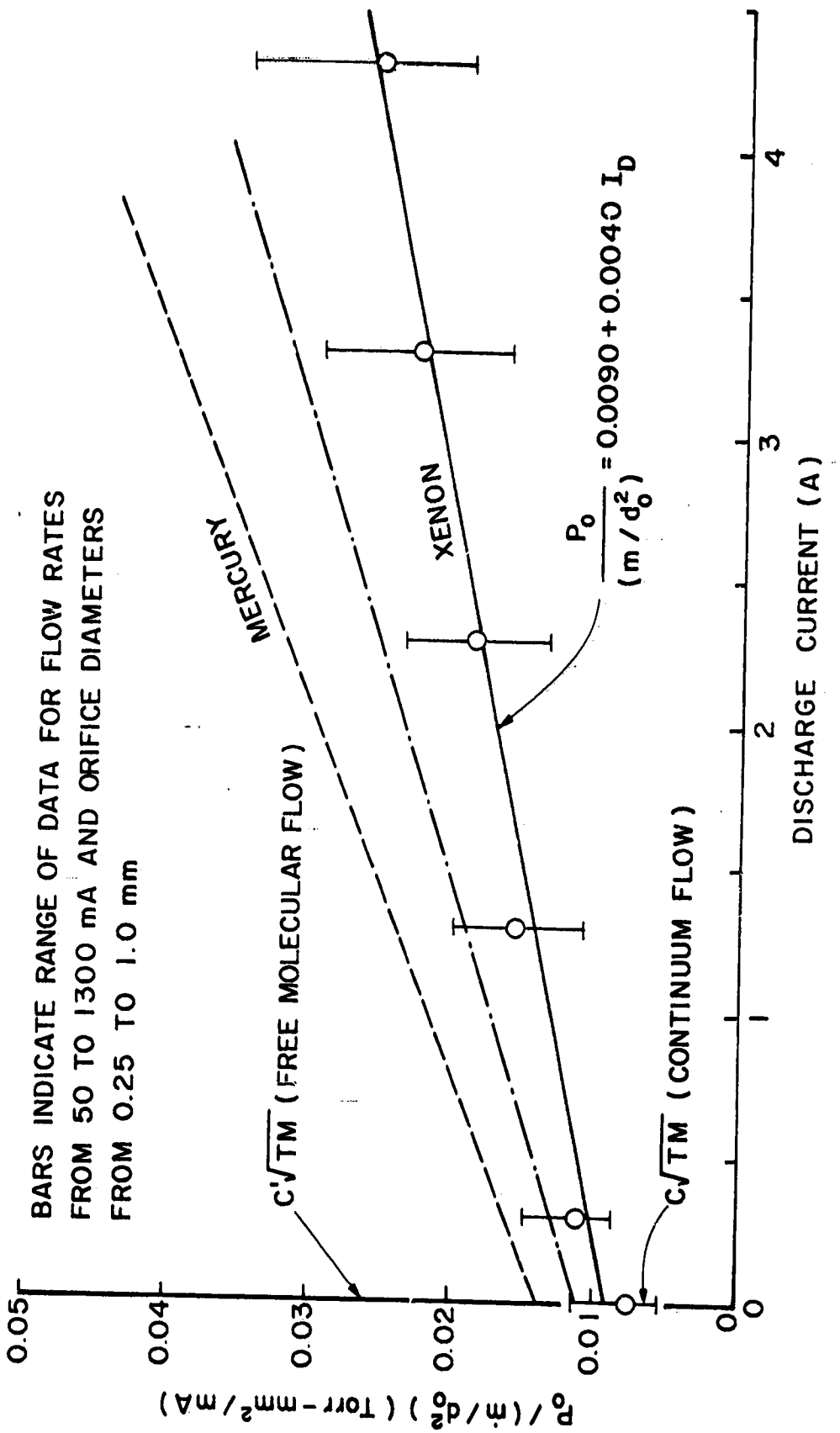

Fig. 46. Internal Pressure/Flow Rate Correlation for Xenon

at ~ 1000°C using the cathode heater. (This is probably also close to the neutral particle temperature when the discharge is on). The values of $C'\sqrt{TM}$ based on this temperature are plotted on the vertical axis for the free molecular and continuum flow cases. For the no discharge case, the hollow cathode flow for both argon and for xenon falls in the transition region between the two types of flow, though it is much closer to being continuum flow than free molecular flow. The parameter $C'\sqrt{TM}$ is used here to distinguish it from the term on the right hand side of Eq. 50. The parameter $C'\sqrt{TM}$ accounts for the fact that the units of $\dot{m}$ used for the correlation factor in Figs. 45 and 46 are milliamps equivalent. That is $\dot{m}$ as used in the figures really represents a charged particle flow rate rather than a mass flow rate, hence, the dependence $\sqrt{TM}$ rather than $\sqrt{T/M}$.

For comparison, the pressure flow correlation determined for mercury[28] is shown in Figs. 45 and 46 by a dashed line. The center dashed line shown in Fig. 45 was obtained by multiplying the mercury result by $\sqrt{M(\text{argon})/M(\text{mercury})}$. Predicting argon behavior from the mercury result in this manner is seen to yield good agreement in the no discharge case. However, when the discharge is present such an extrapolation of the mercury data predicts a pressure higher than the measured argon pressure. Similar results are shown in Fig. 46 for xenon. While it was initially anticipated that the pressure flow results should scale with atomic mass in the manner suggested by $C'\sqrt{TM}$, this is obviously not the case when a discharge is present.

It is suggested that the equations indicated in Figs. 45 and 46 be used to calculate the internal pressure when applying the model to cathodes using argon or xenon and the pressure is not known. This is indicated by Eq. B1 which appears in the summary of the model presented in Appendix B.

Conclusions

The results of the tests discussed above suggest that the physical processes important in the operation of argon and xenon hollow cathodes are similar to those for the mercury cathode. Namely, that field-enhanced thermionic emission is the predominant surface emission mechanism with a significant fraction of the total current coming from the Bohm flux of ions to the cathode surfaces. Surface emission occurs mainly from a region near the downstream end of the insert and extends over an axial distance on the order of the primary electron energy exchange mean free path. The one notable difference between the processes found in the argon and xenon cathodes and those in the mercury cathode is that much of the excitation and ionization is carried out by the high energy tail of the Maxwellian electrons for the inert gases. This effect is most significant at low insert surface work function conditions where the plasma potential is sufficiently low so that the primary energy drops below the excitation threshold energy. In this situation, the inelastic contribution to the primary electron energy exchange mean free path becomes very small and most of the primary electrons are thermalized before having an inelastic collision. However, this difference in the collisional processes in the cathode does not invalidate the analytical model. In fact, when applied to hollow cathodes operating on argon and xenon, the model was found to predict operating parameters which agreed well with the experimental results both in magnitude and in their functional dependence on operating conditions. This agreement was predicated on the assumption that the ratio of emission length to primary electron energy exchange mean free path was one half. This is a reasonable value given the general assumptions and approximations made in the model. The fact, that predictions of the model agree well with experimental results for three

propellants which have significantly different excitation cross-sections and atomic masses is a strong indication that the assumptions of the model are valid and represent a good description of the basic physical processes underlying the operation of the orificed hollow cathode.

For a given insert surface work function the emission surface temperatures are similar for cathodes operating on all three propellants--argon, xenon, and mercury. However, for operation with argon and xenon low surface work functions were difficult to obtain and they tended to increase significantly during the period of several hours required to conduct the experiments. It is believed that the degradation of the insert is due to prevailing plasma conditions which enhance sputter damage of the surface when operating with argon and xenon. As the surface work function increases the surface temperature and plasma potential both increase causing increasingly rapid deterioration of the surface. It is believed that this degradation process is probably significantly worse with the single layer tantalum foil insert used in these experiments than it would be with the impregnated inserts used in actual thruster cathodes. It is quite possible that the surface work function of impregnated inserts would appear to be relatively stable while increased sputtering of the surface would increase the depletion rate of the impregnant and, thereby, reduce the lifetime of the cathode. This is an area that should probably be investigated more closely if cathodes with impregnated inserts are to be operated with argon and xenon.

The present experiments suggest that rolled foil inserts coated with a double carbonate mixture may not exhibit adequate lifetimes when operated with argon and xenon. An investigation into alternative insert materials and/or coatings or the use of a multilayer foil insert without any coating would also be indicated as potentially fruitful areas for improving

performance and reliability of cathodes operating with argon and xenon. Aston[32] and Kaufman[33] have both had some success with uncoated tantalum foil inserts. Such a cathode, however, would require careful design to minimize thermal losses from the insert and special provisions to insure reliable starting. In addition, discharge voltages in such a cathode are expected to be significantly higher than in a cathode with a coated or impregnated insert.

REFERENCES

1. Rovang, D. C., "Ion Extraction Capabilities of Two-Grid Accelerator System," NASA CR-174621, February 1984.

2. Wilbur, P. J., C. E. Mitchell and B. D. Shaw, "The Electrothermal Ramjet," J. of Spacecraft and Rockets, v. 20, No. 6, Nov.-Dec. 1983 pp. 603-610.

3. Longhurst, G. R. and Wilbur, P. J., "Plasma Property and Performance Prediction for Mercury Ion Thruster," AIAA Paper No. 79-2054, Oct. 30-Nov. 1, 1979.

4. Arakaw, Y., and Kawasaki, Y., "Discharge Plasma in a Multiple Ion Thruster," AIAA Paper No. 82-1931, Nov. 17-19, 1982.

5. Masek, T. D., "Plasma Properties and Performance of Mercury Ion Thrusters," AIAA Paper No. 69-256, March 3-5, 1969.

6. Knauer, W., "Power Efficiency Limits of Kaufman Thruster Discharges," AIAA Paper No. 70-177, Jan. 19-21, 1970.

7. Lee, J. F., Sears, F. W., and Turcotte, D. L., "Satistical Thermodynamics," p. 77, Addison-Wesley, 1973.

8. Dugan, J. V. and Sovie, R. J., "Volume Ion Production Costs in Tenuous Plasmas: A General Atom Theory and Detailed Results for Helium, Argon, and Cesium," NASA TN D-40150, 1967.

9. Hershkowitz, N., et. al., "Plasma Leakage Through a Low β Line Cusp," Physical Review Letters, Vol. 35, No. 5, pp. 277-280, 1975.

10. Leung, K. N., et. al., "Plasma Confinement by Localized Cusps," The Physics of Fluids, Vol. 19, No. 7, pp. 1045-1053, 1976.

11. Hershkowitz, N., et. al., "Electrostatic Self-Plugging of a Picket Fence Cusped Magnetic Field," The Physics of Fluids, Vol. 21, No. 1, pp. 122-125, 1979.

12. Kozima, H., et. al., "On the Leak Width of Line and Point Cusp Magnetic Fields," Physics Letters, Vol. 86A, No. 6, 7, pp. 373-375, 1981.

13. Clausing, P., "Über die Stromung sehz Verdünnter Gase Durch Rören von Beliebiger Länge," Annalen der Physik, Vol. 12, pp. 961-989, 1932.

14. deHeer, F. J., et. al., "Total Cross Sections for Electron Scattering by Ne, Ar, Kr and Xe," J. Phys. B: Atom. Molec. Phys., Vol. 12, No. 6, pp. 979-1002, 1979.

15. Sovey, J. S., "Improved Ion Containment Using a Ring-Cusp Ion Thruster," AIAA Paper No. 82-1928, Nov. 1982.

16. Poeschel, R. L., "Development of Advanced Inert-Gas Ion Thrusters," NASA CR-168206, June 1983.

17. Brophy, J. R. and Wilbur, P. J., "The Flexible Magnetic Field Thruster," J. Spacecraft and Rockets, Vol. 20, No. 6, pp. 611-618, Nov.-Dec. 1983.

18. Brophy, J. R. and Wilbur, P. J., "Recent Developments in Ion Sources for Space Propulsion," Proc. Int'l Ion Engineering Congress, ISIAT '83 and IPAT '83, Kyoto, Japan, Sept. 1983, pp. 411-422.

19. Goebel, D. M., "Ion Source Discharge Performance and Stability," Phys. Fluids, 25(6), June 1982, pp. 1093-1102.

20. Kaufman, H. R., "Ion Thruster Propellant Utilization," Ph.D Thesis, Dept. Mech. Engineering, Colorado State University, Fort Collins, Colorado, 1971.

21. Kerslake, W. R., "Charge-Exchange Effects on the Accelerator Impingement of an Electron-Bombardment Ion Rocket," NASA TN-D 1657, May 1963.

22. Bohm, D., "Minimum Ionic Kinetic Energy for a Stable Sheath," appears in The Characteristics of Electrical Discharges in Magnetic Fields, eds. A. Guthrie and R. K. Wakerling, McGraw Hill, 1949.

23. Robinson, R. S., "Physical Processes in Directed Ion Beam Sputtering," NASA CR-159567, March 1979.

24. J. A. Dillon, Jr., W. F. Sheradin, H. D. Edwards, and S. N. Ghosh, "Charge Transfer Reactions in Monatomic and Diatomic Gases," J. Chem. Phys., 23, 776-779 (1955).

25. J. B. Hasted, "The Exchange of Charge Between Ions and Atoms," Proc. Roy. Soc. (London) A205 421 (1951).

26. Longhurst, G. R., "Prediction of Plasma Properties in Mercury Ion Thursters," NASA CR-159448, Dec. 1978.

27. Aston, G., Kaufman, H. R., and Wilbur, P. J., "Ion Beam Divergence Characteristics of Two-Grid Accelerator Systems," AIAA Journal, Vol. 16, May 1978, pp. 516-524.

28. Siegfried, D. E., "A Phenomenological Model for Orificed Hollow Cathodes," NASA CR-168026, Dec. 1982.

29. Specht, L. T., et. al., "Electron Ionization and Excitation Coefficients for Argon, Krypton and Xenon in the Low E/N Region," JAP. vol. 51, pp. 166-170, Jan. 1980.

30. Rapp, D. and P. Englander-Golden, "Total Cross-Sections for Ionization and Attachment in gases by Electron Impact, I. Positive Ionization," J. Chem. Phys., Vol. 43, pp. 1464-1479, 1965.

31. Dixon, A. J. and von Engel, A., "Total Inelastic Cross Sections for Slow Electrons in Xenon," Int. J. Electronics, Vol. 25, No. 3, 1968, pp. 233-237.

32. Aston, G., "Summary Abstract: A Hollow Cathode for Ion Beam Processing Plasma Sources," JVST A, Vol. 1, No. 2, Ap-June 1983, p. 258.

33. Kaufman, H. R. and R. S. Robinson, "Inert Gas Thrusters," NASA CR-165332, Dec. 1980.

Appendix A.

NOMENCLATURE FOR

DISCHARGE CHAMBER WORK

A_g - Grid area (m^2)

C_o - $4\sigma_o \ell_e/(ev_o A_g \phi_o)$ (Aeq.$^{-1}$)

e - Electronic charge (1.6×10^{-19} coul.)

f_B - Extracted ion fraction

f_C - Fraction of ion current produced that goes to cathode potential surfaces.

J_A - Ion current to anode potential surfaces (A)

J_B - Beam current (A)

J_C - Ion current to cathode potential surfaces (A)

J_D - Discharge current (A)

J_E - Cathode emission current (A)

J_j - Rate of production of j^{th} excited state expressed as a current (A)

J_L - Current of primary electrons lost to the anode (A)

J_M - Current of Maxwellian electrons to the anode

J_p - Ion production current (A)

k - Boltzmann's constant (1.38×10^{-23} J/°K)

ℓ_e - Primary electron containment length (m)

m_{Ar} - Argon atomic mass (kg)

m_{Kr} - Krypton atomic mass (kg)

$\dot{m}$ - Propellant mass flow rate (Aeq.)

n_e - Plasma density (m^{-3})

n_o - Neutral density (m^{-3})

$\dot{n}_o$ - Neutral loss rate (Aeq.)

P_o - Probability of a primary electron/neutral atom collision prior to electron collection at the anode

T_o - Neutral atom temperature (°k)

T_W - Wall temperature (°k)

U_j - Excitation energy of j^{th} excited state (eV)

U_+ - Ionization energy (eV)

V_C - Potential (relative to cath. pot.) from which electrons are accelerated to become primaries (V)

V_D - Discharge voltage (V)

v_e - Electron velocity (m/s)

v_o - Neutral atom velocity (m/s)

$\forall_p$ - Plasma volume (m^3)

ε_B - Average beam ion energy cost (eV)

ε_M - Average energy of Maxwellian electrons leaving the plasma at the anode (eV)

ε_p - Average plasma ion energy cost (eV)

ε_p^* - Average plasma ion energy cost neglecting primary electron energy lost to the anode (eV)

ε_o - Average plasma ion energy cost considering ionization and excitation processes only (eV)

η_u - Propellant utilization

σ_o - Total inelastic collision cross section for primary electron - neutral atom collisions (m^2)

σ_+ - Ionization collision cross section (m^2)

σ_j - Excitation collision cross section of j^{th} state (m^2)

ϕ_o - Effective grid transparency to neutrals

ϕ_a - Accelerator grid transparency

ϕ_s - Screen grid transparency

APPENDIX B

EQUATION SUMMARY FOR HOLLOW CATHODE MODEL

Dan Siegfried

The collection of equations which comprise the analytical model describing hollow cathode operation are shown in Table BI. Originally developed for a cathode operating on mercury, these equations appear to hold equally well for operation on argon and xenon, and are the ones used to calculate the results presented. The first column of Table BI. indicates the physical basis for the equation shown in column three and the second column notes important assumptions. Table BII. gives the empirically determined constants (C_1, and C_2) used in the pressure-flow rate correlation given by Eq. B1. and also indicates recommended values for the constant C_3 and the electron temperature (T_e). Table BIII. lists the symbols and units used for the parameters in the equations in Table BI. It should be noted that all of the equations in Table BI. are in MKS units EXCEPT for the parameters in the empirical expression for the pressure (Eq. B1).

Given the mass flow rate $\dot{m}$, the orifice diameter d_o, the total discharge current I_D, the surface work function ϕ_s, the insert thermal power loss $\dot{Q}_{th}$, and the physical constants (e, k, m_i, ε_o, ε_i, a_o), the equations in Table BI. can be solved for all of the other parameters except the electron temperature. Suggested values for the electron temperature are indicated in Table BII. Because Eq. B10 cannot be solved explicitly for the surface temperature T_s, the solution of these equations is necessarily iterative. Such a solution requires a determination of the total inelastic cross-section at each iteration. If the calculations are made on a computer, this can be handled by entering the cross-section data as an array of data pairs and using an interpolation routine to determine intermediate values.

Table B.I.

Summary of Equations Used in Model

Physical Basis	Comments	Equation	No.
Empirical	Neglects orific plate thickness effect. (See Table A.II. for C_1 and C_2)	$P = \frac{\dot{m}}{d_o^2}(C_1 + C_2 I_D) \times 10^{-3}$ (Torr) where $\dot{m}$(mA) and d_o(mm).	B.1
Ideal gas law	Assumes heavy particle temperature equal to insert temperature.	$n_o = \frac{P - n_e k(T_e + T_s)}{k T_s}$	B.2
Semi-empirical	Energy exchange mean free path based on results of computer model. Assumes $\varepsilon_{pr} = V_p$.	$\lambda_{pr} = \left[\frac{6.5\times10^{-17} n_e}{V_p^2} + \frac{10^3 n_o V_p}{2.83\times10^{23} - 1.5 n_o}\right]^{-1}$	B.3
Existence length for primary electron	Criterion for emission/ion production region length.	$L_e = C_3 \lambda_{pr}$	B.4
Current balance	Thermionic electron emission from insert only; ion flux based on Bohm criterion.	$I_D = I_e + I_i = j_{th} A_e + j_i A_s$	B.5
Insert energy balance	Neglects energy input due to excited states and plasma radiation.	$j_i = \left[\frac{\dot{Q}_{th}}{\phi_e} + I_D\right] \cdot \left[2A_c + A_e\left(1 + \frac{a}{\phi_e}\right)\right]^{-1}$ where $a \equiv (V_p + \varepsilon_i - \phi_s)$.	B.6

Table B.1. (cont.)

Summary of Equations Used in Model

Physical Basis	Comments	Equation	No.
Bohm criterion	Assumes uniform or average plasma properties	$n_e = \frac{j_i}{e[kT_e/m_i]^{\frac{1}{2}}}$	B.7
Energy balance on ion production region	Neglects energy loss due to excited states and plasma radiation.	$V_p = \frac{1}{I_D - j_i A_s}\left[\left(\frac{kT_e}{2e} + \varepsilon_i\right) j_i A_s + \frac{5kT_e I_D}{2e}\right]$	B.8
Double sheath analysis	Approx. based on theoretical analysis.	$E \approx \left[\frac{n_e\, kT_e}{\varepsilon_o}\right]^{\frac{1}{2}}\left[2\left(1+2\,\frac{eV_p}{kT_e}\right)^{\frac{1}{2}} - 4\right]^{\frac{1}{2}}$	B.9
Field-enhanced thermionic emission	Model neglects all surface emission mechanisms, except this one.	$j_{th} = a_o T_s^2 \exp\left(-\frac{e\phi_e}{kT_s}\right)$	B.10
Effective work function	Based on electric field at emission surface	$\phi_e = \phi_s - \left[\frac{e\lvert E\rvert}{4\pi\varepsilon_o}\right]^{\frac{1}{2}}$	B.11

Table B.II

Summary of Constants for Hollow Cathode Model

Gas	C_1	C_2	C_3	T_e
argon	5.6	1.2	0.5	1.3
mercury	13.7	7.8	2	0.7
xenon	9.0	4.0	0.5	0.8

Table B.III

NOMANCLATURE FOR CATHODE WORK

a_o - Theoretical constant (1.2×10^6 A/m^2 °K^2)

A_c - Area of end boundary of ion production region (m^2)

A_e - Insert emission area (m^2)

A_s - Total surface area of ion production region (m^2)

C_1 - Empirical constant for pressure-flow rate correlation (See Table B.II.)

C_2 - Empirical constant for pressure-flow rate correlation (See Table B.II.)

C_3 - Empirical constant relating emission length and mean free path (See Table B.II.)

d_o - Orifice diameter (mm)

e - Electronic charge (Coulombs)

E - Electric field at insert surface (V/m)

I_D - Total discharge current (A)

I_e - Insert electron emission current (A)

I_i - Total ion current to cathode surfaces (A)

j_i - Bohm current density (A/m^2)

j_{th} - Field-enhanced thermionic emission current density (A/m^2)

k - Boltzman's constant (1.38×10^{-23} J/°K)

L_e - Insert emission length (m)

$\dot{m}$ - Propellant mass flow rate (mA equivalent)

m_i - Ionic mass (kg/ion)

n_e - Electron density in ion production region (m^{-3})

n_o - Total neutral atom density in ion production region (m^{-3})

Table B.III (continued)

P - Internal cathode pressure

$\dot{Q}_{th}$ - Insert thermal power loss (W)

T_e - Electron temperature in ion production region (°K)

T_s - Insert surface temperature (°K)

V_p - Plasma potential in ion production region (V)

ε_i - Ionization potential

ε_o - Permittivitity of free space

ε_{pr} - Primary electron energy, equivalent to plasma potential V_p(eV)

λ_{pr} - Primary electron, energy exchange mean free path (m)

ϕ_e - Average effective work function (V)

ϕ_s - Average surface work function (V)